ABSTRACT

MOSSBAUER SPECTROSCOPY STUDY OF AGING AND FAST NEUTRON IRRADIATION EFFECTS IN A COPPER-RICH Cu-Fe ALLOY

by

Thomas Hugh Gould, Jr.

Chairman: Dietrich H. Vincent

Mössbauer spectroscopy was used to study the effects of both thermal and radiation environments on precipitation processes in the alloy Cu-0.6at%Fe. The first part of this study is concerned with interpreting the room temperature spectra produced by iron in a variety of configurations or 'phases' in alloy samples which were solution treated, aged at temperatures in the range 285-600°C, and cold-rolled. In the second part of the study, the knowledge gained from the thermal studies is applied to interpret the effects of fast neutrons on a variety of heat treated alloy samples.

A major portion of the thermal studies was devoted to low temperature (285°-400°C) aging, since small precipitates or clusters are the most sensitive to the effects of fast neutron irradiation. The Mössbauer spectra of samples aged at low temperatures are consistent with the growth of spherical clusters or Guinier-Preston zones. The distribution of isomer shifts and quadrupole splittings associated with local configurational variations of iron in three basic environments -- i.e., (1)iron with only Cu nearest neighbors represented by a slightly broadened singlet designated γ_0; (2) 'surface' iron with both Fe and Cu nearest neighbors represented by an ever changing

broad asymmetric doublet designated γ_2; and (3) 'volume' iron with only Fe nearest neighbors represented by a singlet designated γ_1 -- were treated by using Gaussian-distributed Lorentzian functions to fit the complex spectra. For this purpose, an efficient subroutine in which the Gaussian-Lorentzian convolution and its partial derivatives are expressed in terms of the complex error function was developed for use with a general least-square fitting program.

The spectra associated with both the early and very late stages of aging were found to be quite amenable to quantitative phase analysis. In addition, by assuming spherical cluster growth, approximate cluster sizes (or range of sizes) can be inferred from the Mössbauer spectra characteristic of initial and intermediate stages of aging. This was particularly valuable in evaluating the re-solution effects of fast neutron irradiation.

In the irradiation studies the Mössbauer technique provided an insight into the local environment of the precipitate or cluster phase that was not possible with the more conventional techniques of resistivity and magnetization which have been used in the past to study the effects of irradiation on precipitation-hardenable alloys. In the case of solution treated alloys, the Mössbauer spectra provided information concerning both the extent of irradiation-induced aging and the approximate size of the clusters formed. The results are consistent with the formation of very small clusters of less than 12 atoms in quenched-irradiated alloys.

The re-solution effects of displacement cascades or spikes on aged Cu-Fe samples was shown by Mössbauer spectroscopy to be extremely dependent upon the stage of aging or the cluster size. Aged samples

containing very small clusters (< 12 atoms) experience essentially complete dissolution of Fe clusters, whereas those with clusters of intermediate sizes experienced incomplete cluster break-up in the displacement spikes. In contrast, well-aged samples containing large γ-iron precipitates did not experience any dissolution effects, but instead experienced a slight growth in the precipitate phase. Mössbauer measurements were also useful in observing the effects of fast neutron irradiation on the equilibrium precipitate phase, α-iron.

THE UNIVERSITY OF MICHIGAN

COLLEGE OF ENGINEERING
Department of Nuclear Engineering

Technical Report

MÖSSBAUER SPECTROSCOPY STUDY OF AGING AND FAST NEUTRON IRRADIATION EFFECTS IN A COPPER-RICH Cu-Fe ALLOY

Thomas H. Gould, Jr.

Dietrich H. Vincent
Project Director

DRDA Project 035710

supported by:

NATIONAL SCIENCE FOUNDATION
GRANT NO. GK-17073
WASHINGTON, D.C.

administered through:

DIVISION OF RESEARCH DEVELOPMENT AND ADMINISTRATION ANN ARBOR

January 1974

TABLE OF CONTENTS

APPENDICES

LIST OF TABLES

LIST OF FIGURES

LIST OF APPENDICES

CHAPTER I

INTRODUCTION

A. Motivation and Purpose for This Study

R. L. Mössbauer's discovery of recoilless emission and absorption of nuclear gamma radiation in 1958[1] demonstrated that the theoretical limit of resolution, the γ-ray's natural line width, could be achieved under certain circumstances. This discovery opened up a new area of research, nuclear γ-ray resonance (Mössbauer) spectroscopy, which has found applications in nuclear physics, solid state physics, chemistry and biology. The Mössbauer spectrum from an emitting or absorbing nuclide is very sensitive to the nuclide's local electronic environment. From the hyperfine structure of such spectra it is possible to obtain information on internal magnetic fields, electric field gradients and s-electron densities at the nucleus as well as on lattice binding forces. As a consequence, the Mössbauer effect (ME) is being used, in addition to its many chemical and biological applications, as a solid state probe to investigate lattice defects including those introduced by radiation.

Early defect studies by ME spectroscopy were stimulated by an interest in understanding the local environment of Mössbauer nuclei whose low lying gamma states were produced by such techniques as alpha decay, coulomb excitation, and nuclear reactions. There was concern that such methods of producing the Mössbauer level would leave the

nucleus in a defect environment following recoil of the resonant atom. The logical extension of such studies was to intentionally introduce the Mössbauer nucleus into a defect environment for the purpose of gaining information about radiation induced defects. Several experiments of this type have been performed and are reviewed by G. K. Wertheim.[2]

Another radiation effects application, which has received almost no attention, is the use of ME spectroscopy to study solid state phase transformations induced by radiation bombardment. In this type of application it is necessary that the Mössbauer nuclide be uniquely associated with the phase(s) undergoing change. Also, for any such experiment to be successful it is necessary that the different environments of the Mössbauer nuclides induced by radiation be few in number and produce resolvable spectra. In general, for Mössbauer nuclides associated with several defect and normal lattice configurations, the resulting absorption spectrum would consist of a sum of the absorption lines characteristic of each configuration times the fraction of sites associated with that configuration.

This last statement points up the difficulties of obtaining useful information in radiation damage experiments from Mössbauer spectra. First, in order for there to be a significant effect, there must be an appreciable fraction of Mössbauer nuclides intimately associated with a given radiation induced defect configuration. Second, even for a limited number of such configurations it is quite likely that the resultant Mössbauer spectrum would not display well-defined (resolvable) structure. However, under conditions and in materials for which these problems are minimized, ME spectroscopy becomes a useful probe with

which to determine the local environments of absorbing (or emitting) nuclides in radiation 'damaged' materials. Such detailed information is not obtainable from some of the more conventional techniques used to study radiation effects in solids (e.g. resistivity, Hall coefficient, optical emission and absorption, saturation magnetization, etc.).

This work was undertaken for the purpose of determining the effectiveness of ME spectroscopy in probing the effects of fast neutron radiation on certain solid state transformations. The most promising applications seemed to be in the area of order-disorder transformations and precipitation hardening reactions. The latter type of transformation was chosen for several reasons. First, because of the added strength arising from precipitate particles in metallic alloys, age- or precipitation-hardened alloys have structural applications in reactors and the space program. In addition, it has been discovered that small coherent precipitate particles and certain solute atoms can minimize void formation in certain nickel-based alloys, making such transformations of possible importance in fast reactor materials. Finally, these alloys have been of fundamental interest in determining the basic mechanisms of radiation damage. One such alloy--copper-iron (Cu-Fe) with a few percent or less iron--appeared to satisfy the requirement of resolvable structure in the Mössbauer spectra from the three iron phases which are known to exist in this alloy system. Additional advantages of using the Cu-Fe system include:

1) Iron (Fe^{57}) is still the most practical element to use in Mössbauer spectroscopy. It allows excellent energy resolution and high intensity measurements to be made at room temperature.

2) Cu-Fe samples of the size needed and with just a few percent iron (preferably enriched in Fe^{57}) can be irradiated in fast neutron fluences of up to 10^{20} n/cm^2 without acquiring enough long-lived radioactivity to interfere with the Mössbauer spectroscopy.

3) Dilute Cu-Fe alloys have been the subject of several investigations including studies of precipitation kinetics and neutron irradiation effects by resistivity and magnetization measurements[3-5] and studies of the Mössbauer spectra of unirradiated alloy samples.[6-10] Thus, comparison of Mossbauer results with those of other measurement techniques can be made.

B. Literature Review

1. Mössbauer Effect Applications in Alloys Including Phase Analysis

The application of Mössbauer spectroscopy to the study of dilute impurities in metals, metallic alloys, and phase analyses of alloys has been reviewed by Gonser[11] and Wertheim.[1] A majority of the papers on dilute alloys are concerned with the local magnetic and electronic effects of the impurity atoms. Only those papers which are pertinent to this work are reviewed here.

Of particular interest to this study are a series of papers on Mössbauer investigations of dilute concentrations of Fe in the noble metals Cu and Au, including several of their alloys. Gonser et al.[6] were the first to apply Mössbauer spectroscopy to identify the three known iron phases in dilute Cu-Fe alloys: Fe in solid solution with Cu, paramagnetic γ-Fe precipitate, and ferromagnetic α-Fe precipitate. More recently, Bennett and Swartzendruber[7] discovered a possible fourth

'phase' of iron represented by a doublet in the room temperature Mössbauer spectrum of a solution annealed and quenched Cu-0.5% Fe alloy. This doublet 'phase' was not recognized in the earlier work of Gonser et al., since in their somewhat broadened spectrum the right-hand component of the doublet was hidden at the base of the more intense central line produced by Fe in solid solution with Cu. The left-hand component of the doublet, which is essentially coincident with the γ-Fe precipitate singlet evident in well annealed samples, was thought by Gonser et al. to be due to γ-Fe formed during the quench.

Bennett and Swartzendruber initially interpreted the doublet in quenched samples as arising from magnetic interactions within Fe clusters. More recent work by Reno and Swartzendruber[12] and Window[8-10] have shown the doublet to be quadrupolar in origin; i.e. it results from the interaction of the 14.4 Kev Mössbauer state's quadrupole moment with the electric field gradient (EFG) produced by a non-symmetric electronic charge distribution about the Fe^{57} nucleus. The charge asymmetry is believed to be caused by Fe pairs and larger Fe clusters within the Cu lattice.

Because of the greater solubility of iron in gold, the dilute Au-Fe alloy system allows for the study of Fe cluster interactions over a wider range of iron concentrations. As a result there have been several papers concerned with electrostatic and magnetic interactions of Fe solute atoms within the Au lattice.[13-16] A doublet analogous to that observed in Cu-Fe has also been observed in the room temperature spectra of Au-Fe alloys. The Au-Fe doublet also appears at the base of a more intense central line produced by dispersed iron atoms in the gold

lattice and has been interpreted by Violet and Borg,[13] Ridout,[14] and Window[15,16] as arising from quadrupole interactions caused by iron nearest neighbors.

In the area of phase analysis, Mössbauer studies have been carried out on such alloy systems as iron-carbon and steel,[17-24] copper-nickel-iron,[7,25] iron-molybdenum,[26], copper-cobalt,[27] copper-iron[6-10] and nickel-gold.[28] In addition, several order-disorder transitions have been studied by Mössbauer techniques including those occuring in such alloys as Fe-Ni,[29] Ni_3Mn,[30] Au_4Mn,[31] AlFe,[32,33] and Fe-V.[34] In these experiments the Mössbauer effect has been demonstrated to be an effective technique for studying the formation, structure and relationships of various phases in alloys.

The Mössbauer effect seems to be particularly suited for the study of precipitation reactions in alloys because it is capable of detecting minor constituents as well as extremely small particles. The work of Gonser et al.[6] and Bennett and Swartzendruber[7] initially demonstrated the sensitivity of this method for determining the fraction of iron in the two precipitate phases in Cu-Fe alloys. Window's recent publication[10] and the present study extends their work by reporting on precipitation processes of γ-Fe during the early stages of aging in the copper-rich Cu-Fe system.

In the ternary $Cu_{1-x}(Ni_{0.7}Fe_{0.3})_x$ system, Nagarajan and Flinn[25] demonstrated that the segregation of these alloys into two phases occurs by nucleation of precipitate particles and not by 'spinoidal decomposition' as originally thought. The precipitation of Co from Cu-Co solid solutions has been studied by Nasu et al.[27] using Co^{57} in a 2.0% Co source experiment. They were able to not only

determine the fraction of cobalt precipitated but also the average size of the precipitate particles by observing their superparamagnetic[35] behavior as a function of temperature. In yet another precipitation ME experiment, Marcus et al.[26] showed that annealing of random solid solutions of Fe-Mo at 650°C results in the precipitation of Fe_2Mo.

Thus, there is ample evidence that Mössbauer spectroscopy can be an effective technique for phase identification in alloys containing Mössbauer nuclides, especially Fe^{57}. The first part of the present study is concerned with characterizing precipitation processes in a Cu-0.6 at % Fe alloy as a function of heat treatment.

2. Mössbauer Spectroscopy Applications to the Study of Radiation Effects

The use of Mössbauer techniques to study lattice defects was first proposed by Gonser and Wiedersich.[36] Since then there have been several papers describing ME measurements of radiation induced defects in a variety of materials. These measurements have been reviewed by Ullrich,[37] Wertheim[2] and Schroeer et al.[38]

In general, ME radiation damage experiments can be classified into two distinct categories: (1) those in which the Mössbauer nuclide is introduced into a defect environment as a result of its production and (2) those in which the Mössbauer nuclide is used to probe the effects of bombarding radiation but is not produced in the process. The former category has by far received the greatest attention since many of the techniques used to produce Mössbauer source nuclei also cause their displacement from their original lattice position. Methods used to produce a coupled source nuclide-radiation defect include radioactive decay (e.g. Ref. 39), Coulomb excitation (e.g. Ref. 40), ion

implantation (e.g. Ref. 41), thermal neutron activation[42-44] and other nuclear reactions (e.g. Ref. 45).

In principle the objective of such experiments has been to create a simple one-to-one correspondence between Mössbauer source nuclide and defect. In practice such radiation damage effects have proved to be quite elusive, especially in metals. The lack of significant effects in metallic lattices suggests that the primary displaced or implanted Mössbauer nuclide returns to its normal lattice site, probably through replacement collisions (See for example Dedericks et al., Ref. 46). Such replacement collisions have been demonstrated by Berger[43] and Czjzeck and Berger[47] who observed the order-disorder effects in FeAl and Fe_3Al Mössbauer sources caused by gamma recoil following thermal neutron activation of Fe^{57}.

The most significant changes in Mössbauer spectra of 'damaged' materials have been observed in source experiments on oxides, salts and semiconductors. Since these experiments are not of direct importance to this work, the reader is referred to the review papers given above.

To date there have been very few experiments of the second category reported in the literature. This is primarily due to the difficulty of satisfying the criteria (See pp. 2 and 3) for the observance of resolvable Mössbauer spectra from various 'damaged' configurations induced by bombarding radiation. One of the few examples of this type of application is the radiation induced disorder-order transformation studies on a 50-50 FeNi alloy performed by Gros and Pebay-Peyroula[48] using electron bombardment, and by Gros et al.[49] using fast neutrons. The Mössbauer results showed that the radiation caused the growth of a new phase with large magnetic anisotropy and a

partially resolved spectrum exhibiting quadrupole as well as magnetic hyperfine structure.

The effects of radiation, especially fast neutrons, on precipitation processes in alloys have been studied by resistivity,[5] magnetization[5,50] and electron microscopy[51] techniques, but not by Mössbauer spectroscopy until this present work. Results to date suggest that fast neutrons have possibly one or more of the following effects on precipitation hardening alloys: 1) precipitation of solute atoms from supersaturated solid solution caused by radiation-enhanced nucleation and/or diffusion; 2) dissolution of existing precipitate particles by displacement spikes; and 3) conversion of coherent precipitate particles into incoherent particles. All three effects are competitive and are believed to occur simultaneously during fast neutron irradiation, although enhanced precipitation is usually masked by the dissolution of precipitates caused by displacement spikes or cascades.

The dilute Cu-Fe system with its two distinct precipitate phases seems to be well suited for a ME investigation of fast neutron effects on precipitation processes. In this work the Mössbauer nuclide Fe^{57} is used as a probe in Cu-Fe absorbers to determine the fraction of iron existing in the precipitate and solid solution phases both before and following irradiation.

CHAPTER II

BACKGROUND

A. Origin and Properties of the Fe^{57} Mössbauer Effect Line Structure

In iron the Mössbauer effect (ME) is observed for recoilless gamma-ray transitions between the ground state of the Fe^{57} nucleus and its first excited state at an energy E_o of 14.4 Kev. Recent values for the properties of these two states are given by Stevens.(52) The first excited state has a half-life of 97.7 ns, a magnetic dipole moment μ_e = -.155 nuclear magnetons, a quadrupole moment Q_e = 0.20 barns and a nuclear spin I = 3/2. The Fe^{57} ground state has a magnetic dipole moment μ_g = +.904 nuclear magnetons and a spin I_g = 1/2.

The nuclear properties of Fe^{57} allow the observation of Mössbauer line structure through the three hyperfine interactions involving the nucleus and atomic electrons. These are observed as the isomer shift, magnetic hyperfine splitting and electric quadrupole splitting in Mössbauer spectra. These three interactions acting separately or in combination, along with the inherent shape of the gamma-resonance line, determine the line structure observed in Fe^{57} Mössbauer spectra.

1. Resonant Line Properties

a. Line Shape.--As shown by Margullies and Ehrman(53) the shape of the transmission energy distribution is a function of an

energy integral over the gamma ray's emission distribution (which is Lorentzian in shape) multiplied by an exponential function containing the resonance cross section for the absorber. For a source with no resonant self-absorption and thin absorber (effective thickness $T << 1$; see Equation II.1 below), the transmission line* shape is Lorentzian with a width of twice that of the excited state's width, $2\Gamma_o$. In the limit of zero absorber thickness the resonant line's intensity is proportional to the absorber's effective thickness, given by

$$T = nf\sigma_o t \qquad \text{(II.1)}$$

The symbols are defined as f, the recoil-free fraction of the absorber; n, the number density of resonant atoms in the absorber; σ_o, the maximum resonant absorption cross section; and t, the absorber thickness. In absorbers of finite thickness, the exponential absorption term in the transmission integral distorts the transmission energy distribution of the gamma beam causing line saturation and line broadening. Fraunfelder et al.[54] have found that for $T < 5$ the shape of the transmission line is Lorentzian to within 1/2% but with a broadened line width approximated by

$$\Gamma \cong 2\Gamma_o\ (1.00 + 0.135T),\ 0 \leq T < 5 \qquad \text{(II.2)}$$

Additional broadening occurs from equipment noise and resonant atom inhomogeneities in the source and absorber.

---

*All ME spectra in the present work were taken in the transmission or absorption geometry.

b. Recoil-free Fraction.--The recoil-free fraction, f, appearing above in the expression for effective thickness is singly the most important parameter in Mössbauer spectroscopy. It is a measure of the probability for zero phonon processes (i.e., recoilless emission and absorption events) in a given material, and thus determines the magnitude of the effect. The recoil-free fraction is given by[55]

$$f = \exp[-4\pi^2\langle x^2\rangle/\lambda^2] \qquad \text{(II.3)}$$

where $\langle x^2\rangle$ is the mean square amplitude of vibration of the nucleus in the direction of the γ beam and λ is the wavelength of the radiation. Using the Debye model for the case of an infinite crystal lattice, the recoil-free fraction can be approximated by[55]

$$f \simeq \exp[-6(E_r/k\theta_d)(T/\theta_d)], \text{ for } T \gtrsim \theta d/2 \qquad \text{(II.4)}$$

where $E_r = E_o^2/2Mc^2$ is the free-nucleus recoil energy, T the ambient temperature of the source or absorber, and θ_d the Debye temperature. Consideration of Equation (II.4) indicates that $k\theta_d$ should be greater than E_r and T less than θ_d in order to obtain a significant effect.

The Debye model and thus Equation (II.4) are approximations to the actual lattice frequency spectrum and apply in the strictest sense to monatomic crystals. However, the use of an "effective" Debye temperature for more complicated crystals has proven useful in characterizing Mössbauer recoil-free fractions. For dilute impurities in metals such as Fe in copper, the "effective" Debye temperature is given by[56]

$$\theta_D^{(I)} = \left(\frac{M_H}{M_I}\right)^{1/2} \theta_D^{(H)} \qquad \text{(II.5)}$$

where M_I and M_H are the impurity and host masses and $\theta_D^{(H)}$ the Debye temperature of the host lattice. For Fe^{57} in copper Equation (II.5) yields an 'effective' Debye temperature of about 365°K using the value of 343°K given by Kittel[57] for the Debye temperature of copper. Since $E_R \tilde{=} 1.95(10)^{-3}$ev and $k\theta_D \tilde{=} 3.15(10)^{-2}$ev, the condition $k\theta_D > E_R$ is easily satisfied. Also since $T<\theta_D$ the Mössbauer effect for Fe in Cu is readily observable at room temperature (i.e., from Equation II.4, $f \simeq .74$). The measured f-value for isolated Fe in Cu is about 0.73 at room temperature.[58]

2. Resonant Line Area and Phase Analysis

In order to perform quantitative analysis of metallurgical phases using ME spectroscopy, it is necessary to relate one or more spectral parameters to the concentration of atoms existing in a given phase. As discussed in the previous section the spectral line intensity for a thin absorber is directly proportional to the absorber's effective thickness, and thus to the Mössbauer isotope concentration. However, the absorption area is a better parameter since it is insensitive to source line shape and instrument resolution, and tends to saturate less rapidly with increasing absorber thickness than the intensity.[59-61] This study makes use of spectral area ratios to determine the relative iron phase concentrations in copper as a function of thermal treatment and fast neutron exposure.

The background corrected area under a well resolved absorption line associated with an ME isotope of given phase can be expressed as[60]

$$A_i = f_s \int_{-\infty}^{\infty} dE[1-e^{-T_i k_i(E)}] \qquad \text{(II.6)}$$

In this expression f_s is the recoil-free fraction for the source, T_i is the effective absorber thickness (Equation II.1) for the ith phase or resonant atom configuration, and $k_i(E)$ is the energy dependent part of the resonance absorption cross section which is given in the Breit-Wigner equation as

$$k_i(E) = \frac{(\Gamma/2)^2}{(E-E_i)^2+(\Gamma/2)^2} \qquad \text{(II.7)}$$

Here, Γ is the total width at half maximum of the excited state's energy distribution and E_i is the transition energy centroid. The resonance absorption cross section is then given by

$$\sigma_i(E) = \sigma_0 k_i(E) \qquad \text{(II.8)}$$

where σ_0, the cross section's maximum value, is as defined in many references; e.g. see p. 12 of Reference (55).

When hyperfine interactions split the absorption spectrum of the ith phase into N lines, the cross section given by Equation (II.8) can be written as

$$\sigma_i(E) = \sigma_0 \sum_{j=i}^{N} P^{(j)} k_i^{(j)}(E) \qquad \text{(II.9)}$$

where $P^{(j)}$ is the probability for the jth hyperfine transition between the split excited and ground states). The $P^{(j)}$'s are normalized to unity; i.e. $\sum_{j}^{N} P^{(j)} = 1$, so that the energy integral of the cross section remains independent of splitting. The origins of such splittings are discussed in the next section.

When there are several phases present, the generalized form of Equation (II.6) becomes

$$A = f_s \int_{-\infty}^{\infty} dE[1-\exp(-\sum_i T_i k_i(E))] \qquad (II.10)$$

where the sum in the exponent is over the number of phases present. If the absorption lines of one or more of the phases are split, sums over the split components must be included as in Equation (II.9). Assuming that the individual components are well resolved, the partial areas given by Equation (II.6) can be considered separately, in which case for a thin absorber ($T_i << 1$) the exponential in Equation (II.6) can be expanded to give

$$A_i \simeq f_s \int_{-\infty}^{\infty} T_i k_i(E) dE = \frac{1}{2}\pi\Gamma f_s T_i \qquad (II.11)$$

The total area under the absorption curve is then the sum over the individual areas; i.e. $A = \sum_i A_i$. Unfortunately many cases of phase analysis involve lines which aren't well resolved so that the details of overlap in Equation (II.10) must be considered. This is done in Appendix A for the Cu-Fe alloy absorbers used in the present study.

When the absorber can not be considered as 'thin' a more comprehensive evaluation of Equation (II.6) or Equation (II.10) must be made. For isolated lines an exact expression in terms of zero and first order Bessel functions has been obtained.[61] A useful expansion of A_i in terms of a power series in T_i is also available.[62] The inverse of this power series which is particularly convenient in obtaining phase concentrations can be approximated to within 1% by[62]

$$T_i \simeq \frac{A_i}{1-A_i/4} \; ; \quad Ai \leq 4/3 \tag{II.12}$$

where $A_i = A_i/(\frac{1}{2}\pi\Gamma_i f_s)$.

To obtain the relationship between absorption line areas and phase concentrations, consider an absorber containing several phases. Let N_i be the atom density of the ME element in the ith phase and a, the isotopic abundance of the ME nucleus. The expression for the effective absorber thickness (Equation II.1) for the ith phase becomes

$$T_i = f_i N_i a \sigma_o t$$

Combining Equation (II.12) and T_i from above gives

$$(a\sigma_o t) f_i N_i = \frac{A_i}{1-A_i/4} \tag{II.13}$$

and similarly for the other phases.

Experimentally it is much easier to measure relative rather than absolute areas. Dividing the above expression by the effective thickness for the jth phase yields the desired equation for relative phase concentrations,

$$N_i/N_j = R_{ij}(f_j/f_i)\left[\frac{1-A_j/4}{1-A_i/4}\right] \tag{II.14}$$

In the above expression R_{ij} is the ratio of spectral areas for the ith and jth phases; i.e. $R_{ij} = A_i/A_j$. The ratio in the brackets containing the absolute areas in the A_i's is a correction factor which approaches unity for 'thin' absorbers. Systematic errors which enter into the determination of absolute absorption line areas tend to cancel in the correction factor, so that the extreme care usually required in absolute

ME area measurements is not necessary in measurements of relative phase concentrations. If the recoil-free fractions for the phases are approximately equal and the thin absorber criterion met, the ratio A_i/A_T, where A_T is the total area of the spectrum, can be used to determine the relative concentration of the ith phase. Given the total ME element concentration in the absorber, one can then determine its concentration in the phases present.

3. Hyperfine Interactions: Summary of Theory

Three nuclear-atomic interactions due to near neighbors affect the Fe^{57} nuclear energy levels. These are the isomer shift, which measures the s-electron density at the nucleus; the electric quadrupole interaction, which measures the distortion of the iron electrons and the lattice from spherical and cubic symmetry, respectively; and the magnetic hyperfine interaction, which measures the effective magnetic field at the Fe^{57} nucleus. A brief description of these interactions and their observation in ME spectra is given below. More detailed discussions of these interactions in connection with Mössbauer spectroscopy are contained in several excellent reviews (e.g., see References 63 and 64).

a. Isomer Shift.--This is a nuclear volume effect resulting from the fact that the ground and excited states of the nucleus have different effective charge radii. Therefore, the electrostatic interaction energy caused by the overlap of electronic and nuclear charge distributions is different for the two levels. As a result, the gamma ray energy is shifted by an amount depending on the source and absorber's

s-electron density. Neglecting relativistic effects the isomer shift, IS, is given by

$$IS = \frac{2\pi}{5} Ze^2 \delta\langle R^2\rangle [|\psi_a(0)|^2 - |\psi_s(0)|^2] \qquad \text{(II.15)}$$

where $\delta\langle R^2\rangle$ is the difference between the mean square nuclear charge radii in the isomeric excited and ground states, Z is the nuclear charge, and $|\psi_a(0)|^2$ and $|\psi_s(0)|^2$ are the s-electron densities at the nuclear sites in the absorber and source, respectively.

For heavy elements relativistic effects become important. Correction factors accounting for such effects have been given by Shirley.[65] Such corrections can be as large as 30 percent for heavier nuclei.

The isomer shift is measured by determining the shift of the centroid of a Mössbauer spectral component with respect to zero velocity (i.e. zero Doppler shift energy of the emitted gamma). In order to obtain information on s-electron densities, relative isomer shifts for a series of compounds of a given ME isotope are measured with respect to a standard source or absorber. In this manner, changes in s-electron densities can be determined and referenced to the calculated s-electron density for a known electronic configuration of the ME element (e.g., that of a pure ionic state).

The relative isomer shifts for Fe^{57} as an impurity in 3d transition metal host lattices have been measured in several sources.[66] The results show that the charge density at the impurity nucleus is dependent upon the number of 3d electrons, as well as on the 4s character of the host. An exact interpretation has not yet been given owing to the difficulty of calculating the distribution of electrons

in the 3d band and the 4s conduction band. Using the data presented by Walker et al.,[67] the isomer shift decrease of about .31 mm/sec observed in this work and by others[7,10] in going from Fe^{57} in copper to Fe^{57} in FCC γ-iron precipitates corresponds to an increase of about 6.5% in the s-electron density at the Fe^{57} nucleus. According to Qaim[66] this increase is probably caused by a reduction in 3d electron screening effects when going from Cu to γ-Fe. An increase in the 4s character of the surrounding lattice would also contribute to the observed effect. Since there is only about a 0.5% decrease in lattice parameter from pure Cu to γ-Fe, it is unlikely that the inter-atomic spacing difference would make a significant contribution.

b. Magnetic Hyperfine Splitting.--Magnetic hyperfine splitting (hfs) arises from the interaction between the nuclear magnetic moment, μ_I, and the magnetic field at the nucleus. The Hamiltonian for this interaction can be written

$$H_m = -\mu_I \cdot H_{eff} \qquad \text{(II.16)}$$

where H_{eff} refers to the effective magnetic field at the nucleus. The interaction splits the nuclear state with spin I into (2I+1) sub-levels with the eigenvalues

$$E_m = -g\mu_n H_{eff} m_I \qquad \text{(II.17)}$$

where g is the nuclear g-factor, μ_n the nuclear magneton, and m_I is the magnetic quantum number which takes the values I, I-1,..., -I.

In the ME isotope Fe^{57} the spin 3/2 excited state is thus split into four sublevels as shown in Figure II-1 (left side). The multipolarity of the 14.4 Kev gamma is almost exclusively M1,

restricting transitions to $\Delta m_I = 0, \pm 1$. The allowed transitions result in a 6-line Zeeman pattern as shown in Figure III-2 for an α-iron foil absorber. The angular dependence of the six transitions is as follows:

Transition	m	Angular Distribution
$\pm 3/2 \rightarrow \pm 1/2$	± 1	$(3/4)(1+\cos^2\theta)$
$\pm 1/2 \rightarrow \pm 1/2$	0	$\sin^2\theta$
$\pm 1/2 \rightarrow \pm 1/2$	± 1	$(1/4)(1+\cos^2\theta)$

Here θ is the angle between the magnetic field and the direction of propagation of the gamma-ray. If the internal fields are randomly oriented to the line of observation of the gamma ray, as in a polycrystalline aggregate, then an average over the above distributions leads to a ratio of 3:2:1:1:2:3 for the intensities of the six lines. An orientation of $\theta = 90°$ leads to a ratio of 3:4:1:1:4:3, while one of 0° results in a 3:0:1:1:0:3 intensity ratio. Finite thickness effects, instrumental broadening and internal field distributions will modify these theoretical intensity ratios. Such a modification occurs for the α-iron standard used in the velocity calibration of our spectrometer where cold rolling effects in the thin foil and saturation effects resulted in the outer four lines deviating from the theoretical intensities expected for randomly oriented fields.

The effective field at the Fe^{57} nucleus is usually large for iron in a magnetic material below its transition temperature; e.g., $H_{eff} = 330$ kG for Fe in metallic form at room temperature.[68] The origin of this field in ferromagnetic materials has been investigated theoretically by Watson and Freeman.[69] The effective fields observed for Fe in metallic materials arise largely from core and conduction electron polarization caused by unpaired 3d electrons.

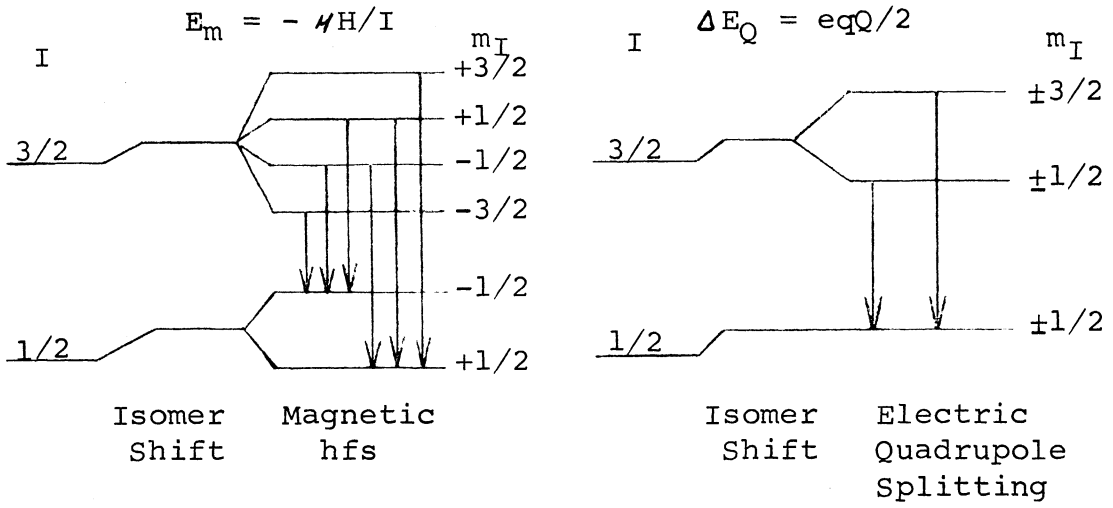

Figure II-1.--Magnetic hf splitting of the ground and first excited state of Fe-57 (left) and quadrupole splitting of the first excited state of Fe-57 (right).

In the present study carried out at room temperature, only α-iron precipitates that form in well aged and cold-worked Cu-Fe samples exhibit a magnetic hfs structure in their Mössbauer spectra. Room temperature is well above the magnetic transition temperatures for Fe in any of its FCC 'phases' with copper.[10,70] Therefore, any multiple line structure observed for the dilute Cu-Fe alloy samples in this study, with the exception of the well-known α-iron lines, will originate from isomer shift differences and/or electric quadrupole effects from Fe^{57} in different near neighbor configurations.

c. Electric Quadrupole Splitting.--Electric quadrupole splitting arises from the interaction between the nuclear quadrupole moment, Q, and the electric field gradient, $\bar{\nabla}\bar{E}$, created by the electronic environment of the nucleus. In Fe^{57} the electric quadrupole interaction splits the first excited state (I=3/2) into two doubly degenerate sublevels as shown in Figure II-1 with the eigenvalues

$$E_m = \frac{eQV_{zz}}{4I(2I-1)} [3m_I^2 - I(I+1)](1+\eta^2/3)^{1/2} \qquad (II.18)$$

$$m_I = \pm 3/2, \pm 1/2$$

In Equation (II.18) V_{zz} is the z component of the electric field gradient (EFG) tensor in the crystal's principal axis system and η is the asymmetry parameter given by

$$\eta = \frac{V_{xx} - V_{yy}}{V_{zz}} , \quad 0 \leq \eta \leq 1 \qquad (II.19)$$

The ground state in Fe^{57} has no quadrupole moment since $I_g = 1/2$. Thus, the transitions between the excited and ground states give rise to a two line Mössbauer pattern with a quadrupole splitting of

$$\Delta E_Q = |E_{3/2} - E_{1/2}| = \frac{eQV_{zz}}{2}(1+\eta^2/3)^{1/2} \qquad (II.20)$$

For cubic or spherical symmetry each of the EFG components will be zero and the quadrupole interaction vanishes. If the field gradient has axial symmetry $V_{xx} = V_{yy}$, $\eta = 0$ and $\Delta E_Q = eQV_{zz}/2$. In this case the angular dependence of the two transitions is as follows:

Transition	Angular Dependence
$\pm 3/2 \rightarrow \pm 1/2$	$3(1 + \cos^2\theta)$
$\pm 1/2 \rightarrow \pm 1/2$	$5-3\cos^2\theta$

Here θ is the angle between the principal axis of the EFG and the propagation direction of the gamma-ray. For a randomly oriented polycrystalline material the relative line intensities are 1:1 (in the thin absorber limit).

The origin of electric field gradients in metals and alloys has been discussed by Watson et al.[71] The EFG arises from two sources, V_{zz}^{loc} due to electrons within the atomic sphere centered at the nucleus and V_{zz}^{latt} due to charges outside the atomic sphere on near neighbors. The resultant EFG and the asymmetry parameter can be expressed in the forms:

$$V_{zz} = (1-\gamma_\infty)V_{zz}^{latt}+(1-R)V_{zz}^{loc} \qquad \text{(II.21a)}$$

and

$$\eta V_{zz} = (1-\gamma_\infty)\eta^{latt}V_{zz}^{latt}+(1-R)\eta^{loc}V_{zz}^{loc} \ , \qquad \text{(II.21b)}$$

where (1-R) and $(1-\gamma_\infty)$ are the Sternheimer shielding and antishielding factors, respectively.[72] These account for the polarization of the spherically symmetric core electrons caused by the asymmetric charge distributions of p- or d-electrons in the case of V_{zz}^{loc} and by lattice charges in the case of V_{zz}^{latt}. In general, V_{zz}^{loc} from valence electrons in non-symmetric orbitals will be large compared to V_{zz}^{latt} due to the $1/r^3$ dependence of the EFG. However, the polarization factor γ_∞ may be quite large providing significant enhancement of the lattice contribution, V_{zz}^{latt}.

The observation of quadrupole effects for Fe impurities in cubic alloys using ME spectroscopy has been limited to a few systems and until very recently[15] little attention has been given to investigating their origin. The interpretation of quadrupole effects in Au-Fe and dilute Cu-Fe alloys, which display relatively large quadrupole splittings for metallic systems, is discussed in the following section.

B. Interpretation of Mössbauer Spectra for Fe^{57} Solute Atoms in Copper and Gold

The problems encountered in analyzing ME spectra for Fe^{57} in alloys are complex and varied. These are brought about by inhomogeneities in the near neighbor configurations of the iron solute atoms which can cause a distribution of observed isomer shifts and quadrupole and magnetic hyperfine splittings. In this section current interpretations of room temperature Mössbauer spectra of dilute Cu-Fe alloys* and the similar alloy system, Au-Fe, are discussed. Although the majority of ME studies of these two alloy systems have been concerned with low temperature magnetic properties, only those results which are germane to an understanding of the room temperature spectra are considered here.

---

*Before 1972 ME results existed for solution annealed and well-aged Cu-Fe alloys only. These results are considered in this section. ME spectra obtained in the present study for aged Cu-0.6%Fe samples with a variety of ageing histories and their interpretation are given in Chapter IV. Window's[10] recent study of aged Cu-1.0%Fe alloy samples is also considered in Chapter IV in conjunction with the present work.

1. Au-Fe Alloys

Owing to its large solubility for iron and relatively large observed quadrupole splittings, the Au-Fe system has proven to be easier to study than its noble metal counterpart, Cu-Fe. The spectra above the ordering temperature in AuFe consist of an apparent single line and doublet, both of which were interpreted by Violet and Borg[13] in terms of quadrupole interactions due to near-neighbor iron atoms. The broadened central singlet has been associated with isolated Fe atoms experiencing quadrupole interactions with further than nearest-neighbor Fe atoms. Ridout[14] interpreted the asymmetry and broadening of the doublet to be a consequence of there being a distribution of numbers and configurations of iron nearest-neighbors.

A mechanism to produce the large electric field gradients observed in these alloys was proposed by Window[15] on the basis of a study of Fe^{57} in AuX alloys, X being a 3d impurity. The correlation between quadrupole splittings and residual resistivities observed in these alloys led Window to suggest that the electric field gradients at an Fe^{57} impurity arise from a distortion of the iron screening charge from cubic symmetry due to the increased density of states at the Fermi level on an X impurity in the nearest neighbor shell. The screening charge can be described in terms of the Thomas-Fermi model.[73] Its distortion in the presence of another 3d impurity can be explained by Friedel's virtual-bound-state (vbs) theory.[74] In order to approximate the effects of this charge distortion upon the electric field gradient, Window[15,16] invoked an effective point charge model previously used by Preston et al.[75] to explain quadrupole effects in V-Fe alloys. In this model the distortion of the screening electrons ($\sim$ seven 3d

electrons for Fe in Au or Cu) in the presence of an Fe (or X) neighbor is simulated by an effective point charge localized on the neighboring impurity site.

The magnitude of the screening charge distortion (and thus the quadrupole splitting) will depend upon the increase in the density of states on the impurity neighbor. Thus, according to Window, it is only for d impurities with a narrow virtual bound state accommodating ten 3d electrons that the distortion is large enough to produce resolvable quadrupole splittings. A further consequence of this model is that the effective point charge should decrease with increasing number of Fe (or X) impurity neighbors. Window[16] was able to explain the changes in the doublet structure for Au-Fe alloys with increasing Fe concentrations (up to $\sim$ 30%) by using a reducing point charge model to account for changes in iron screening effects occurring for an increasing number of Fe nearest neighbors (i.e., increased clustering).

2. Cu-Fe Alloys

The interpretation of room temperature spectra from dilute Cu-Fe alloys is complicated by excessive iron clustering caused by the very low solubility of iron in copper. Similar to the Au-Fe system, spectra from solution annealed Cu-Fe alloys display a 'cluster' doublet at the base of a central resonance line due to isolated Fe atoms (e.g., see Figure IV-1) as was first noted by Bennett and Swartzendruber.[7] Early controversy over the origin (magnetic or quadrupolar) of the doublet's splitting has been experimentally resolved by Reno and Swartzendruber[12] in favor of a quadrupole interaction. The electric

field gradient responsible for the interaction has been interpreted by Window[8] as having the same origin as described above for Au-Fe alloys.

Dilute Cu-Fe alloys ($\tilde{<}$ 1% Fe) which are rapidly quenched from solution temperature display a reasonably well defined doublet with a splitting of approximately .58 mm/sec and area fraction of 0.3 to 0.4.[7,8] Window[8] associates this doublet with Fe pair formation occurring during the quench. By reducing the quenching rates, Window found evidence for increased iron clustering from ME spectra taken at both 300°K and 1.4°K. From spectra taken at 300°K, he observed that with progressively less efficient quenching the doublet shifts slightly to lower energy, decreases slightly in splitting, and increases in area fraction--all signs of Fe clustering.

The small decrease in the doublet's splitting for slower quenches can be interpreted in terms of the effective point charge model used by Window[15] to simulate the screening charge distortion occurring in Au-Fe alloys when Fe clusters of a pair or more form. In the way of illustration, this model is applied in Appendix B to calculate the relative quadrupole splittings for several Fe cluster configurations that might occur in dilute Cu-Fe alloys. From the results of Table B-1 it is seen that the doublet decreases in splitting but remains quite well resolved for Fe^{57} with up to five iron neighbors in copper.

Concurrent with the doublet's decrease in splitting, Window observed a decrease in the doublet's isomer shift with increased clustering. This is to be expected since the position of the spectral component for large γ-iron precipitate particles is about -0.33 mm/sec with respect to the isolated iron (solid solution) component. The resultant effect of a decrease in splitting and isomer shift is that the

low energy line of the doublet remains well defined, while the high energy line broadens and becomes masked by the central solid solution component.

The low temperature results of Window[8] also indicate the occurrence of iron clustering during quenching from solution temperature. Window fit the complex magnetic hfs spectra obtained at 1.4°K to an approximate distribution of hyperfine fields.[76] Peaks in the field probability distribution can be associated with internal magnetic fields occurring for iron with n = 0, 1, 2 or more Fe nearest neighbors. A large peak at about 80 kOe was assigned to isolated iron atoms, while broader peaks at higher fields were related to iron atoms in clusters of a pair or more. These results indicate that below ordering temperatures iron atoms in small clusters or isolated in copper couple ferromagnetically in contrast to the anti-ferromagnetic coupling observed in large γ-iron precipitate particles.[70] The fraction of iron with and without Fe nearest neighbors was approximated from both the 1.4°K hyperfine field distributions and the spectral area fractions obtained at 300°K; results from both methods agree reasonably well over the range of quenching rates.

If dilute Cu-Fe alloys are aged at intermediate temperatures, another component appears in their room temperature ME spectra.[7] This component is a single resonance line which is essentially coincident with the low energy (left) member of the 'cluster' doublet and is produced by Fe^{57} in FCC γ-iron precipitate particles. In well-aged samples which have subsequently been cold worked, the γ-iron precipitates are transformed to BCC α-iron precipitates which exhibit the well known six-line iron hfs spectrum.[7]

C. Metallurgy of Copper-rich Cu-Fe Alloys

Copper-rich Cu-Fe alloys belong to the precipitation hardening category of alloys as can be seen from the phase diagram[77] in Figure II-2. The solubility of iron in copper reduces from about 3.0 at.% at 1060°C to practically zero at room temperature. Thus, only a small amount of Fe can be retained in solid solution in pure Cu.

From the phase diagram it is seen that below the eutectoid temperature (850°C), the iron-rich phase in equilibrium with the copper-rich solid solution consists of BCC α-Fe. Above 850°C, for alloys containing approximately 1.4 at.% or more Fe, the equilibrium iron-rich phase is FCC γ-Fe. Aging below the solvus initially produces the γ-Fe precipitate phase as is discussed below.

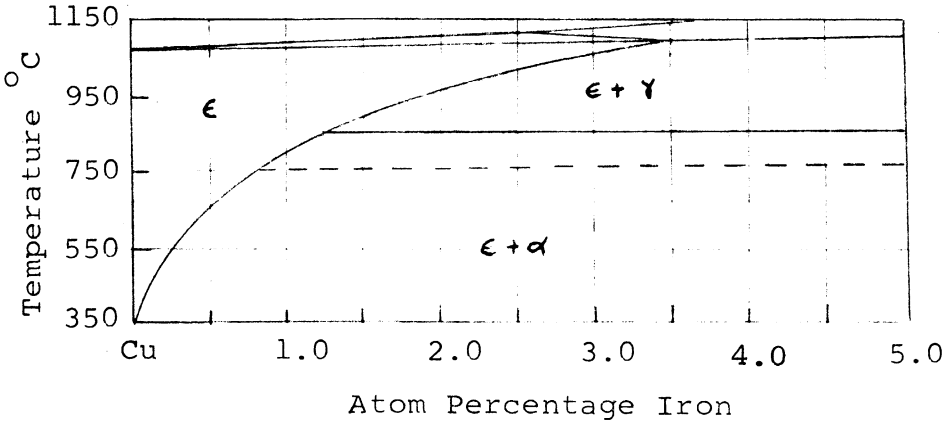

Figure II-2.--Copper-rich Cu-Fe phase diagram

Precipitation processes in the Cu-rich Cu-Fe alloy system have been studied by several diverse techniques including the measurement of resistivity,[3] hardness[78] and magnetization[3,4,79] as well as X-ray diffraction,[4,78] electron microscopy,[4,78,85] and very recently Mössbauer spectroscopy.[10] Early aging experiments[79-83] showed that the initial precipitate was paramagnetic (at room temperature) and could be made ferromagnetic by cold working or extended aging at high temperatures. This led Smith[83] to suggest that the initial paramagnetic precipitate was FCC and coherent with the Cu matrix, while the ferromagnetic precipitate could be identified with the stable BCC α-iron structure.

Later attempts to verify Smith's suggestion were made by Denney[4] and Newkirk.[78] Measuring the saturation magnetization of 2.4% Fe samples which were aged and then cold worked to effect a γ-α transformation, Denney followed the isothermal precipitation of Fe from solid solution in the temperature range 600-800°C. From these measurements he concluded that precipitation proceeded as a diffusion limited process characterized by an activation energy of 1.65 ev and a time exponent of 3/2. X-ray diffraction studies by Denney[4] revealed that the paramagnetic γ-phase probably forms coherently with the parent Cu lattice on the {111} and {100} planes, transforming under plastic deformation to a ferromagnetic body-centered structure. Newkirk[78] from Debye-Scherrer X-ray patterns concluded that the FCC iron-rich precipitate phase possessed a lattice constant of a_o = 3.590 Å and was identically oriented with the copper-rich solid solution phase (a_o = 3.615 Å).

Further studies of precipitation processes in dilute Cu-Fe alloys were performed by Boltax.[3] Using electric resistivity and saturation induction measurement techniques, he detected the occurrence of two distinct precipitation processes in furnace cooling experiments: (1) the formation and growth of a coarse FCC Fe precipitate (possibly incoherent) above the eutectoid temperature which transforms spontaneously to α-iron at 850°C, and (2) the formation and growth of coherent γ-iron precipitate below 850°C which remains indefinitely stable. Boltax also studied the precipitation kinetics of quenched 1.7% Fe samples during isothermal aging in the temperature range 200-400°C. Results from resistivity measurements analyzed by the Johnson-Mehl[84] empirical rate equation yielded a time exponent of 0.28 and activation energy of 34 kcal/mole ($\sim$ 1.5 ev), the latter value agreeing with Denney's[4] result. Based on the low value of the time exponent,* Boltax concluded that low temperature precipitation processes in Cu-Fe were probably the result of precipitate particles nucleating at dislocation loops formed by the clustering of quenched-in vacancies. He suggested Denney's high temperature aging results represented the coalescence stage of precipitate particle growth (i.e., growth of large particles at the expense of smaller, less stable ones).

The γ-α martensitic transformation has been recently studied by Easterling and Meik-Oja[85] in a Cu-1.95%Fe alloy using electron microscopy supplemented by magnetic measurements. They demonstrated that precipitation of the γ-phase for this composition occurs in the

---

*A time exponent of n = 3/2 is expected for diffusion limited growth of spherical precipitate particles.[84]

temperature range 550-750°C. Nucleation was found to occur homogeneously leading to fully coherent spherical precipitate particles.* With long aging times, γ-iron precipitates were found to grow, lose their coherency and take on a cubic shape. After prolonged annealing, stable γ-precipitates would nucleate from large cubic γ-precipitates or directly on dislocations in the matrix as well as on grain boundaries. Transformation from the γ- to α-phase was found to occur martensitically on dislocations which traversed large γ-particles of 100 Å or greater following cold working.

The characterization of incipient γ-iron precipitate formation during low temperature aging (285-400°C) using Mössbauer spectroscopy has been made in Window's recent paper[10] and in the present work. Discussion of these results is delayed until Chapter IV.

D. Effects of Fast Neutrons on Precipitation Hardening Alloys

In the past, most of the studies of radiation effects in precipitation or age-hardening alloys have been performed with the viewpoint of determining the basic mechanisms of radiation effects through the unique properties of these materials, while their possible use in reactor environments was of secondary concern. Recently it has been shown that certain nickel-based alloys[86] exhibit significantly reduced swelling compared to austenitic stainless steels in extreme fast neutron environments. It is thought that small coherent precipitate particles in such alloys reduce vacancy clustering and thereby

---

*It should be pointed out that particles smaller than about 100 Å were not resolved in their micrographs.

minimize void-swelling. Thus, with the advent of fast reactors, an understanding of the effects of radiation, especially fast neutrons and heavy charged particles, on precipitation processes in such alloys is again of some importance.

Fast neutrons are believed to have the following effects on precipitates in alloys: (a) increase of precipitation caused by enhanced nucleation and/or diffusion; (b) dissolution of precipitates caused by multiple displacements; and (c) conversion of coherent precipitates into incoherent precipitates. These effects have been reviewed by Damask.[87] Discussions of the general theory of radiation effects in materials can be found in several books (e.g., see References 88-90).

1. Simple Theoretical Considerations

Irradiation of a metal or alloy by fast neutrons will cause the atoms to be displaced from their lattice sites. The displacements are created by the scattering of a high energy neutron from a lattice atom, called the primary knock-on atom (PKA). Before coming to rest, the PKA dissipates its energy through multiple collisions with other lattice atoms which, in turn, can be displaced and initiate further collisions. The displacements occur until the initiating atom reaches a minimum or threshold energy E_d ($\sim$ 25 ev for Cu). The resulting displacement cascade is responsible for the observed effects in precipitation hardening alloys.[87] The number of such displacements in copper is estimated below from simple radiation damage theory.

Assuming elastic scattering, the maximum energy imparted to the primary knock-on by a neutron of energy En is

$$T_{max} = \frac{4A}{(1+A)^2} E_n = \alpha E_n \ , \qquad \text{(II.22)}$$

where A is the atomic mass of the target atom. If the scattering is isotropic in the center of mass system, the mean energy of the PKA will be just $T_{max}/2$. Using Equation (II.22) the mean energy may be described by

$$\bar{T} = f\frac{2A}{(1+A)^2} E_n \text{ or } f\frac{\alpha}{2} E_n \qquad \text{(II.23)}$$

where a factor f is added to account for anisotropy and inelasticity in fast neutron scattering. For Cu atoms, Dienes and Vineyard[89] give a nominal value of $f \simeq 0.6$ for reactor neutron bombardments.

A number of models have been proposed for the analysis of radiation effects. We shall use the model of Kinchin and Pease in a modified form.[91] According to this model the number of displacements originating from a PKA of energy T can be expressed as follows:

$$\nu(T) = \frac{\kappa(T-E_{in})}{2E_d} \qquad \text{(II.24)}$$

In the above expression, the damage energy $(T-E_{in})$ is the total energy available for elastic collisions, E_{in} is the energy lost to inelastic processes (e.g., electronic excitations), and the displacement efficiency κ is a correction factor which accounts for deviation from hard-sphere scattering assumed in the original model. The average number of displacements $\bar{\nu}(E_n)$ created by a neutron of energy E_n can be approximated by substituting $\bar{T}$ from Equation (II.23) into Equation (II.24) above; i.e.,

$$\bar{\nu}(E_n) \simeq \frac{\kappa(\bar{T}-E_{in})}{2E_d} = \frac{\kappa(\frac{f_\alpha}{2}E_n - E_{in})}{2E_d} \qquad \text{(II.25)}$$

The values for the parameters $(T-E_{in})$ and κ in the case of Cu have been obtained in a recent computer simulation of displacement cascades in FCC lattices.[91] In the report on this study, the damage energy $(T-E_{in})$ is given as a plot against the PKA energy T. The displacement efficiency κ in the computer model was found to be energy invariant and to have a value of about 0.81.*

The rate of production of displacements per unit volume of material in a reactor can be estimated from

$$\frac{dN}{dt} \simeq N_o \bar{\sigma}_s \phi_f \bar{\nu}_f \ , \qquad \text{(II.26)}$$

where N_o is the number of atoms per unit volume, $\bar{\sigma}_s$ is the average neutron scattering cross section, ϕ_f is the fast neutron flux density, and $\bar{\nu}_f$ is the mean number of displacements per fast neutron scattered. As an approximation, the flux density ϕ_f is taken to be that of a fission spectrum. The parameter $\bar{\nu}_f$ can be estimated using the method described above by setting E_n in Equation (II.25) equal to the average fission spectrum energy; i.e., $\bar{E}_n \simeq 2.0$ Mev.[93]

---

*The definition of displacement efficiency used here is with reference to the damage energy $(T-E_{in})$. This definition differs from the displacement efficiency defined by Beeler[92]--i.e., $\kappa(T) = \nu(T)/T$--which was found to decrease with increasing PKA energy. From the results of a computer study of "displacement spike" effects, Beeler concluded that this decrease was primarily caused by recombination of vacancies and interstitials from different collision events; i.e., interference effects of overlapping branches of the cascade.

For neutrons of this energy, the average PKA energy $\bar{T}$ given by Equation (II.23) is about 36 Kev. Using this value and the computer generated plots of Torrens and Robinson[91] a damage energy $(\bar{T}-E_{in}) \simeq 30$ Kev is obtained. From Equation (II.25), the average number of displacements per fast neutron is then about 480. For the high flux irradiations in this study (see Table III-2), Equation (II.26) yields a damage rate of approximately $2.8(10)^{15}$ displacements per cm^3-sec or $3.4(10)^{-8}$ displacements per atom-sec. The value of the scattering cross section $\bar{\sigma}_s$ used in the above calculation is 3 barns.[94]

The simple calculation of $\bar{\nu}(T)$ above has not considered such effects as vacancy-interstitial recombination, annealing in "thermal spikes,"[95] channeling of displaced ions between preferential lattice planes, extreme mixing of atoms in "displacement spikes,"[96] or replacement collisions at low energies. Thus, the 480 defects produced by a 2.0 Mev neutron is at best an estimate of the initial number of vacancy-interstitial pairs formed per PKA. In comparison, the computer study of Beeler[92] yielded a $\nu(T)$ value of about 300 displacements from 2.0 Mev reactor neutrons. Also, the results from many experimental studies in which the displacement rate can be estimated from physical property changes generally indicate that the simple displacement models overestimate the number of defects.[88] Therefore, the number calculated above is an upper limit and probably should be reduced. However, the calculation does point out the fact that many vacancies and interstitials are created by each reactor neutron interacting with a lattice atom; these defects in turn can enhance solid state transformations which are dependent upon diffusion. Also, clusters of these defects

which are known to form in metals can act as nucleation sites for heterogeneous precipitation of metallic phases in alloys.

The above discussion has concentrated on the number of defects produced by an energetic PKA. An equally important problem is the determination of the spatial distribution and configuration of such defects. In medium- and heavy-mass metals, a PKA created by a fast neutron initially loses energy primarily by inelastic collisions with electrons until it reaches an energy of about A Kev, where A is the atomic mass of the PKA ($\sim$ 64 Kev for Cu atoms). At energies of the order of 10 Kev or greater, the mean free path between PKA collisions with lattice atoms is several interatomic spacings,[97] and thus the damage consists of secondary branches dispersed along the primary's path. As the PKA slows down to about 2 Kev or so, its mean free path approaches one inter-atomic distance and it collides with almost every atom in its path. The resulting damaged region is called a "displacement spike."[96]

2. Displacement Spikes

The energy lost by the PKA near the end of its path length occurs both thermally and by displacements; i.e., through "thermal"[95] and "displacement"[96] spikes. In the thermal spike mechanism, energy is dissipated by electronic collisions and their subsequent lattice interactions. Simple transient heat transfer calculations[89] indicate that although localized temperatures above the melting point occur, the spike's duration is of the order of only 10^{-11} sec so that only limited thermal diffusion of lattice atoms is expected.

The displacement spike as originally envisioned by Brinkman[96] consists at the instant of its creation of a region ($\sim$ 75 Å in diameter) which contains a vacancy-rich central core surrounded by a sheath of displaced interstitials. This configuration has been confirmed in a recent computer study[92] of displacement cascades in BCC and FCC metals. Since such a configuration of defects is highly unstable, many of the interstitials will rapidly relax back to the depleted region, although probably not to their original sites. The resulting effect is the creation of a highly mixed and disordered region of the lattice. All of the displaced atoms, however, do not return to the central depleted region, as many of the interstitials are driven away leaving single vacancies and clusters of varying sizes. The vacancies can then migrate to various sinks in the lattice, form larger vacancy clusters, or collapse to form dislocation loops.

Calculations of such displacement effects are extremely sensitive to the choice of the interatomic interaction potential and the subsequent determination of the mean free path between PKA displacements. Brinkman's[96,98] original calculations based on a simple Thomas-Fermi screened coulomb potential indicated that the mean free path of Cu atoms in a copper lattice is about one interatomic distance for PKA energies of less than 20 Kev. Thus an energy of $\sim$ 20 Kev would be dissipated in the spike's volume (estimated to be about 75 Å). A more recent calculation by Davies and Sims[97] indicated that the mean free path (ℓ_m) of Cu atoms varied approximately as

$$\frac{\ell_m}{T} \simeq 2.16 \text{ Å/Kev}$$

where T is the primary's energy. If it is assumed that a spike occurs when ℓ_m equals the interatomic spacing, the energy dissipated in the spike would be approximately 1.2 Kev, or a factor of $\sim$ 17 less than Brinkman's result. The spread of these two results is indicative of the uncertainties involved in the analytical models.

An improved method of determining the properties of displacement spikes is by computer experiments.[92,99] Computer simulation methods use more realistic interatomic potentials and can account for such lattice effects as channeling and vacancy-interstitial recombination in determining the energy deposition of the primary and secondary knock-on atoms. One such study (Beeler[92]) simulated displacement spike effects in α-iron and copper for a range of PKA energies. The results indicated that (1) the PKA energy is completely transferred to secondary knock-on atoms within a distance of 10-80 Å in the range $0.5 \leq T \leq 25$ Kev, (2) the cascade dimension is determined by the ranges of quasi-channeled (short range) high order knock-on atoms rather than by the range of the initiating PKA, and (3) the initial defect configuration in the spike is similar to what Brinkman suggested.[96]

On the basis of such a model, a precipitation hardening alloy such as Cu-Fe in a reactor environment would experience a number of highly disordered regions (spikes) 10 to 80 Å in diameter having high vacancy densities. The number ΔN_s of such spikes created per unit time would be given by

$$\frac{\Delta N_s}{\Delta t} \simeq N_o \bar{\sigma}_s \phi_f \qquad \text{(II.27)}$$

since one spike is expected for each neutron-PKA interaction. In the spike regions, the high vacancy concentration would result in artificially large solute diffusion coefficients, thereby enhancing precipitation in a super-saturated alloy. Dislocation loops produced in the spike region could serve as nucleation sites for heterogeneous precipitates. On the other hand, small precipitate particles enveloped by such a spike could be dissolved, leading to an overall reduction of the precipitate phase. In addition, an ordered precipitate phase could be effectively disordered by the spike mechanism. The experimental observation of these effects is discussed below.

3. Experimental Observation

Experimental observations of radiation effects on precipitation processes in metallic alloys have been made by measuring electrical resistivity,[5] magnetic[5,50] and mechanical[102] properties and more recently by high voltage electron microscopy.[51] In general, results from such studies have confirmed the predicted effects discussed above, however, not without some ambiguity.

Observation of the first effect discussed at the end of the last section, that of enhanced-diffusion, has been made in many systems including order-disorder alloys and precipitation hardening alloys. The pioneering quantitative studies in this area have been made primarily on Cu-Zn (α-brass) and Cu-Al and to a lesser degree on the Fe-Si precipitation system. These studies, which consist of the measurement of resistivity in originally quenched alloys as a function of annealing temperature and irradiation, have been thoroughly reviewed by Damask.[87] Results from these measurements indicate that a diffusion coefficient

of about 10^{-20} cm^2/sec can be achieved by reactor irradiation alone. Such diffusion enhancement is believed to arise primarily from the motion of excess vacancies.[87] In the case of precipitation hardening alloys, the amount of precipitation caused by such a small diffusion coefficient has only been observed in samples that have been quenched to retain all the solute atoms in super-saturated solid solution.[101,102] Piercy's experiments[50] with Cu-2 wt. % Co alloy samples which exhibit superparamagnetism indicate that the precipitate particles formed as a result of reactor neutron irradiation have radii less than 10 Å.

The second effect mentioned above is that of nucleation of precipitates on vacancy clusters or dislocations caused by displacement spikes. This effect is difficult to determine in precipitation hardening systems since the increased precipitation caused by irradiation in a quenched alloy could be caused by either enhanced diffusion or enhanced nucleation (e.g., see Reference 101 and 102 on the Cu-Be system). Successful demonstration of the effect was performed by Hull and Mogford[103] with a Fe-.004% C alloy. Using an electron microscope these workers observed an increase in the number of carbon precipitates formed during irradiation in the temperature range 60-100°C over those formed during aging in the same temperature range. There have been several other experiments of this type which have demonstrated the enhancement of nucleation by irradiation--for examples, see the review paper by Damask.[87]

The dissolution effect of displacement spikes on precipitates has been experimentally investigated in two systems, Cu-Co[50] and Cu-Fe.[5] In both cases, samples aged at temperatures which would

favor the production of small precipitate particles showed property changes upon irradiation which indicated that precipitate particles were being dissolved.

In the Cu-Co (2.0 wt. % Co) system, Piercy carefully studied the break-up of precipitate particles caused by a fast neutron exposure of $3.4(10)^{19}$ nvt as a function of particle size. Co precipitates of varying sizes were produced by aging quenched samples at 395 and 600°C for varying times. During the early stages of annealing (i.e., for particles of about 150 Å or less), the precipitates exhibit a phenomenon called superparamagnetism.[104]. This phenomenon is characterized by the particles having a single magnetic domain whose direction is independent of its neighbors and is thereby free to rotate. The size of these particles and the standard deviation of the particle size distribution can be determined from the initial and final slopes of the magnetization curve.[105] Also, the number density of the particles can be obtained from the saturation magnetization once the average particle size is known.

Using this method, Piercy determined the average particle size and number density before and following irradiation. From the results, he concluded that (1) only particles with a radius of less than about 12.4 Å were effectively dissolved by neutron induced spikes and that (2) partial overlapping of a spike and precipitate particle did not cause partial dissolution. The calculated spike radius (assuming spherical spike volumes and complete overlapping) to produce these effects was about 34 Å. His second conclusion above is questionable, since according to Table 1 in his paper[50] two samples with initial radii of about 41-47 Å showed an effective decrease in average radius

and accompanying increase in the number of precipitate particles. It would appear that the particles were partially dissolved and new precipitates were formed in the spike region as a result of the high solute concentration existing there. Although there is some uncertainty in Piercy's calculation which predicted an average spike radius of 34 Å, his experimental results clearly demonstrate that spikes do dissolve small precipitate particles and that particles smaller than about 13 Å are unstable in a reactor.

Similar radiation effects to those reported by Piercy[50] for Cu-Co were determined in a Cu-1.7% Fe alloy by Boltax.[5] Since samples of this alloy aged below the eutectoid temperature contain paramagnetic γ-Fe precipitate particles,[3] Boltax was not able to directly determine particle sizes in the manner of Piercy.[50] Instead he relied on precipitation kinetics data from a previous aging experiment (Boltax[3]) and the particle size data obtained from the similar Cu-Co system[50,104] to estimate the average size of the γ-Fe precipitates. (Both the aging and radiation dissolution results were obtained from resistivity measurements.) His size estimate was based on the growth law for spherical particles,[106]

$$r^3 = k'e^{-(Q/RT)}t \ , \qquad \text{(II.28)}$$

where k' was determined from the Cu-Co size data (104) and the activation energy Q was obtained from the Cu-Fe aging results. Since the results of his earlier kinetics studies (see section C of this chapter) indicated precipitation occurred on dislocation loops, the use of Equation (II.28) was not justified. However, as discussed in the previous section, electron microscopy studies of Cu-Fe alloys aged at

550°C have revealed the presence of spherical coherent γ-precipitate particles.[85] Therefore, Equation (II.28) would apply to particle growth in the Cu-Fe system assuming the kinetics were diffusion controlled, which is probably not the case at the lower aging temperatures used in Boltax's work. In addition, a comparison of Mössbauer and resistivity results in aged Cu-0.6% Fe alloy samples (see Chapter IV) indicates that resistivity is not a direct measure of the concentration of Fe in solid solution as was assumed by Boltax.[3,5] The effects of small iron clusters on the resistivity can not be ignored during the early stages of aging.

Because of the foregoing considerations, the quantitative aspects of Boltax's work appear to be incorrect, however, his resistivity measurements of aged and irradiated Cu-Fe samples do provide a qualitative indication of the precipitation processes occurring. In general, Boltax's[5] measurements showed an increase in resistivity upon irradiation for Cu-1.7 wt. % Fe samples previously aged at temperatures in the range 250-475°C. Since an increase in resistivity indicates an increase of Fe in solid solution (or to a lesser extent a reduction in precipitate particle size), dissolution of precipitate particles in these samples did occur. Boltax also found that the resistivity of samples aged at temperatures > 500°C decreased upon reactor irradiation. He interpreted this as an indication that the precipitate particles were too large to be dissolved by a displacement spike and that the existing particles increased in size as a result of radiation induced diffusion.

Unlike the model used by Piercy[50] to calculate the effective displacement spike size, Boltax used a model which accounted for

precipitate dissolution caused by partial spike-particle interactions. His results indicate that precipitate particles less than $\sim$ 50 to 100 Å in radius can be partially dissolved (or broken-up) by displacement spikes whose mean radius was estimated to be 35 Å. Although the size of the spike agrees with Piercy's estimate,[50] the fact that particles with radii greater than 13 Å can be dissolved does not agree with Piercy's conclusion. There are three reasons for this disagreement: (1) Boltax's particle size estimate is in error (see Chapter IV); (2) the spike-particle interaction models used by the two investigators were different and (3) the property changes measured in the two experiments (magnetization and resistivity) differed in their sensitivity to particle size changes. At the onset of the present study, it was anticipated that a direct determination via Mössbauer spectroscopy of Fe concentration in the phases existing in Cu-Fe before and after irradiation would clarify the above results. A comparison of the present study's results to those of Piercy[50] and Boltax[5] is made in Chapter IV.

The final effect of fast neutron irradiation on precipitation hardening alloys to be considered is the conversion of a coherent precipitate to the incoherent form. It is believed that large coherent precipitates having high strain fields associated with them can be converted to the more stable incoherent form as a result of vacancy clusters created in the collision cascade.[107] The extreme case of this effect involved the partial conversion of coherent to incoherent particles in a Cu-2.4% Fe alloy by electron irradiation.[108] In this experiment, Denney[108] observed the conversion of FCC γ-particles to the incoherent BCC α-form by measuring the saturation magnetization of

the alloy samples before and after irradiation. This effect is remarkable since high energy electrons only produce isolated defects. Denney's results have not been successfully explained to date.

A similar experiment except with fast neutron bombardment was performed by Boltax[5] on Cu-Fe alloys with Fe concentrations in the range 0.8-5.0%. Similar to Denney's results, the saturation induction measurements of this investigator also showed the presence of α-Fe following the irradiation of annealed samples originally containing only γ-Fe. However, in samples containing both types of precipitates, the saturation induction measurements gave ambiguous results indicating an increase in α-Fe for some samples and a decrease for others. Mössbauer measurements should be able to provide unambiguous results concerning the γ-α transformation (or its reverse), since the six-line α-iron pattern is easily resolved from the single lines due to γ-iron and Fe in solid solution.

CHAPTER III

EXPERIMENTAL PROCEDURE

A. Sample Preparation

The Cu-0.6at.%Fe absorber foils were prepared by melting a mixture of 99.999% copper shot with pure iron powder enriched to 69.7% in Fe^{57}.* The melting was performed in a vacuum induction furnace** with the sample contained in a vitrious graphite crucible. The Cu-Fe mixture was maintained in the molten condition for approximately one hour at a temperature of about 1250°C. To insure a homogeneous mixture of Fe in copper, the melting procedure was repeated three times.

The ingot so obtained weighed about 20 g. It was subsequently cold-rolled** to strips 13 to 20 μm in thickness from which rectangular foils measuring 0.7x0.5 $in.^2$ were cut. On two occasions during the rolling procedure, the foils were subjected to re-crystallization heat treatments at 850°C to relieve strains induced by cold-rolling. Samples from several of the Cu-Fe foils were chemically analyzed to determine the Fe concentration and its homogeneity.*** The mean composition for

---

*The enriched Fe was obtained from Oak Ridge National Laboratory, Oak Ridge, Tennessee.

**The induction melting and rolling operations were performed with the assistance of L. Terner and L. Whitt at the Ford Scientific Laboratory, Dearborn, Michigan.

***The chemical analyses of the Cu-Fe samples were performed by T. F. Strow of the Ford Scientific Laboratory.

eight samples was 0.63at.% with a standard deviation of .04at.%. A spectrochemical analysis of these samples showed only trace amounts of carbon and other impurities.

The majority of the Cu-0.6at.%Fe foils underwent the same heat treatment procedure. The initial heat treatment consisted of a solution anneal for three hours at 1000°C followed by rapid quenching to room temperature. For this purpose, the foils were encapsulated in Vycor capsules filled with a mixture of argon and hydrogen and then heated in a temperature controlled tube furnace.* The rapid quench was achieved by dropping the capsule with a steel weight follower onto a piece of angle iron submerged in a water bath below the furnace. Bright surfaces were maintained on all specimens prepared in this manner. Most of the samples so treated were subsequently subjected to an aging heat treatment at lower temperatures (285-600°C) using this same technique except that the Vycor capsules were not broken during the quench.

Several of the 0.6% Fe foils cut from an 80 μm-thick rolled strip were first solution annealed and then cold rolled to a thickness of about 25 μm. Five such samples were then aged at 600°C, while the remainder were used to study the effects of cold-rolling on solution annealed alloys. In addition to the 0.6at.% Fe alloy samples, Cu foils containing 0.1, 0.2, 0.3, and 0.4 at.% Fe were also used in this study.** These were prepared by plating 91% Fe^{57}-enriched Fe onto Cu foils and diffusing at 1000°C in an inert atmosphere. All of the samples with lower Fe concentrations were solution annealed at 1000°C.

---

*Lindberg Heavy-Duti tube furnace and control console, Models 54032 and 59344.

**Obtained from R. Knauer of the Sandia Laboratories, Albuquerque, New Mexico.

One of the primary considerations in the preparation of the Cu-Fe absorbers was that of thickness optimization. In this regard, the following criteria were considered:

(1) The absorber thickness is chosen so as to maximize the information obtainable in the Mössbauer experiment; i.e., maximize the ratio of the maximum resonant intensity in counts per channel to the standard deviation of the counts per channel.[37]

(2) The effective absorber thickness T should be less than one to minimize line broadening (maximize resolution) as discussed in Chapter II and Appendix A.

(3) The actual absorber thickness t should be large enough to allow resistivity measurements to be performed (see Section C of this chapter).

The latter two criteria above were considered most important for this work. Preliminary tests using the resistivity measurement apparatus described in Section C of this chapter demonstrated that reproducible resistivity measurements could be performed with foils as thin as $\sim$ 12 μm. Because of significant atomic absorption of the 14.4 Kev gammas in copper, it was desirable to use thin foils to maximize the Mössbauer information. With an Fe enrichment of 69.7%Fe^{57}, foils with thicknesses in the range 12-15 μm satisfied the second criterion ($.77 \lesssim T \lesssim .94$), yet provided sufficient spectral intensity to allow reasonable counting time.

The source used in this study consisted of 50 mCi of Co^{57} dispersed in a Cu matrix.* It was prepared by plating Co^{57} onto a Cu foil and diffusing at 950°C in an Argon atmosphere, followed by quenching to room temperature. With the spectrometer used in this study, the 50 mCi Cu(Co^{57}) source produced a 0.21 mm/sec corrected line width for the inner two lines of a 1/2 mil natural iron absorber.

B. Mössbauer Spectrometer

In studying the Mössbauer effect, the energy scan over the line structure of the resonant gamma-rays is provided via the Doppler shift by varying the relative velocity between the source and absorber. The simultaneous registration of the transmitted gamma-rays versus relative velocity can be accomplished by coupling a multichannel analyzer with a linear velocity drive.[109-112] In this method, the source is mounted on the drive shaft of an electro-mechanical transducer which is constrained to move in a cyclic manner between positive and negative velocity extremes.

The spectra in this experiment were recorded using a multichannel analyzer operating in the time or multiscaling mode in conjunction with a linear velocity drive of the electro-mechanical feedback type.[111] The existing spectrometer is a modified version of an earlier system used in the Department of Nuclear Engineering.** A

---

*The Cu(Co^{57}) source was obtained from the New England Nuclear Corporation, Boston, Massachusetts.

**The original drive system is described in a thesis by J. F. Ullrich.[37] Unlike the present system it derived its basic triangular drive signal from the analog address scaler sweep of the MCA.

block diagram of the spectrometer equipment including the gamma-ray detection system is shown in Figure III-1. A description of the design of the drive system, including schematic diagrams of all new components, is given in Appendix C along with a listing of commercial components used in the spectrometer.

1. Drive System

At the onset of this project it was apparent that 'equipment' broadening of spectra taken with the original ME drive system prevented the attainment of the optimum resolution necessary to separate the complex Cu-Fe structure. The major portion of line broadening was caused by the combination of (a) higher harmonic noise due to finite steps in the analog address scaler reference signal, (b) 60 cycle pick-up from the vacuum tube components in the drive amplifier, and (c) a phase shift in the drive signal following amplification. In general, the original drive amplifier contained mostly vacuum tube components so that overall system performance was inferior to similarly designed systems using solid state components. In particular, frequent tuning and repairs were required of the vacuum tube electronics. Since commercial ME drives were relatively expensive at the time, it was decided that appropriate modification could be made to the original spectrometer by employing a redesigned drive amplifier using the latest solid state components and obtaining the drive's reference signal from an independent function generator. Some of the original spectrometer's major components were retained including the moving-coil drive transducer and the multichannel analyzer-multiscaler system.

In the present ME spectrometer the triangular reference signal is derived from an ultrastable function generator and not the analog

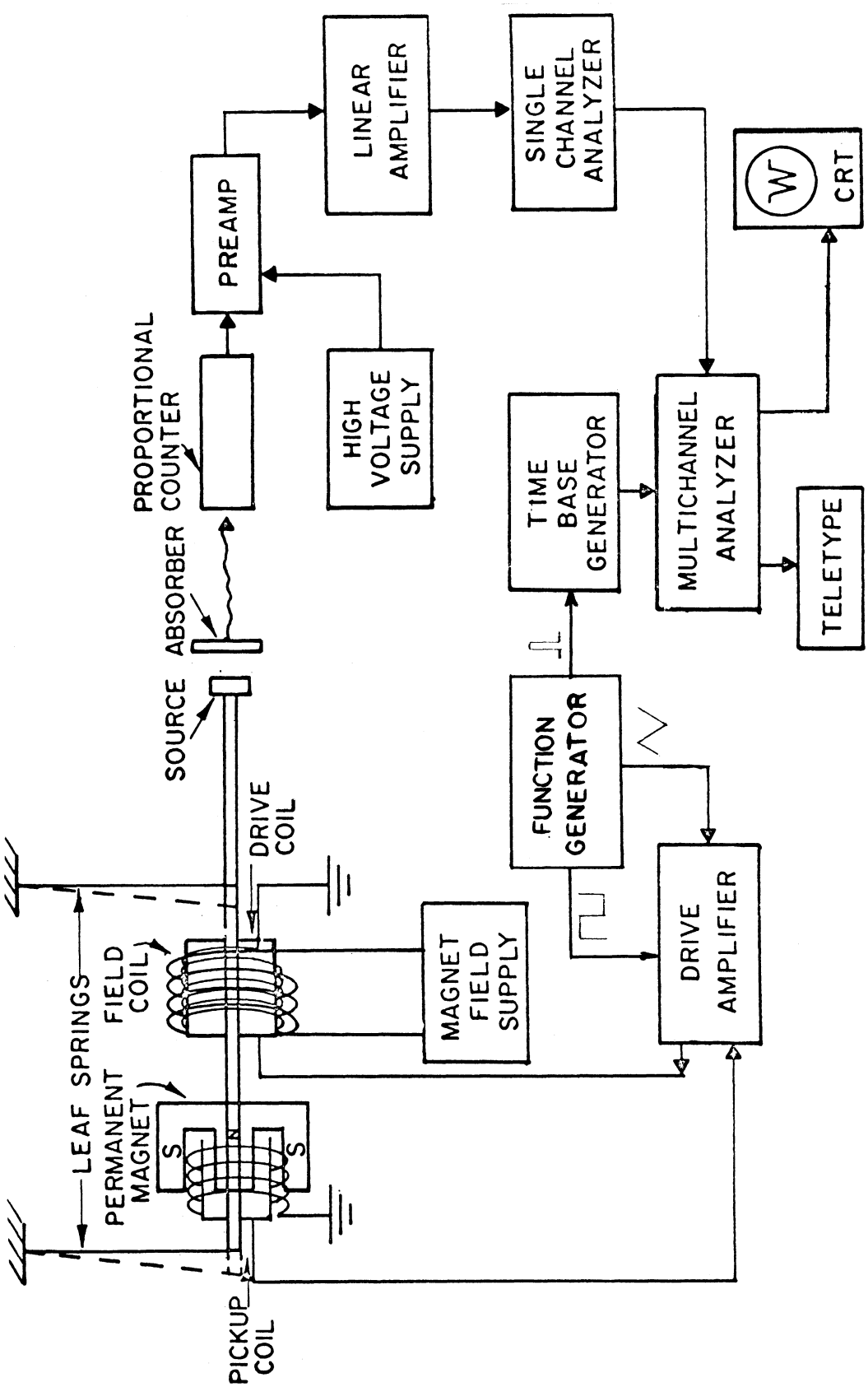

Figure III-1. Experimental System for Mossbauer Effect Measurements

address scaler sweep of the MCA as was the case for the original drive. The function generator is a modification of Cohen's design[113] which produces extremely stable triangular and square waves that are precisely in phase. The version used has a frequency and amplitude stability and linearity of better than 0.1%.

The new drive amplifier performs three basic functions. First, it integrates the triangular reference signal provided by the function generator to produce the principal parabolic displacement wave form. Then it synthesizes the square, triangular and parabolic wave forms to approximate the voltage signal required to give the moving-coil transducer a linear velocity response. Finally, by comparing the output of the transducer's velocity pick-up coil (amplified about 50 times) to the triangular reference signal a correction signal is derived which provides negative feedback to control the motion of the transducer. The combined signals are boosted in the final amplification stage to provide the required driving current for the transducer. Further details of the drive electronics can be obtained from Appendix C.

The analog address scaler or multiscaler (MCS) sweep is synchronized to the source motion by a trigger signal received from the function generator at the beginning of each period. When the last channel has been addressed, the MCS is automatically reset to zero channel to await the arrival of the next trigger signal. By making the product of the MCS dwell time per channel and the number of channels equal to (actually slightly less than) the drive motion's period, the velocity spectrum is recorded twice in the MCA memory, the second half being the mirror image of the first half. The operating frequency of

the transducer was set below its resonance frequency of 17 Hz at approximately 10 cps for the Fe^{57} spectra taken in this study.

Initial calibration of the spectrometer's velocity scale was performed by using the room temperature hyperfine spectrum of Fe^{57} from a 1/2 mil natural iron foil in conjunction with the data given in Stevens.[52] One such spectrum taken with the 50 mCi $Cu(Co^{57})$ source is shown in Figure III-2. Rolling and saturation effects on the intensity of the outer lines can be seen in the figure. A comparison of the line positions and widths with their expected values is made in Table III-1 below. Using the excited and ground state splitting factors of g_1 = 2.2363 mm/sec and g_0 = 3.19156 mm/sec recommended in Stevens,[52] the linearity of the spectrometer over the velocity range of about ± 6.0 mm/sec was determined to be about .01 mm/sec or within 0.1%.

The reference zero position of all spectra taken in this work is given as the centroid of the sodium nitroprusside (SNP) doublet. For this purpose, a National Bureau of Standards' secondary SNP standard absorber[114] was used. (Its spectrum is shown in Figure III-3.) For the majority of the Cu-Fe alloy samples studied, a reduced velocity range was used since their spectra displayed no broad magnetic hyperfine splitting. In these cases calibration of the velocity scale was obtained from the splitting of the SNP doublet. Excellent agreement occurred between the channel calibration values obtained from the SNP splitting ($\Delta\nu$ = 1.7015 mm/sec) and those from the splitting of the inner two iron lines ($\Delta\nu$ = 1.6793 mm/sec).

The overall performance of the modified spectrometer satisfied our initial requirements of low equipment broadening and good velocity

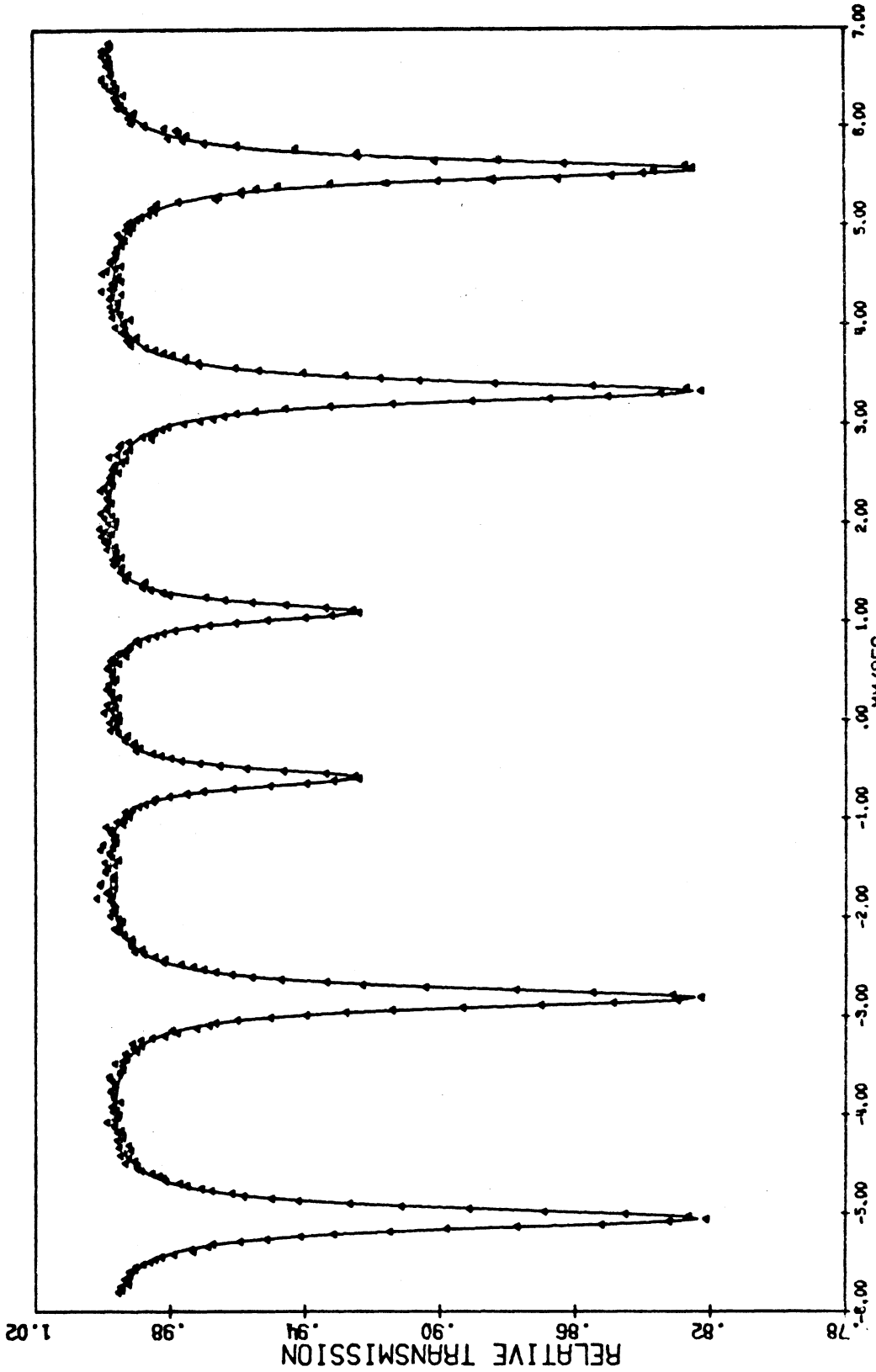

Figure III-2. Resonance absorption spectrum of natural iron standard.

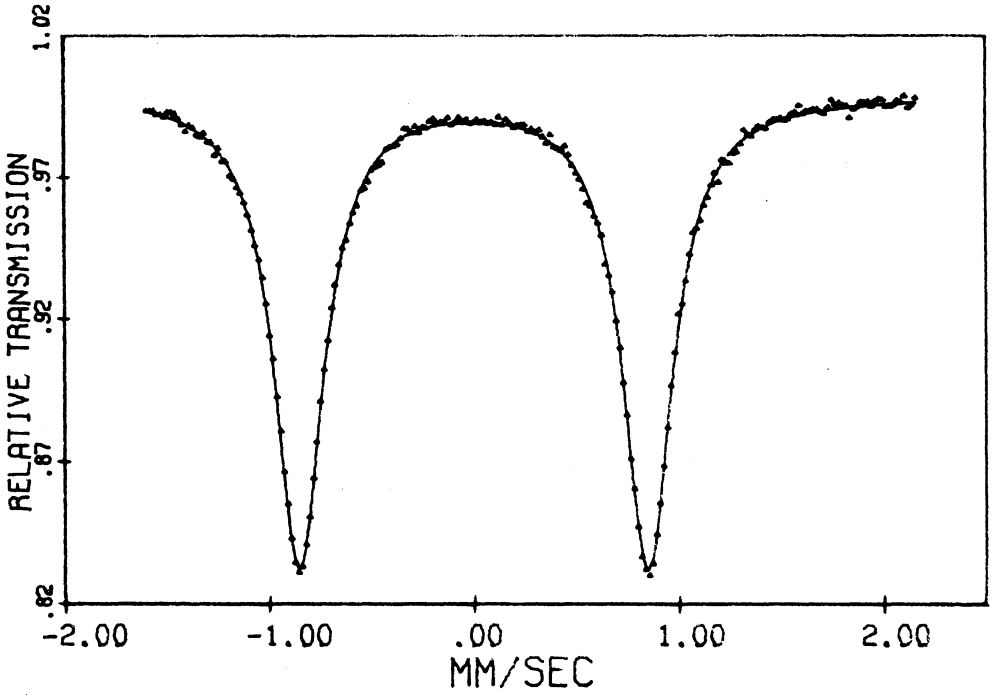

Figure III-3. Resonance absorption spectrum of NBS secondary standard, Sodium Nitroprusside.

stability. Calibrations over a two year period showed variations of only .003 and .015 mm/sec per month in the SNP doublet's splitting and centroid position parameters, respectively. The noise reduction attained over the previous drive system was significant; the observed velocity error signal was reduced from about 0.25 to 0.1% of the maximum velocity. Line broadening* as determined from the inner two lines of the metallic iron spectrum decreased from about 0.04 to 0.015 mm/sec.

TABLE III-1

NATURAL IRON SPECTRUM

Line	Measured Position mm/sec (±.003)[a]	Expected Position mm/sec	Measured Line Width ±.008 mm/sec	Expected Line Width mm/sec
1	-5.054	-5.052	.250	.225
2	-2.814	-2.816	.236	.215
3	-0.580	-0.580	.218	.204
4	+1.100	+1.100	.216	.204
5	+3.334	+3.336	.233	.215
6	+5.573	+5.572	.248	.225

[a] Reference: NBS secondary standard, sodium nitroprusside (SNP). $(IS^{SNP}-IS^{Fe}) = -0.260$ mm/sec.

*Equipment broadening was determined by evaluating the $\Delta\omega$ remaining after thickness corrections to the line-width were made; i.e., the width in excess of that calculated by Equation II.2.

2. Detection System

The method used to detect the 14.4 Kev gamma-ray of Fe^{57} is well established (e.g., see Reference 115). The commercial components which make up the detection system are listed in Appendix C.

A two-inch-diameter krypton-filled, CO_2-quenched gas proportional counter with a 1/2 in. Be "thru-window" was used because of its relatively high efficiency ($\sim$ 85%) for the 14.4 Kev gamma-ray. Radiation from the Cu(Co^{57}) source was pre-filtered with a five mil Al foil to attenuate ($\sim \chi$1/50) the X-ray peak at 6.3 Kev, and thereby reduce the unwanted low energy contribution to the count rate. The source-detector separation was kept at 8 in. or more so that "cosine smearing" effects(116) on the Mössbauer spectrum would be negligible.

The output pulses from the Kr-CO_2 proportional counter were fed through a preamplifier and pulse-shaping linear amplifier into a single-channel analyzer (SCA) with a window setting at the 14.4 Kev peak. The logic pulses from the SCA were fed into the multiscaling input of the MCA and stored in the memory channel corresponding to the velocity of the source. Adjustment of the SCA window setting was easily accomplished by using the coincidence gating circuit of the MCA in the pulse-height mode.

In order to obtain approximations to the absolute spectral areas as required by Equation (II.14), it was necessary to determine the high energy gamma contribution to the pulses passed by the SCA. This was done by using the method suggested by Housley et al.(117) In this method, a filter of brass 5 mils in thickness is used to absorb the 14.4 Kev gammas (passes less than .02%) while allowing all but 4% of the high energy radiation (122 and 136 Kev gammas from the Fe^{57}

decay) to pass. The count rate so obtained for a particular experimental configuration, multiplied by 1.04, is then the desired background count rate which is used to obtain the signal to background ratio. Because the experimental configuration remained constant and the samples were of the same material and approximately the same thickness, this ratio required only periodic checking.

C. Resistivity Measurements

Resistivity measurements of all of the solution annealed and aged samples and several of the irradiated samples* were made to supplement the ME measurements and serve as a comparison with resistivity data reported by Boltax.[3,5] A detailed description of the procedure and apparatus used in the resistivity measurements is given in a report by Yu.[118]

The measurements were made by the well-known potentiometer method in which voltages across an unknown sample and a standard resistor in series are determined by balancing them against a standard voltage. The foil's resistance was obtained from the product of the standard resistance and the unknown to standard voltage ratio, while its resistivity was calculated from

$$\rho = \frac{M}{\ell^2 d} R \qquad \text{(III.1)}$$

In this expression R is the resistance of the foil, M its mass, d its density and ℓ is the distance between the potential terminals. Extreme

*The condition of many of the irradiated foils was too rough to obtain meaningful results from resistivity measurements.

care was taken in cutting the foils into rectangles in order to provide a constant cross sectional area and minimize errors associated with a non-uniform electric field.

Because of the unique shape of the resistivity specimens, a special four-contact sample holder had to be designed and assembled. It is shown in Figure III-4. The foil to be measured was clamped rigidly between extremely flat brass plates to which the current leads were connected. This arrangement provided a uniform electric field across the foil and also avoided having to connect the current leads directly to the fragile sample. The potential across the foil was measured between two vertically adjustable pointed screws which could be slowly brought into contact with the foil.

The resistivity of each foil was determined by averaging the results of six independent measurements taken with different potential contact positions. The precision of the measurements ranged from 0.5 to 2.0%. Systematic errors in the measurements could have resulted from non-uniform foil thickness, deviations from a constant width, and contact resistance in the potential terminals. Because of the excellent agreement achieved between measurements taken with different potential contact positions, such errors are believed to be within 2.0%.

D. Data Analysis

All spectra obtained in this study were analyzed by the use of computerized least squares fitting techniques based on a modified Gauss-Newton iteration procedure.[119] The fitting methods used were adapted from the computer programs of Chrisman and Tumollilo[120] and

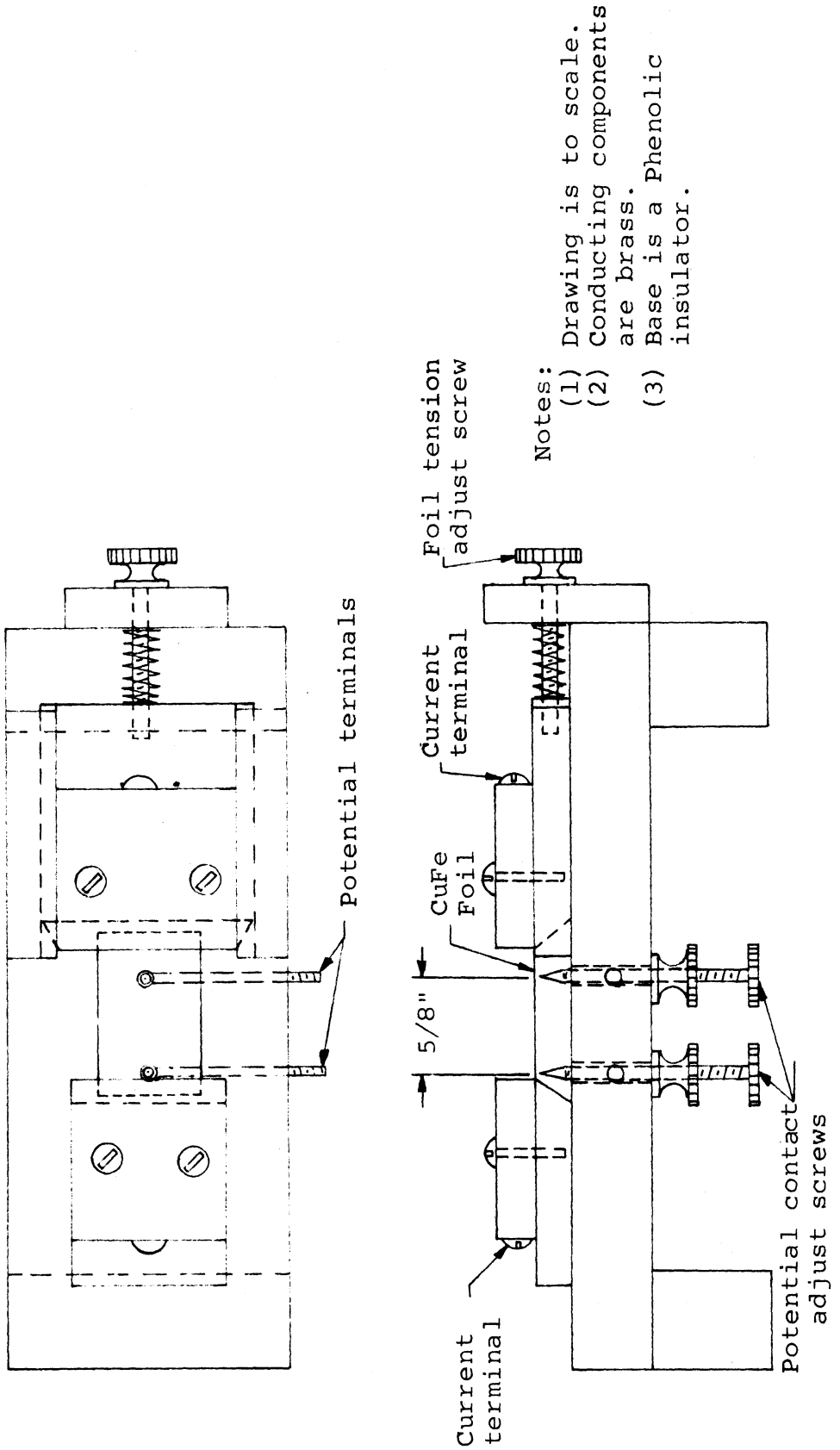

Figure IV-4.--Foil holder for resistivity measurements.

Ullrich.[37]* A short description and Fortran listing of the Mössbauer data analysis code used in this work appear in Appendix D. Descriptions of the iteration techniques used by the program are given in the above references. The data analyses were performed on the IBM Model 360-67 computer at the University of Michigan. Plots of the data and fitted spectra were obtained using a Calcomp automatic plotter.

Basically, two types of distribution functions were used in fitting the experimental data. The first consisted of the usual sum of Lorentzian shaped resonant lines, while the second consisted of a sum of convoluted Gaussian-Lorentzian functions (i.e., Gaussian distributed Lorentzians). In both cases the non-resonant background was fit to a quadratic equation to account for solid angle effects from the moving source.

1. Lorentzian Fitting Functions

As discussed in Chapter II, the transmission of resonant gamma-rays through an absorber with an effective thickness of $T < 5$ is Lorentzian in shape. Thus, the first attempt at fitting the complex hfs spectra observed for the Cu-Fe alloys was to use a simple sum of Lorentzian single and/or pair functions. To avoid having to write a separate "theory" subroutine for each unique resonant line configuration, the following general equation was used to fit the data:

---

*The program originally written by J. F. Ullrich in the MAD (Michigan Algorithmic Decoder) language was subsequently translated into Fortran IV by P. Merrithew.[121] The existing Mössbauer analysis code is a modification of these earlier programs.

$$F(v) = B\left\{1+Cv+Dv^2-\sum_{i=1}^{N_s}\frac{I_i\left(\frac{\Gamma_i}{2}\right)^2}{(v-v_i)^2+\left(\frac{\Gamma_i}{2}\right)^2}\right.$$
$$\left.-\sum_{j=1}^{N_p} I_j\left(\frac{\Gamma_j}{2}\right)^2\left[\frac{1}{\left(v-v_d+\frac{\Delta_j}{2}\right)^2+\left(\frac{\Gamma_j}{2}\right)^2}+\frac{1}{\left(v-v_d-\frac{\Delta_j}{2}\right)^2+\left(\frac{\Gamma_j}{2}\right)^2}\right]\right\}_3 \qquad \text{(III.2)}$$

where the summations are taken over N_s single Lorentzians and N_p symmetric Lorentzian doublets. In the above expression F(v) is the number of gammas transmitted at the velocity v (given in channel units); v_i, Γ_i and I_i are the centroid, linewidth (FWHM) and normalized intensity, respectively, of the ith singlet; Δ_j, Γ_j and I_j are the splitting, linewidth and intensity, respectively, of the jth doublet; v_d is the mutual centroid of the N_p doublets; and B is the number of counts at $v = \infty$ with the coefficients C and D accounting for the linear and quadratic corrections in the non-resonant background. The summation over the mutually centered doublets was a convenient way of fitting the six-line hfs spectra produced by α-iron precipitate particles in the presence of the two singlets produced by γ-iron precipitates and Fe in solid solution with copper. All of the fitting parameters were varied independently.

2. Gaussian-Distributed Lorentzian Functions

In the method of fitting discussed above, line broadening brought about by inhomogeneities in the Fe near-neighbor configurations was accounted for by the unconstrained broadening of the Lorentzian linewidth parameters. In order to treat such broadening in a more realistic manner, the data were also fit to a function of the form

$$F(v) = B+Cv+Dv^2-\sum_{j=1}^{N} d_j(v) \ , \qquad \text{(III.3)}$$

where $d_j(v)$ is a convolution of Gaussian and Lorentzian functions and is given by

$$d_j(v) = A_j\int_{-\infty}^{\infty} dv' \frac{\Gamma/2\pi}{(v-v')^2+(\frac{\Gamma}{2})^2} \cdot \frac{1}{\sqrt{\pi}\theta_j} e^{-(v_j-v')^2/\theta_j^2} \ . \qquad \text{(III.4)}$$

For the above convolution the resonant line fitting parameters become v_j, A_j and θ_j; the centroid, area and Gaussian width,* respectively, of the jth resonant line. The expression of Equation (III.4) represents a Gaussian distribution of Lorentzian functions of width Γ and position v'. The Lorentzian width was fixed in the fitting at 0.21 mm/sec, which corresponds to the minimum experimentally observed linewidth.** The total width (FWHM) of the convolution of Equation (III.4) as a function of the Gaussian width parameter θ is plotted in Figure III-5.

The techniques for least-squares fitting an expression of the form given by Equations (III.3) and (III.4)--in particular, the numerical evaluation of $d_j(v)$ and the obtainment of the partial derivatives required to set up the normal equations--were not found in the Mössbauer literature. For this reason, a description of the

---

*This width parameter is related to the Gaussian "full width at half maximum," W, by $\theta = W/2\sqrt{\ln 2}$.

**Corresponds to the natural iron linewidth (of inner two lines) extrapolated to zero absorber thickness.

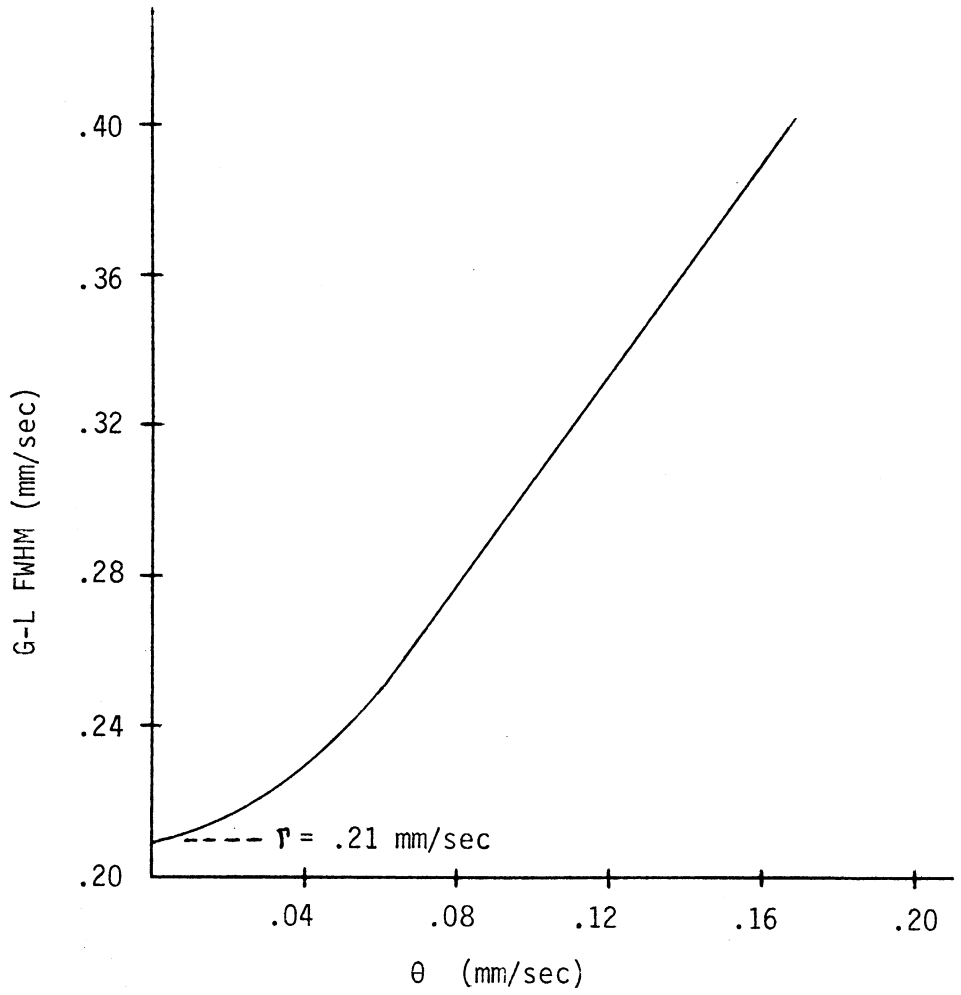

Figure III-5.--Full width at half maximum (FWHM) of Gaussian-Lorentzian convolution (G-L) function versus Gaussian width parameter θ. Lorentzian FWHM Γ fixed at .21 mm/sec.

procedure used to evaluate $d_j(v)$ and its partial derivatives is given in Appendix D (see Section B).

3. Error Analysis

The deviation of the measured spectrum from the fitted spectrum--or, the goodness of fit--is determined by the normalized chi-square value given by

$$\chi^2/N = \sum_{i=1}^{M} \frac{(F_i - Y_i)^2}{\sigma_i^2 (M-N_p)} \qquad \text{(III.5)}$$

In this expression, M is the number of data points; N_p is the number of fitting parameters; F_i and Y_i are the values for the fitted and measured spectrum at the i^{th} data point; and σ_i^2 is the experimental variance in Y_i. Termination of the iteration procedure used in the least-squares analysis program occurs when $\frac{\chi^2}{N}$ reaches a minimum value. (Actually, convergence was assumed to occur when $\frac{\chi^2}{N}$ at iteration k+1 minus $\frac{\chi^2}{N}$ at iteration $k < 10^{-3}$).

After a minimum in $\frac{\chi^2}{N}$ is achieved, the errors in the fitting parameters are determined by the method described by Cohen et al.[122] The statistical error in the k^{th} parameter was calculated from

$$\sigma_k = \left(A_{kk}^{-1} \frac{\chi^2}{N}\right)^{1/2} \qquad \text{(III.6)}$$

where A_{kk}^{-1} is the k^{th} diagonal element of the error matrix. (The error matrix is obtained by inverting the coefficient matrix of the normal equations--see References (37) and (120) for additional detail.)

It was also necessary to determine the errors associated with certain functions of the fitting parameters; e.g., individual resonant

line areas and area ratios. This was accomplished using the error propagation methods described by Ku.[123] The variance in the function f, which depends on K fitting parameters P_k, was calculated from

$$\sigma_f^2 = \sum_{j=1}^{K} \left(\frac{\partial f}{\partial P_j}\right)^2 \sigma_j^2 + 2\sum_{j<k}^{K} \left(\frac{\partial f}{\partial P_j}\right)\left(\frac{\partial f}{\partial P_k}\right)\sigma_{jk} \ , \qquad \text{(III.7)}$$

where σ_{jk} is the covariance of the j and k^{th} parameters. The parameter covariances are obtained from the off-diagonal elements of the error matrix by the expression

$$\sigma_{jk} = (A_{jk}^{-1})\frac{\chi^2}{N} \ .$$

E. Sample Irradiations

Following heat treatment, the Cu-Fe alloy samples were irradiated in the Ford Nuclear Reactor (FNR) at the University of Michigan. The FNR is an open pool research reactor which operates at a power level of 2 MW with an average thermal flux of about $1.5(10)^{13}$ n/cm^2-sec. The core consists of MTR-type, enriched U-235 fuel elements.

All irradiations were made at reactor ambient temperature at two in-core locations. Initial sample irradiations were carried out in the "Central-Stringer" (CS) irradiation facility. The absorber foils were sealed in 1/2" diameter by 1 1/2" Al capsules and then placed in the CS at a vertical position of 5" below the core's mid-plane. To provide heat transfer from the foils, spring inserts were used in the capsules to assure that the Cu-Fe foils made good contact with the capsule walls. Previous thermocouple measurements[37] of in-core Al

sample holders indicated a maximum temperature of about 55°C could be expected. Since temperatures of 120°C or greater for a duration of one month caused no significant annealing effects (as determined by their ME spectra) in quenched and irradiated Cu-Fe samples, no attempt was made to ascertain the exact sample temperatures during irradiation. The fast flux above 0.1 Mev at the irradiation position in the CS was estimated to be $\sim 1.7(10)^{13}$ n/cm^2-sec.

The CS irradiation facility had three shortcomings: (a) samples had to be irradiated for one or more cycles at a time; (b) it was extremely difficult to insert the Cu-Fe foils in the required Al capsules without damaging them; and (c) the fast flux in the CS was significantly lower ($\sim$x1/2) than in the central fuel element. Therefore, subsequent irradiations were performed between fuel plates in the central fuel element (core position L-37). For these irradiations, the Cu-Fe foils were tin plated to prevent corrosion, packaged in Al foil to provide structural stability, and sandwiched between two Al plates having the same curvature as the fuel channels.

An important challenge in any radiation effects experiment involving a reactor is the characterization of the fast flux $\phi(r,E,t)$ and the monitoring of the total integrated fast flux or fluence $\bar{\phi}(r,E)$. An excellent review on this subject has been given by Zijp.[128] Because of the inherent uncertainties involved with interpreting the Cu-Fe Mössbauer data, a careful characterization of the fast flux was not necessary in this work.

For this reason only two flux measurements were made prior to the irradiations: one at the start of a fuel cycle with an In activation monitor (threshold reaction: $^{115}In(n,n')^{115m}In$) and the other

during mid-cycle with an Fe activation monitor (threshold reaction: $^{54}Fe(n,p)^{54}Mn$). Both measurements were made at the core's mid-plane. Using the suggested values of $\langle\sigma\rangle_f^{115} \simeq 168$ mb[128] and $\langle\sigma\rangle_f^{54} \simeq 78$ mb[129] for the effective fission neutron cross sections for the above reactions, the respective fission spectrum fluxes were found to be $\phi_f^{115} \simeq 2.3(10)^{13}$ n/cm^2-sec and $\phi_f^{54} \simeq 2.5(10)^{13}$ n/cm^2-sec. These results are in agreement with the earlier measurements of K. Nishina.[130]

The determination of fast neutron fluences during the irradiations was made with iron wire activation monitors, making use of the $^{54}Fe(n,p)^{54}Mn$ threshold reaction. The results of these measurements are given in Table III-2. The fluence values reported are for an assumed fission neutron energy distribution which approximates the FNR's fast flux[130] and are based on an effective cross section of 78 mb. In calculating the fast fluence from the monitor's activity, a time independent flux was assumed.

TABLE III-2

IRRADIATION SUMMARY

Core Position	Irradiation Time	Fast Fluence	Average Fast Flux
Central Stringer	1 cycle (595.3 hr.)	2.7×10^{19}	1.3×10^{13}
L-37	2 cycles (1177 hr.)	9.0×10^{19}	2.1×10^{13}
L-37	48 hours	4.0×10^{18}	2.3×10^{13}

CHAPTER IV

EXPERIMENTAL RESULTS

A. Preliminary

This research involves the application of Mössbauer (ME) spectroscopy (supplemented by resistivity measurements) to study the effects of thermal aging and fast neutron irradiation on precipitation processes in copper-rich Cu-Fe alloys. A Cu-0.63at.%Fe alloy was selected for use in the aging and irradiation studies, because samples containing Fe concentrations greater than about 1.0% can not be effectively quenched from the solid solution regime of the phase diagram (see Figure II-2). The experimental program consisted of four phases--(a) sample preparation and heat treatment, (b) ME and resistivity measurements of the heat treated samples, (c) irradiation of the heat treated samples in a reactor, and (d) ME and resistivity measurements of the irradiated samples.

Sample preparation details were given in Section III-A. The heat treatment procedures can be summarized as:

(1) All samples were initially solution annealed at 1000°C and quenched.

(2) A majority of the quenched samples were then annealed (aged) isothermally at 285, 335, 400 or 600°C for times in the range from 6 min. to 10,000 min.

(3) A few of the quenched and one of the aged samples were cold worked ($\sim$ 1/5 reduction in thickness). Four of these cold-rolled samples were subsequently given an aging treatment for various times at 600°C.

(4) Four Cu-Fe samples with Fe concentrations of 0.1, 0.2, 0.3 and 0.4% were solution annealed at 1000°C and quenched.

For convenience, the heat treated samples will be referred to below as being either quenched, aged, cold-rolled, or cold-rolled and aged. The Cu-0.6%Fe samples so prepared were investigated by Mössbauer spectroscopy and resistivity measurements. The results are given in Section B and discussed in Section C of this chapter.

The ultimate objective of the above procedure was to prepare Cu-0.6%Fe alloy samples with a variety of relative concentrations of iron in solid solution, γ-Fe precipitate and α-Fe precipitate for the irradiation phase of the experimental program. The precipitates so produced should have different average particle sizes, and hence would behave differently in a fast neutron radiation environment. Our goal was to study the competitive radiation effects of enhanced precipitation, dissolution of precipitate particles and γ-Fe to α-Fe precipitate transformation through the changes produced in the Mössbauer spectral components associated with the phases of iron in copper.

The irradiations were performed in the FNR reactor at three different fast neutron exposures. (For this purpose, three samples per heat treatment were prepared.) Details of the irradiation phase of the program were given in Section III-E. The results of the post-irradiation measurements are given in Section D and discussed in Section E of this chapter.

The room temperature Mössbauer spectra for copper-rich Cu-Fe alloys are complex. Typical spectra which are representative of quenched and various aged samples are shown in Figure IV-1. The data in the figure were computer-fit to a sum of Lorentzian functions using the techniques described in Section III-D and Appendix D. For the purpose of discussion, the following notation introduced by Bennett and Swartzendruber[7] will be used to describe the ME spectra of the Cu-Fe alloy samples of this study (refer to Figure IV-1):

(1) Component γ_0, the central peak in the figure, is produced by iron atoms which are isolated (non-interacting) in the Cu-lattice; i.e., Fe in solid solution with copper. It has an isomer shift with respect to SNP of about 0.484 mm/sec.[7,8]

(2) Component γ_2 is the partially resolved doublet shown in the top spectrum of a quenched (and cold-rolled) sample. It has a splitting of about 0.58 mm/sec.[7,8] During the early stages of aging at intermediate temperatures (500°C or less), the γ_2 doublet decreases in splitting and shifts towards lower velocities making its resolution extremely difficult. In spectrum (b) of Figure IV-1, the γ_2 component was fit to a symmetrically constrained Lorentzian doublet. Although this representation is proven to be incorrect (see Section B below), it is shown here to illustrate the doublet's behavior upon aging. As discussed in Section II-B and Appendix B, the γ_2 doublet is produced by small Fe clusters or possibly surface atoms of large clusters in the Cu-lattice.

(3) Component γ_1, shown in spectra (b) and (c) of the figure, is essentially coincident with the lower energy (left) line of the γ_2 doublet (i.e., with γ_2^L). It is produced by Fe in iron-rich FCC precipitate particles (traditional γ-iron). In the spectrum (c) for a sample aged at 600°C for 200 minutes, γ_1 is the major component and represents about 60% of the iron in copper. In the intermediate case, spectrum (b), the fraction of iron in the γ_1 phase, if any, is uncertain because of the difficulty in fitting individual and doublet components (Lorentzian in Figure IV-1) to the poorly resolved spectra. The problems in interpreting the spectra during the early stages of aging are discussed in Sections B and C of this chapter.

(4) The α-Fe structure, not shown in the present figure, consists of a six-line pattern similar to that in pure iron metal (see Figure IV-7). It represents Fe in the stable BCC precipitate phase.

The room temperature Mössbauer spectra of this study taken of either heat treated or irradiated Cu-0.6%Fe samples display a combination of the above components. The fitting of these complex spectra is discussed in the following section (as well as in Section III-D and Appendix D), while a discussion and possible interpretation of the results is given in Section C of this chapter.

B. Results of Annealing Experiments

1. Solution Annealed and Quenched Samples

All of the samples (a total of 60) were initially given this heat treatment to retain as much Fe in solid solution as possible prior

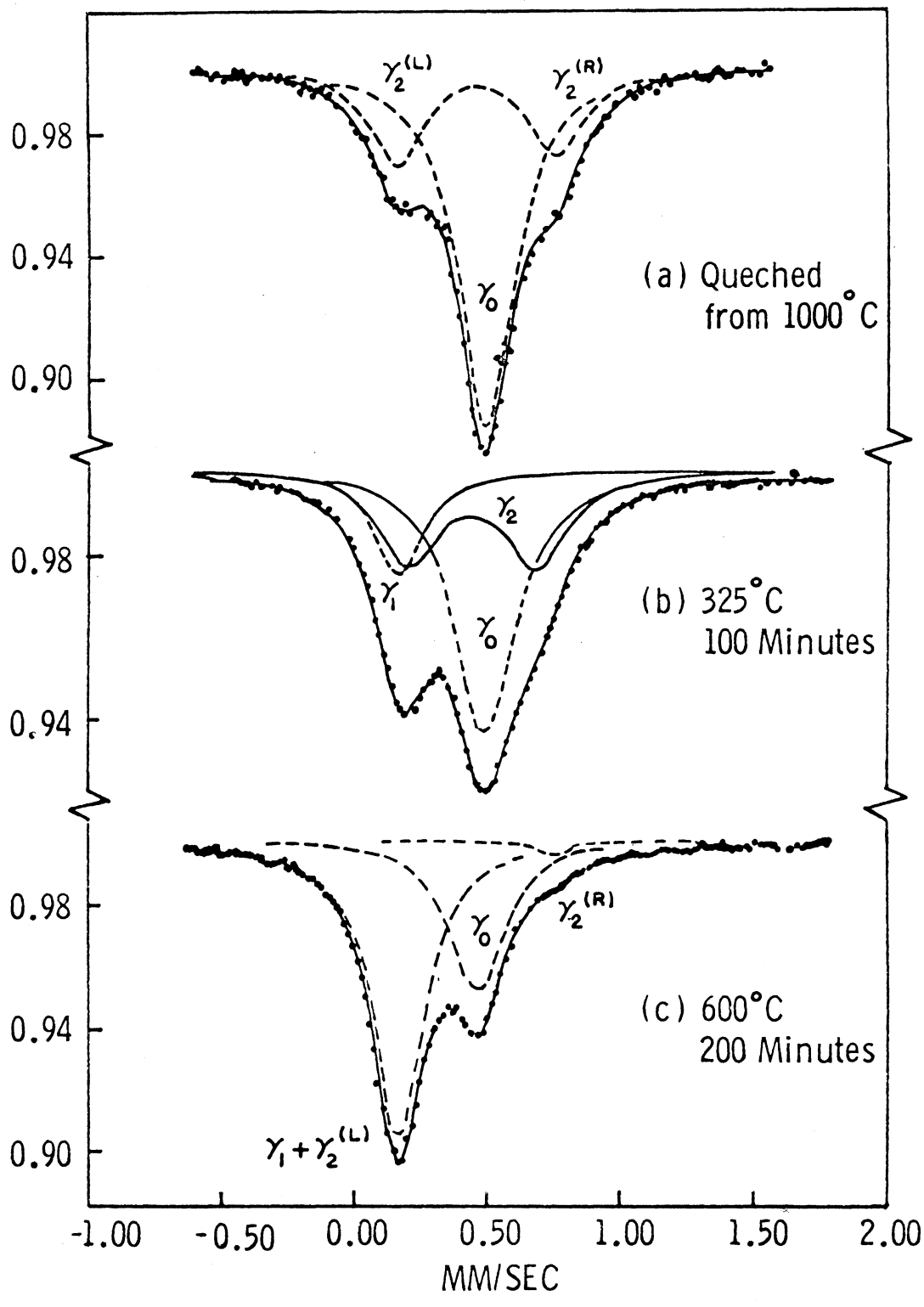

Figure IV-1.--Mössbauer absorption spectra of Cu-0.6%Fe alloy samples representing the quenched and two aging stages of γ-iron in copper.

to subsequent aging and/or irradiation studies. To determine the quality of the quench, resistivity measurements were made for a majority of the solution annealed samples. Mössbauer spectra were also taken of many of the samples for the purposes of correlating with the resistivity results and providing reference spectra for subsequent aging (precipitation kinetics) and irradiation studies. The resistivity values for the quenched samples ranged from $\sim$ 5.8 to 6.5 $\mu\Omega$-cm, depending on the quality or rapidity of the quench. Since an increase in the amount of Fe in solid solution causes an increase in resistivity, the higher ρ values correspond to the best quenches.

As demonstrated by earlier studies,[7,8] the Mössbauer spectra for the quenched samples consisted of a slightly asymmetric γ_2 doublet at the base of a large γ_0 singlet. This is illustrated in Figures IV-1(a) and IV-2. The average values for the fitting parameters of some 15 quenched samples fit to the sum of Lorentzians are as follows:

P_o	P_2	Δ_2	Γ_2^L	Γ_o	Γ_2^R	A_o	A_2
.484(2)	.452(5)	.587(3)	.232(4)	.242(6)	.25(1)	.63(1)	.37(1)

Here, P represents the components' isomer shift with respect to sodium nitroprusside (SNP), Δ_2 the splitting between the γ_2 lines, Γ the linewidth (FWHM), and A the area fraction. The subscript "2" refers to the γ_2 doublet, while "o" refers to Fe in solid solution or γ_0. The above results agree with previously published values.[7,8]

A few of the quenched spectra were also fit to a sum of Gaussian-distributed Lorentzians (see Section III-D). These convolution functions were introduced to simulate the broadening in the spectral

components caused by the different Fe near neighbor configurations associated with both isolated and clustered Fe atoms. (In the case of Fe in solid solution, neighbors further than the nearest shell of 12 atoms might broaden the γ_0 line through distant quadrupole interactions.) The fitting parameters for both types of fitting schemes are summarized in Table IV-1 for 0.2%Fe, 0.6%Fe and cold-rolled 0.6%Fe samples. The Lorentzian fits consisted of an unconstrained sum of three lines, while the Gaussian-distributed Lorentzian (G-L) fits consisted of the sum of a single line plus an area constrained doublet (i.e., the lines of the doublet are constrained to have equal areas). The χ^2/N values, which are good in both cases,* are lower for the G-L fits to the data except for the .2%Fe sample. This is reasonable since one would expect configurational broadening of the resonance lines to be Gaussian rather than Lorentzian in nature. For the 0.2% Fe sample, the lower χ^2/N value for the Lorentzian fit reflects the fact that very little broadening in γ_0 has occurred and also that there were no constraints in the Lorentzian fitting model.

Although it has been discussed briefly in Section III-D, a further remark concerning the Gaussian width or broadening parameter θ is in order. For a pure Mössbauer absorption line, the broadening parameter θ should approach zero (equipment broadening was accounted for by setting Γ = .21 mm/sec). This condition is almost satisfied

---

*For the number of degrees of freedom N of about 200 used in this work, values of $.95 \lesssim X^2/N \lesssim 1.05$ would fall within the $\pm 2\sigma$ limits of the X^2 distribution.[131] Thus, "good fits" would be those yielding a X^2/N value of about unity.

TABLE IV-1

MÖSSBAUER SPECTRA PARAMETERS FOR SOLUTION ANNEALED AND QUENCHED Cu-Fe ALLOY SAMPLES

Sample[c]	Position[a] (mm/sec.)		γ_2 Splitting (mm/sec.)	Line Width[b] (mm/sec.)			Relative Area		χ^2/N
	γ_0	γ_2		γ_2^L	γ_0	γ_2^R	γ_0	γ_2	
(1) Lorentzian fits									
0.2% Fe Q	.482(4)	.449(4)	.585(1)	.233(3)	.227(1)	.255(4)	.708(8)	.292(8)	0.97
0.6% Fe QR	.481(4)	.449(4)	.586(1)	.234(3)	.265(1)	.249(4)	.718(9)	.282(9)	1.03
0.6% Fe Q	.484(4)	.447(4)	.575(2)	.242(4)	.246(2)	.273(5)	.600(8)	.400(9)	1.12
(2) Gaussian-distributed Lorentzian fits									
0.2% Fe Q	.483(4)	.451(4)	.574(1)	.066(2)	.038(2)	.085(3)	.683(4)	.317(6)	1.04
0.6% Fe QR	.482(4)	.451(4)	.580(1)	.077(2)	.061(2)	.073(2)	.667(4)	.333(5)	0.97
0.6% Fe Q	.483(4)	.448(4)	.559(2)	.065(2)	.045(2)	.096(3)	.575(4)	.425(5)	1.07

[a] Position or isomer shift parameter referred to NBS secondary, sodium nitroprusside.

[b] Lorentzian fit: FWHM Γ; Gaussian-distributed Lorentzian fit: width of Gaussian broadening θ.

[c] Key: Q = quenched; QR = quenched and cold rolled.

for the γ_0 line of the 0.2%Fe sample (see Table IV-1), as might be expected of lower concentration alloys. The total width (FWHM) of a given resonant line can be determined from Figure III-5; e.g., for the γ_0 line of the .2% sample for which θ = .038 mm/sec, the FWHM value is 0.229 mm/sec. This compares to a Lorentzian width of Γ = .227 mm/sec obtained for the same 0.2% sample (see Table IV-1).

Comparison of the area fractions obtained from the two fitting models indicates that the γ_0 area fractions (and thus the predicted Fe concentration in solid solution) are consistently smaller for the G-L fits. This is a consequence of the G-L convolution function having less area in its "tails" than a Lorentzian of equivalent FWHM.

Figure IV-2 displays typical spectra obtained for 0.6%Fe samples in the quenched and cold-rolled conditions; the fitting parameters of typical samples are given in Table IV-1. The increase in γ_2's splitting and its decrease in area fraction upon cold-working indicates that some of the small Fe clusters which existed in the quenched alloy are broken-up upon cold-rolling. This is consistent with Window's[8,10] observations made from both room temperature and 4.2°K spectra of a Cu-1.0%Fe alloy. Another effect of cold-working is the broadening of the γ_0 absorption line (about 8% of the total width for the several quenched and rolled samples measured). In a recent experiment, V. A. Lagunov et al.[132] observed similar line broadening of Fe^{57} in deformed copper (source experiment). They ascribed this broadening to quadrupole splitting produced by the localization of the Fe^{57} atoms near defects created during the cold-rolling.

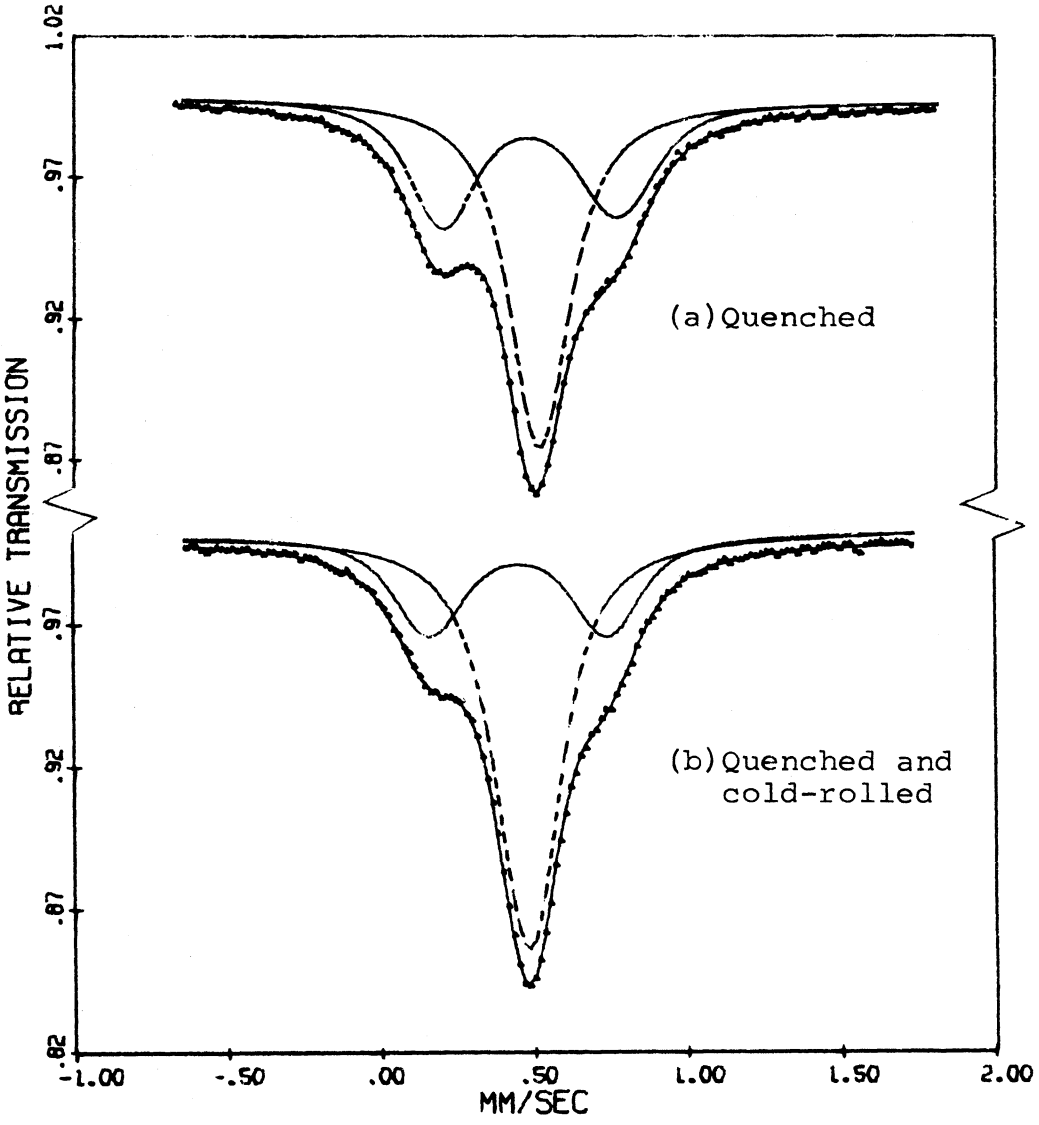

Figure IV-2.--Mössbauer absorption spectra of two Cu-0.6%Fe alloy samples which have been (a) solution annealed and quenched and (b) cold-rolled after quenching. The spectra were fit to the sum of a Gaussian-distributed Lorentzian singlet and area constrained doublet.

2. Aged Samples

The results of the aging studies using Mössbauer spectroscopy are summarized in Tables IV-2 through IV-7* and Figures IV-3 through IV-7. Aging (γ-iron formation) in the Cu-0.6%Fe alloy may be divided into the following three stages according to the appearance of the Mössbauer spectra: (a) incipient Fe clustering characterized by an apparent three-line Mössbauer pattern (class I spectra); (b) an intermediate stage characterized by a broadened, apparent two-line spectrum (class II spectra); and (c) the definite formation of γ-iron characterized by the dominance of the γ_1 line at about .175 mm/sec** and the reappearance of the high energy γ_2^R satellite line (class III spectra). The first two classes of spectra occurred for samples annealed at 285, 335, and 400°C, while the class III spectra were observed only for the samples annealed at 600°C. Examples of the spectra associated with γ-iron aging are illustrated in Figures IV-3 and IV-4 (class I), Figure IV-5(b-d) (class II), and Figure IV-1(c) (class III). The following is a brief discussion of the functions used to fit the three classes of spectra.

---

*The errors or standard deviations for the parameters are given in parentheses following the parameter values. The error in line position is a combination of the error in the determination of the SNP reference "zero" position and the statistical error obtained from the fitting program (see Equation III.6). The other error values were determined in the manner described in Section III-D.3.

**By the comparison of Mössbauer spectra of well-aged Cu-Fe alloys with the results of other measurement techniques, the resonant line at about .17 mm/sec (with respect to SNP) has been identified as being produced by FCC γ-iron.[6,7]

The initial attempt at fitting the Mössbauer data from the aged samples was the application of an unconstrained sum of single Lorentzians. The parameters obtained from this fitting model are listed in Table IV-2 for the 285-400°C aging data. The spectral components have been characterized in the notation of Section IV-A. They are similar in appearance to those illustrated in Figure IV-3 for the Gaussian-distributed Lorentzian fits (see below). As a first approximation, it is tempting, as the notation suggests, to subtract the area of the γ_2^R satellite line from that of the $(\gamma_1+\gamma_2^L)$ line and designate the remaining area fraction as representing the concentration of Fe in γ-precipitates. The variation of the splitting, position and relative area of the γ_2 doublet, represented by the γ_2^R component and a hidden component under the $(\gamma_1+\gamma_2^L)$ or left satellite line, would be associated with the growth of small Fe clusters.

The merit of this simplified model is determined through the χ^2/N values which are consistently much too large. Since the γ_2 doublet can be expected to decrease in splitting and shift in position (see Section II-B and Appendix B) and since the possible growth of a component representing γ-iron precipitates is masked by γ_2^L, the critical parameters in the fitting are the position and area fraction* of the central (γ_0) peak. Since the γ_0 line represents isolated Fe atoms, its position, if properly fit, should remain constant to within

---

*Actually, the normalized peak height was used as the intensity parameter in the Lorentzian fits. The area fraction was obtained from $A_i^* = 1/2(\pi\Gamma_i I_i/A)$, where I_i is the line intensity, Γ_i the line width and A the total area of the spectrum.

TABLE IV-2

MÖSSBAUER SPECTRA PARAMETERS FOR HEAT TREATED Cu-0.6%Fe ALLOY SAMPLES ANALYZED AS THE SUM OF INDIVIDUAL LORENTZIAN LINES[a]

Heat Treatment	Line Position[b] (mm/s)			Line Width Γ (mm/s)			Relative Area			Goodness of fit χ^2/N
	$\gamma_2^L+\gamma_1$	γ_0	γ_2^R	$\gamma_2^L+\gamma_1$	γ_0	γ_2^R	$\gamma_2^L+\gamma_1$	γ_0	γ_2^R	
Average of Quenched Samples from 1000°C	.158(4)	.484(4)	.746(6)	.232(4)	.242(6)	.250(9)	.18(1)	.65(1)	.17(1)	1.0-1.2
285°C, 100 min	.170(4)	.488(4)	.712(5)	.243(3)	.262(3)	.288(5)	.292(4)	.470(9)	.247(9)	1.77
285°C, 1000 min	.175(4)	.489(4)	.696(5)	.246(3)	.261(4)	.298(6)	.310(4)	.42(1)	.27(1)	1.89
285°C, 5000 min	.187(4)	.500(6)	.668(6)	.255(2)	.285(6)	.303(8)	.362(9)	.44(2)	.20(2)	1.41
335°C, 10 min	.169(4)	.487(4)	.718(4)	.241(3)	.246(3)	.286(6)	.277(8)	.490(9)	.233(9)	1.37
335°C, 100 min	.186(4)	.496(4)	.684(6)	.256(3)	.279(5)	.294(7)	.327(7)	.50(2)	.17(1)	1.43
335°C, 200 min	.193(4)	.497(4)	.669(7)	.273(3)	.280(5)	.31(1)	.37(1)	.47(2)	.16(2)	1.23
335°C, 1000 min	.197(4)	.500(5)	.655(8)	.291(3)	.288(7)	.31(2)	.41(1)	.50(3)	.09(2)	2.15
400°C, 6 min	.178(4)	.489(4)	.709(5)	.258(3)	.270(4)	.280(8)	.321(6)	.50(1)	.18(1)	1.29
400°C, 10 min	.185(4)	.493(4)	.694(6)	.262(3)	.273(4)	.29(1)	.332(7)	.51(2)	.16(1)	1.23
400°C, 20 min	.182(4)	.489(4)	.684(8)	.270(5)	.276(6)	.31(2)	.36(1)	.50(3)	.14(2)	1.26
400°C, 100 min[c]	.176(4)	.461(4)		.273(3)	.321(3)		.44(1)	.56(1)		3.24
400°C, 1000 min[c]	.170(4)	.434(4)		.260(3)	.318(2)		.56(1)	.44(1)		3.63

[a] Average of the two mirror image spectra from a single measurement.

[b] Line positions or isomer shift values are referred to the NBS secondary standard, sodium nitroprusside. (SNP).

[c] Only two lines were able to be fit.

experimental error ($\sim \pm .005$ mm/sec) at .484 mm/sec. Observation of Table IV-2 indicates that the apparent γ_0 position has shifted to higher velocities in the initial stage of aging and to lower velocities in the intermediate aging stage. In addition, if Fe clusters or γ-precipitate particles are being formed, there should initially be a monotonic decrease in the concentration of the γ_0 phase as a function of time at a given aging temperature; i.e., a decrease in the area fraction of the γ_0 resonant line. This expectation is also not fulfilled by the single Lorentzian fitting model.

The next attempt at fitting class I spectra characteristic of early aging was the use of two single Lorentzians representing γ_0 and γ_1 and a symmetric Lorentzian doublet representing γ_2 (e.g., see Figure IV-1b). The results of this model are summarized in Table IV-3. This approach also failed for the same reasons given above for the three-line Lorentzian model. An attempt at fitting the γ_2 doublet "phase" to an asymmetric, area constrained Lorentzian doublet also did not significantly improve upon χ^2/N or the critical parameter values.

There are two major reasons why the simple Lorentzian fitting models failed to provide adequate fits of the initial and intermediate aging spectra. One is of course poor resolution. The other is the broadening of spectral components resulting from local variations in solvent and solute atoms about the resonance atom. While the first problem will plague any fitting model, the second can be more effectively treated.

In an attempt to treat the line broadening caused by such configurational variations in a more realistic manner, the spectra were fit to the sum of Gaussian-distributed Lorentzians (G-L) given by

TABLE IV-3

MÖSSBAUER SPECTRA PARAMETERS FOR AGED Cu-0.6%Fe ALLOY SAMPLES ANALYZED AS THE SUM OF TWO INDIVIDUAL LORENTZIANS AND ONE SYMMETRIC LORENTZIAN DOUBLET

Heat Treatment	Position[a] (mm/sec.)			(b) γ_2 Splitting (mm/sec.)	Line Width Γ (mm/sec.)			Relative Area			χ^2/N
	γ_1	γ_o	γ_2[b]		γ_1	γ_o	γ_2	γ_1	γ_o	γ_2	
285°C 100 min.	.165(5)	.498(4)	.456(4)	.532(5)	.192(7)	.265(4)	.279(5)	.067(5)	.47(1)	.46(2)	1.71
285°C 1000 min.	.158(5)	.494(4)	.447(4)	.519(5)	.201(5)	.258(4)	.285(5)	.074(5)	.43(1)	.50(2)	2.09
285°C 5000 min.	.166(5)	.495(4)	.436(5)	.459(9)	.231(6)	.280(8)	.287(9)	.019(1)	.43(3)	.38(3)	1.40
335°C 10 min.	.173(7)	.495(4)	.451(4)	.554(8)	.20(1)	.244(4)	.276(5)	.061(4)	.49(1)	.42(2)	1.36
335°C 100 min.	.164(4)	.501(4)	.447(5)	.474(7)	.229(5)	.287(6)	.271(9)	.173(9)	.50(2)	.32(3)	1.35
400°C 10 min.	.163(4)	.496(4)	.459(5)	.470(8)	.231(5)	.258(5)	.285(8)	.185(7)	.51(2)	.30(3)	1.27

[a] Isomer shift reference: sodium nitroprusside.

[b] γ_2's isomer shift is reported as centroid of the doublet.

Equations (III.3) and (III.4). The results of the fits for class I spectra are given in Table IV-4. The data and fitted curves for three of the samples aged at 335°C are plotted in Figure IV-3.

Comparison of Table IV-4 with the two previous tables reveals that a significant improvement in the quality of the fits, as represented by the χ^2/N values, has occurred with use of the G-L fitting model. In addition, the critical parameters--γ_0's position and area fraction--behave as suggested above. The position of γ_0 remains within $\pm\sigma$ of its value for quenched samples, while the relative area of γ_0 (i.e., the relative Fe concentration in solid solution) decreases in time upon isothermal aging. Because of the poor resolution (see Figure IV-3c) in the case of the sample annealed at 335°C for 1000 minutes, the position of γ_0 was constrained at .484 mm/sec--its average value obtained from the quenched results. For the other samples, all of the parameters were allowed to vary freely during the fit.

Very recently Window[10] reported on an extensive Mössbauer study of aging processes in a Cu-1.0at.%Fe alloy. In this study he suggests that aging in the 300-400°C temperature range produces very small Fe clusters (12 atoms or less). If it is assumed that the Fe atoms cluster in a spherical array--for example, say 12 atoms in the nearest neighbor shell about a central atom--then on the average the Fe atoms would see only 5 iron nearest neighbors. Thus, according to the discussion in Section II-B and Appendix B one would expect a broadened, asymmetric γ_2 doublet (there would of course be a variety of cluster sizes, and thus Fe configurations) and a central singlet (γ_0) due to isolated Fe atoms to make up the Mössbauer spectra of Cu-Fe alloys aged at 300-400°C. For such a model, there would be very little or no

TABLE IV-4

MÖSSBAUER SPECTRA PARAMETERS FOR HEAT TREATED Cu-0.6%Fe ALLOY SAMPLES ANALYZED AS THE SUM OF GAUSSIAN-DISTRIBUTED LORENTZIANS

Heat Treatment	Position[a] (mm/sec.)			Gaussian Width θ[b] (mm/sec.)			Relative Area			χ^2/N
	$\gamma_2^L+\gamma_1$	γ_0	γ_2^R	$\gamma_2^L+\gamma_1$	γ_0	γ_2^R	$\gamma_2^L+\gamma_1$	γ_0	γ_2^R	
Sol. anneal & quench	.158(4)	.484(4)	.739(5)	.065(2)	.042(2)	.089(4)	.189(4)	.633(4)	.178(6)	1.06
285°C 100 min.	.178(4)	.485(4)	.703(6)	.066(2)	.053(2)	.112(4)	.310(1)	.421(3)	.269(7)	1.32
285°C 1000 min.	.176(4)	.481(5)	.687(6)	.064(2)	.046(3)	.121(5)	.325(1)	.370(5)	.304(9)	1.38
285°C 5000 min.	.187(4)	.487(6)	.63 (1)	.069(3)	.065(10)	.14(1)	.373(3)	.30(2)	.33(1)	1.09
335°C 10 min.	.171(4)	.485(4)	.712(6)	.061(2)	.041(3)	.102(5)	.283(2)	.470(3)	.248(6)	1.06
335°C 100 min.	.191(5)	.487(5)	.661(9)	.078(2)	.061(4)	.12(1)	.356(2)	.39(1)	.26(2)	1.08
335°C 200 min.	.194(5)	.486(6)	.65(1)	.084(3)	.058(4)	.13(1)	.378(3)	.35(2)	.27(4)	1.14
335°C 1000 min.	.202(5)	.484[c]	.58(3)	.106(3)	.05(1)	.14(2)	.439(6)	.31(8)	.25(7)	1.34
400°C 6 min.	.182(4)	.485(4)	.691(6)	.070(2)	.056(3)	.115(5)	.342(3)	.441(5)	.220(9)	1.18

TABLE IV-4--Continued

Heat Treatment	Position[a] (mm/sec.)			Gaussian Width θ[b] (mm/sec.)			Relative Area			χ^2/N
	$\gamma_2^L+\gamma_1$	γ_0	γ_2^R	$\gamma_2^L+\gamma_1$	γ_0	γ_2^R	$\gamma_2^L+\gamma_1$	γ_0	γ_2^R	
400°C 10 min.	.189(4)	.487(5)	.67(1)	.082(2)	.049(4)	.13(1)	.341(2)	.42(1)	.24(2)	0.98
400°C 20 min.	.203(5)	.484[c]	.61(2)	.098(3)	.053(8)	.14(2)	.421(7)	.36(5)	.22(7)	1.17

[a]Position parameters are referred to the NBS secondary standard, sodium nitroprusside.

[b]The actual halfwidth (FWHM) of the resonance line can be obtained from the Gaussian width θ by use of Figure III-5.

[c]Positions were constrained at 0.484 mm/sec, the isomer shift for solid solution Fe in copper, during the fitting.

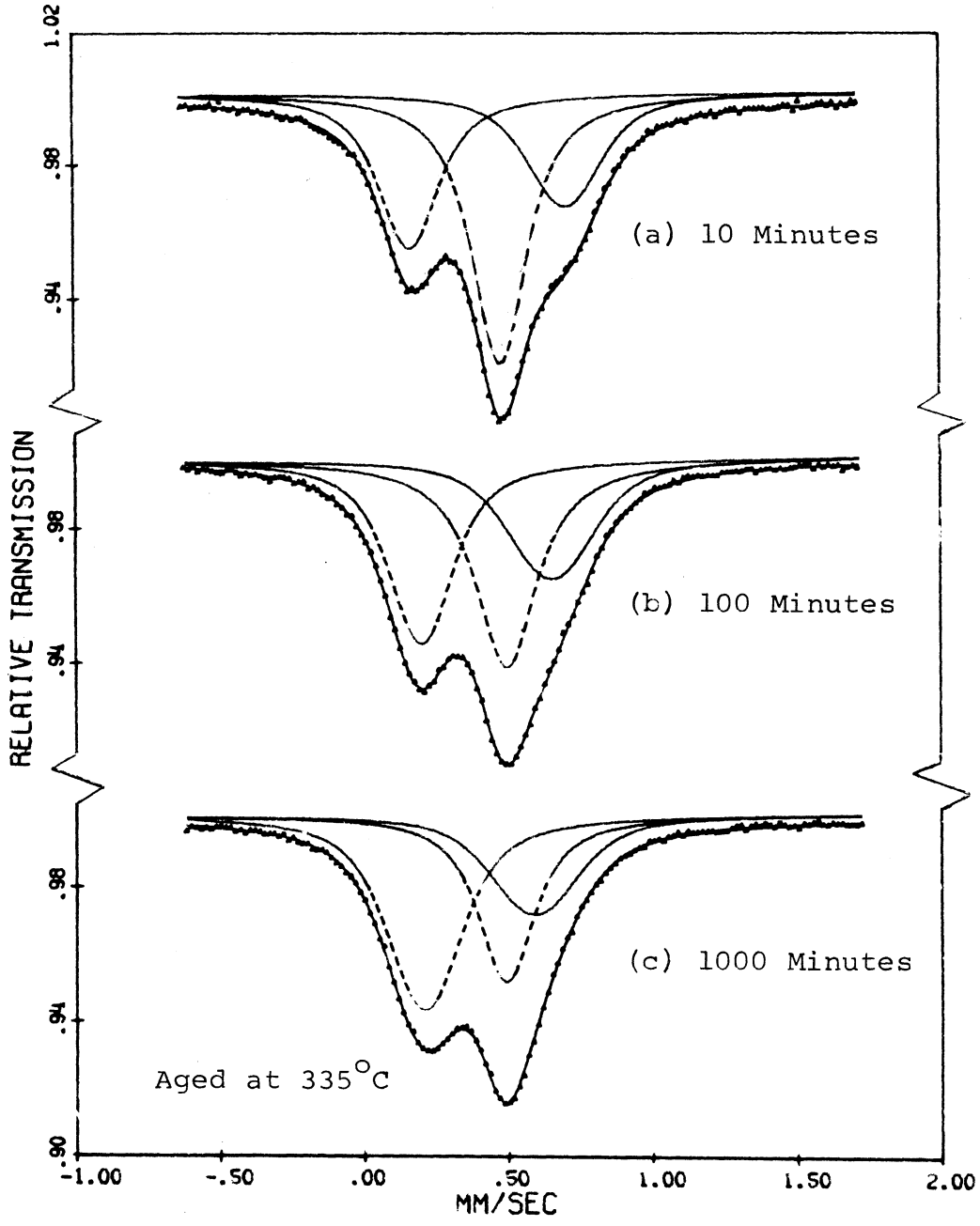

Figure IV-3.--Spectra of samples aged at 335°C fit to the sum of single Gaussian-distributed Lorentzian functions.

γ_1-iron (i.e., iron surrounded completely by Fe atoms). Therefore, Window[10] fit the class I spectra which are representative of the initial aging stage to the sum of two Gaussian-distributed Lorentzian functions--a single line to represent Fe in solid solution and an asymmetric doublet constrained to have equal areas to represent Fe in clusters.

In the unconstrained three line G-L fitting model of the present study, on the other hand, there has been no a priori assumption of the size of Fe clusters. The difference in the relative areas of the $(\gamma_2{}^L+\gamma_1)$ and $\gamma_2{}^R$ lines would then be interpreted as representing the fraction of iron surrounded entirely by Fe nearest neighbors. The results from the three line fits in Table IV-4 indicate that iron of the γ_1 variety does form during the initial aging stages. This contradicts Window's aging model.

In order to obtain a direct comparison of this more general fitting model with Window's suggested two component model, several of the aged samples were re-fit to the sum of a G-L singlet and area constrained doublet. The fitting parameters from these fits are given in Table IV-5, while two example fits are illustrated in Figure IV-4. Comparison of the results given in Tables IV-4 with those of Table IV-5 indicates that in general both methods seem to fit the data equally well. As might be expected, the χ^2/N values of the unconstrained three-line fits are less than those from fits with one parameter constrained (i.e., equal line areas in the doublet), however, their differences are small. Also, the position and area fraction of the γ_0 line behave as expected in the γ_2 area constrained fit. Thus, on the

TABLE IV-5

MÖSSBAUER SPECTRA PARAMETERS FOR ANNEALED Cu-0.6%Fe ALLOY SAMPLES ANALYZED BY THE SUM OF ONE AREA CONSTRAINED GAUSSIAN-DISTRIBUTED DOUBLET PLUS ONE SINGLET

Heat Treatment	Position[a] (mm/sec.)		γ_2 Splitting	Gaussian Width θ (mm/sec.)			Relative Area		χ^2/N
	γ_0	γ_2[b]		γ_2^L	γ_0	γ_2^R	γ_0	γ_2	
285°C, 100 min	.479(4)	.430(5)	.504(1)	.067(2)	.042(2)	.134(2)	.379(3)	.621(4)	1.49
285°C, 1000 min	.478(4)	.426(5)	.501(1)	.064(2)	.040(2)	.131(2)	.349(3)	.651(4)	1.41
285°C, 5000 min	.482(5)	.400(5)	.426(2)	.069(3)	.057(4)	.154(3)	.255(3)	.745(4)	1.09
335°C, 10 min	.480(4)	.430(4)	.509(1)	.062(2)	.027(3)	.132(3)	.425(3)	.575(5)	1.20
335°C, 100 min	.483(4)	.405(5)	.428(2)	.078(2)	.045(3)	.155(3)	.290(3)	.710(6)	1.11
335°C, 1000 min	.488(5)	.369(5)	.338(2)	.099(3)	.019(8)	.174(5)	.16(1)	.84(1)	1.46
400°C, 10 min	.484(4)	.402(4)	.428(1)	.081(2)	.032(4)	.170(3)	.327(4)	.673(6)	1.00

[a] Reference: sodium nitroprusside.

[b] Centroid of γ_2 doublet.

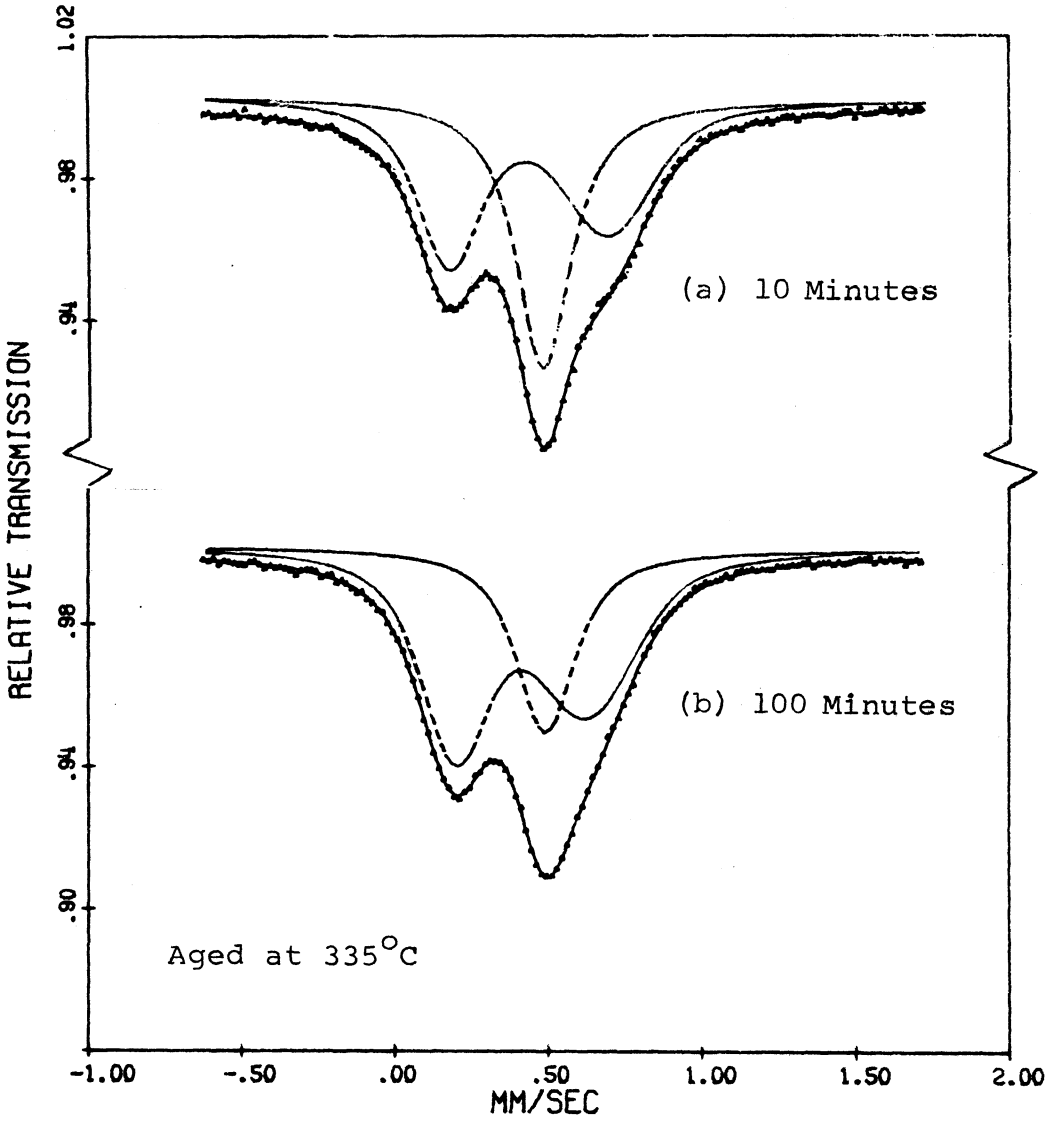

Figure IV-4.--Spectra of two samples aged at 335°C fit to the sum of a Gaussian-distributed Lorentzian singlet and area constrained doublet.

basis of the fitting results alone, it is not possible to choose between the two models. The interpretation of spectra representing the initial stages of aging will be considered further in the next section.

Aging at 335°C for times greater than 1000 min. and at 400°C for times of the order of 100 min. results in an apparent doublet in the Mössbauer spectra of the Cu-0.6%Fe alloy samples; i.e., class II spectra. The 400°C aging spectra have been fit to the sum of (a) two G-L distributions and (b) one single Lorentzian plus two single G-L functions. The parameters obtained in both cases are listed in Table IV-6. The data and fitted curves (3-line) for the 400°C aged samples are shown in Figure IV-5. This figure includes the spectrum of the 400°C-10 min. aged sample which is of type class I, and represents the incipient stage of Fe clustering. (Its fitting parameters were listed in Tables IV-4 and IV-5.)

Because of the poor resolution of the class II spectra, the three line fits were particularly difficult to make. Two pre-conditions on the fitting model were necessary to achieve convergence, both involving the γ_0 solid solution component. As in the case of the 335°C-1000 min. aged sample, the position of γ_0 was constrained to its quenched value. The second condition involved representing γ_0 as a Lorentzian instead of a Gaussian-broadened Lorentzian as before. This was necessary because in these fits the Gaussian broadening parameter θ became negative during the first iteration of the fitting program. Even with these conditions convergence was difficult to achieve.*

---

*It was necessary to operate the fitting program in an interaction mode via a Teletype terminal, so that the parameter increments at the end of each iteration could be modulated according to the

TABLE IV-6

MÖSSBAUER SPECTRA PARAMETERS FOR Cu-0.6%Fe ALLOY SAMPLES ANNEALED AT 400°C

Annealing Times	Position[b] (mm/sec.)			Line Width (mm/sec.)			Relative Area			χ^2/N
	γ_1	γ_0	γ_2	γ_1[c]	γ_0[d]	γ_2[c]	γ_1	γ_0	γ_2	
	(a) Three-line fits:[a]									
$(10)^2$min.	.168(5)	.484	.41(1)	.067(4)	.21(1)	.22(1)	.35(1)	.17(3)	.48(1)	1.34
$(10)^3$min.	.160(5)	.484	.39(1)	.057(3)	.20(3)	.162(9)	.466(7)	.10(4)	.43(1)	1.28
$(10)^4$min.	.169(5)	.484	.38(1)	.058(2)	.25(1)	.07(3)	.70(2)	.15(3)	.15(4)	1.35
	(b) Two-line fits: (L--left, R--right)									
	P(L)	P(R)		θ(L)	θ(R)		A(L)	A(R)		
$(10)^2$ min.	.180(5)	.461(5)		.065(3)	.106(3)		.461(6)	.539(2)		3.10
$(10)^3$ min.	.175(5)	.437(5)		.069(2)	.116(3)		.548(5)	.452(2)		1.57
$(10)^4$ min.	.174(5)	.433(5)		.060(2)	.102(4)		.707(5)	.293(3)		1.45

[a] The three line fits to the spectra were analyzed as the sum of two Gaussian-distributed Lorentzians (γ_1 and γ_2) plus a single Lorentzian with its position fixed at .484 mm/sec. (γ_0). The γ_2 doublet is assumed to be a broadened singlet for the purposes of fitting the data.

[b] Reference: sodium nitroprusside.

[c] Width (θ) of Gaussian broadening.

[d] FWHM of Lorentzian line.

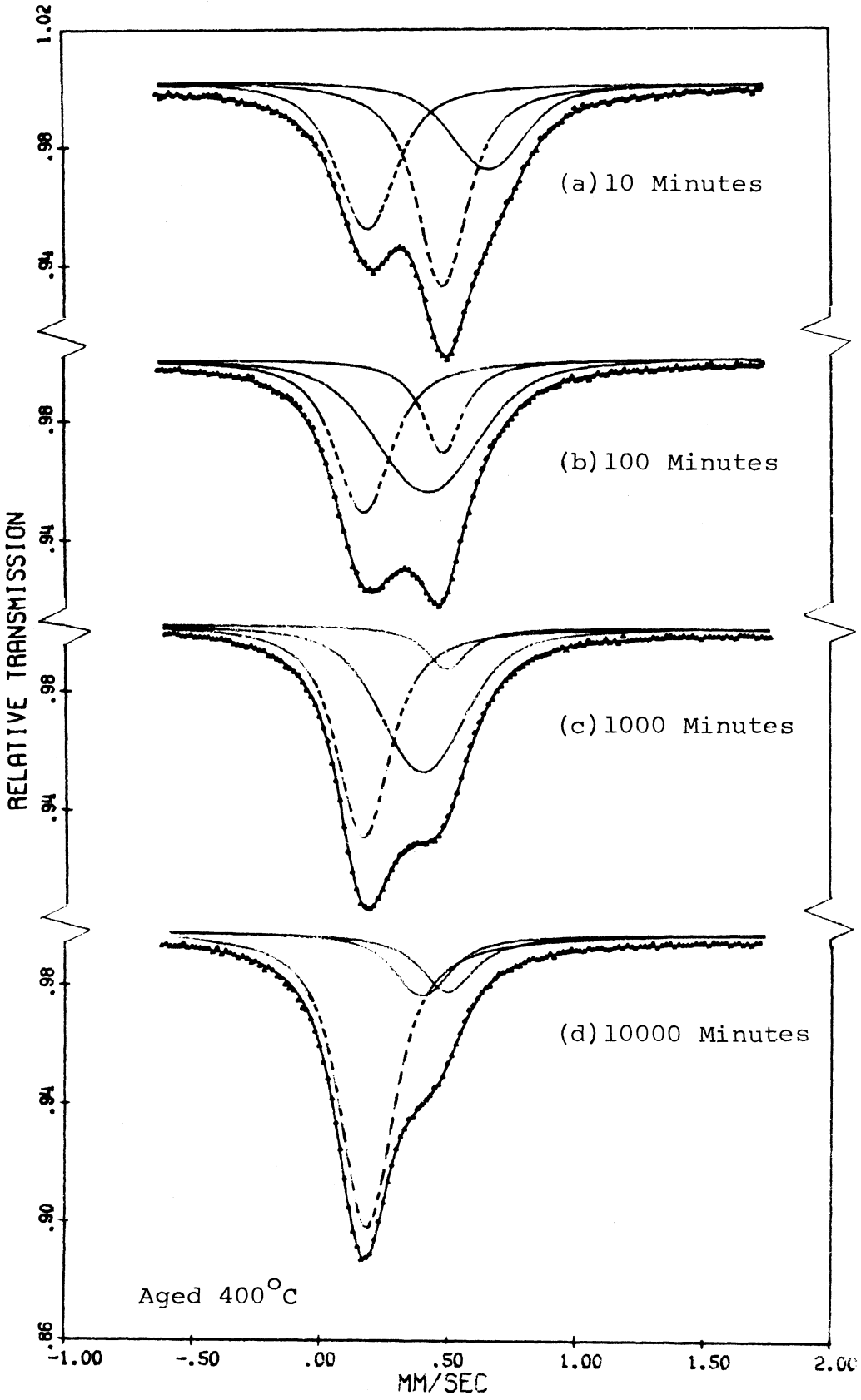

Fig. IV.5 --Gaussian-distributed Lorentzian fits to 400°C data.

The γ_2 doublet evident in the quenched and mildly aged samples is no longer resolvable in the class II spectra which represent a more advanced stage of Fe clustering. The low energy line, designated as ($\gamma_2^L+\gamma_1$) for class I spectra appears to be dominated by γ_1-iron; i.e., its position and linewidth parameters are more characteristic of those observed in well-aged samples (see below and compare Tables IV-6 and IV-7). For this reason, it has been designated as γ_1 for the three line fits in the table. The broad line whose centroid is between the γ_1 and γ_0 lines is designated γ_2 for convenience and in a qualitative manner, represents iron with a near neighbor configuration between that of γ_1-iron and iron in solid solution. The parameters from the two-line G-L fits are identified in Table IV-6 as either left (L) or right (R). As aging at 400°C progresses, the spectra more closely resemble two resonant lines as indicated by the reduction in χ^2/N for the two line fits. It should be emphasized that the assignment of the fitted lines of Table IV-6 to a particular form of iron in copper is only an approximation.

All of the Cu-0.6%Fe samples aged at 600°C produced a third type of Mössbauer spectrum (class III) which is characteristic of a more advanced stage of γ-iron precipitation. An example spectrum is illustrated in Figure IV-1(c) for an alloy aged for 200 minutes. Table IV-7 lists the Mössbauer line parameters obtained in fitting four such

---

variation of χ^2/N and the parameters from previous iterations. Even though convergence was achieved, there is of course no guarantee that the minimum in the χ^2 surface has been reached. Many false minima in the χ^2 surface undoubtedly occur because of the overlapping of the γ_0 and γ_2 components. The large variances and covariances in the parameters occurring in these fits, especially for γ_0 and γ_2, indicate that the results can only be interpreted as being approximate.

spectra (aging times from 10 to 1000 minutes) to the unconstrained sum of three single Lorentzians. Since the χ^2/N values were satisfactory for the Lorentzian fits, the subsequent application of the Gaussian-distributed Lorentzian fitting model was unnecessary. The class III spectra are characterized by relatively narrow Lorentzian lines and a large γ_1 component ($\sim$ 60% of total area) whose relative area varies only slightly with annealing time. The reappearance of a weak γ_2^R component in a position comparable to that for quenched samples is also a notable feature of these spectra.

All three classes of Mössbauer spectra observed for aged Cu-0.6%Fe in this study are illustrated in Figure IV-6. This figure shows the effects of increasing annealing temperatures on spectra produced by samples aged for 100 minutes. For comparison, a typical spectrum of a solution annealed and quenched sample has been included in the figure.

The final spectra type encountered in the aging studies of Cu-0.6%Fe was the combination of a six-line magnetic hyperfine spectrum characteristic of α-iron and the class III spectrum characteristic of advanced γ-iron precipitation. One of two such spectra obtained from cold-rolled samples that were aged for 1000 min. or more at 600°C is shown in Figure IV-7. The six-line structure in the spectrum is due to Fe in BCC α-iron precipitate particles. In this study the α-precipitates were formed by the following two processes: (1) a Cu-0.6%Fe quenched sample was annealed at 600°C for 1000 minutes and then cold-rolled and (2) a quenched sample was first cold-rolled and then aged at 600°C. The former process is the conventional method for producing α-iron precipitates below the eutectoid (γ-α transformation temperature).[85] Only

TABLE IV-7

MÖSSBAUER SPECTRA PARAMETERS FOR Cu-0.6% Fe ALLOY SAMPLES AGED AT 600°C.[a]

Annealing Time	Position[b] (mm/sec)			Line Width Γ (mm/sec)			Relative Area			x^2/N
	$\gamma_1 + \gamma_2^L$	γ_o	γ_2^R	$\gamma_1 + \gamma_2^L$	γ_o	γ_2^R	$\gamma_1 + \gamma_2^L$	γ_o	γ_2^R	
(1) AGED AT 600°C. FOLLOWING QUENCH FROM 1000°C.										
10 min.	.181(4)	.482(4)	.773(6)	.250(2)	.266(4)	.23(2)	.574(6)	.395(5)	.032(5)	1.17
$(10)^2$ min.	.178(4)	.479(5)	.775(7)	.238(2)	.248(4)	.23(3)	.631(6)	.342(5)	.027(4)	1.05
$2(10)^2$ min.	.176(4)	.481(5)	.759(6)	.240(2)	.241(5)	.22(3)	.64(1)	.34(1)	.032(8)	1.25
$(10)^3$ min.	.175(4)	.483(5)	.760(8)	.231(2)	.228(4)	.24(3)	.650(6)	.318(5)	.032(4)	1.15
(2) COLD-ROLLED FOLLOWING QUENCH FROM 1000°C. AND THEN AGED AT 600°C.										
$(10)^2$ min.	.179(4)	.483(5)	.771(8)	.242(2)	.244(5)	.23(3)	.638(8)	.334(6)	.028(5)	1.18
$(10)^3$ min.[c]										
γ-iron	.178(4)	.484(5)	.75(1)	.244(2)	.231(5)	.24(1)	.413(8)	.303(8)	.041(6)	1.06
α-iron	Centroid	Δ_{34}	Δ_{25}	Δ_{16}	A_α					
	.261(8)	1.69(1)	6.142(7)	10.64(1)	0.24(1)					

[a] Spectra were fit to a sum of Lorentzian lines using Equation (III.2).

[b] Reference: sodium nitroprusside.

[c] Contained both the γ-lines and six α-iron lines.

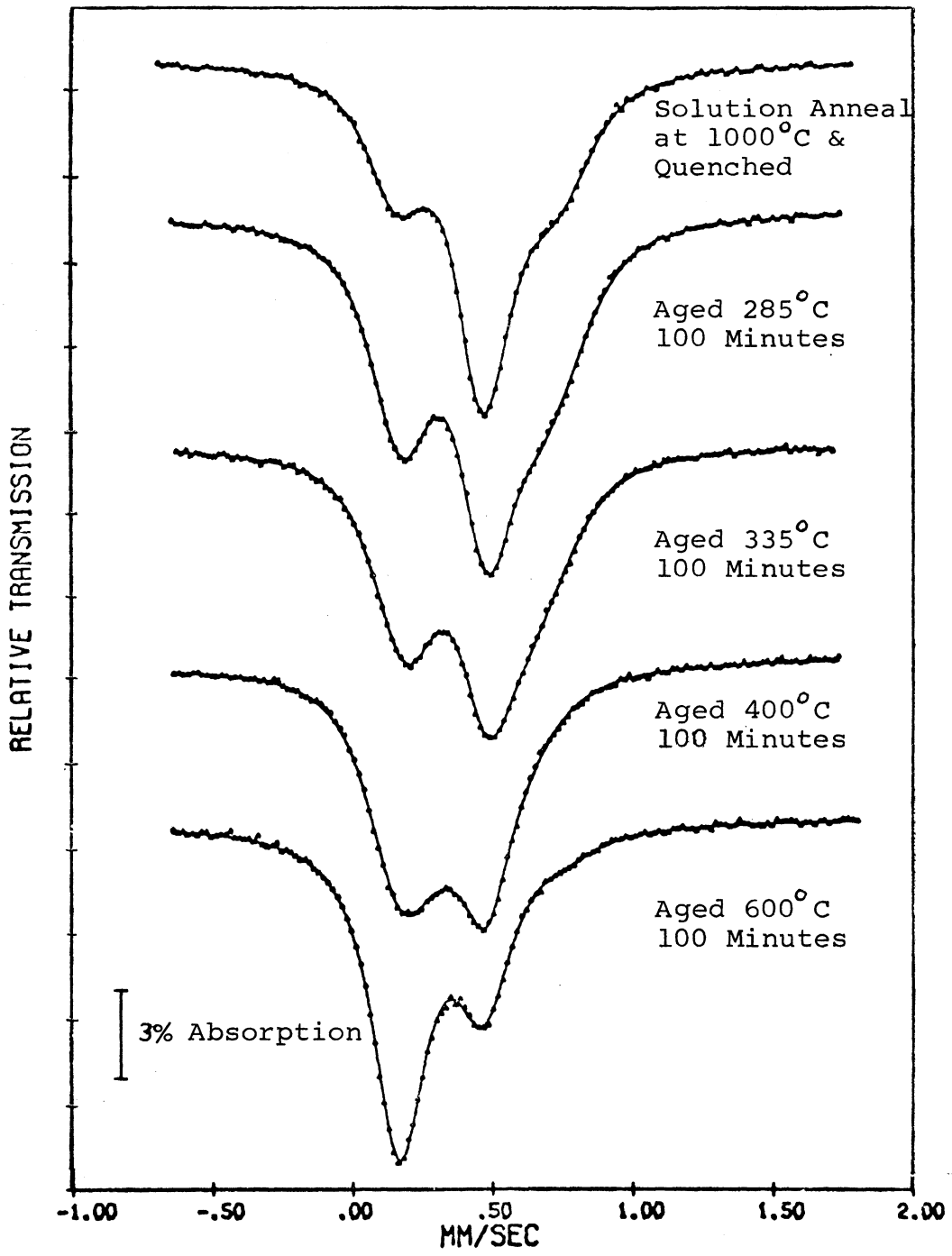

Figure IV-6.--Mössbauer absorption spectra showing the various aging stages of a Cu-0.6%Fe alloy.

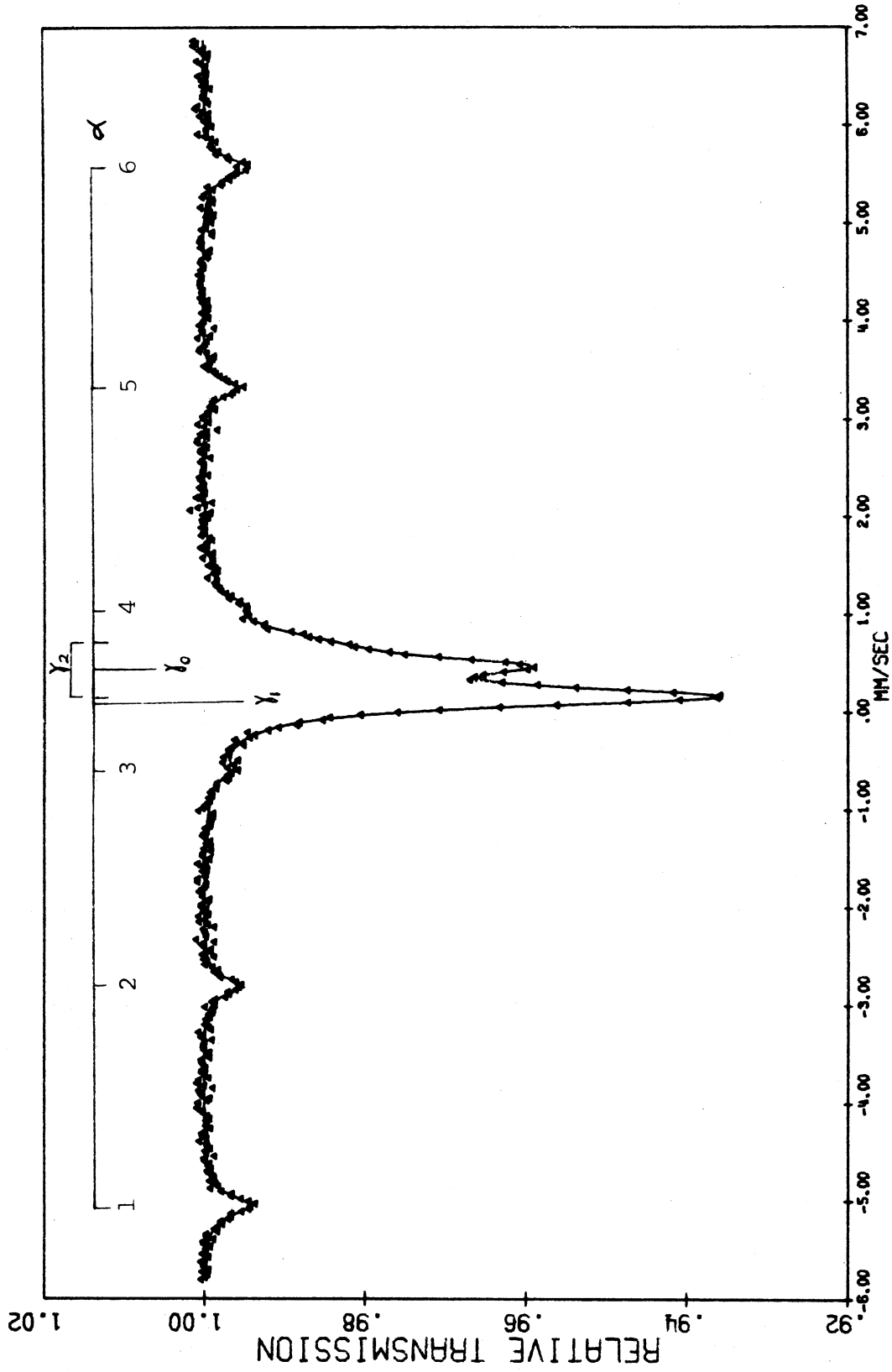

Figure IV-7.--Mössbauer absorption spectrum of a Cu-0.6%Fe alloy sample which was quenched, cold-rolled and then aged at 600°C for 1000 minutes.

one sample was prepared in this manner. The second method was used to prepare four samples, all aged at 600°C for various times. Only the two samples aged for 1000 and 2000 minutes exhibited α-iron lines in their Mössbauer spectra. Those aged for times less than 1000 minutes produced spectra identical to the class III spectra obtained from the straightforward aging of solution annealed (quenched) samples at 600°C. The results of the cold-rolling experiments are summarized in Table IV-7 for samples that were aged for 100 and 1000 minutes.

3. Results of Resistivity Measurements

The resistivity measurement apparatus and procedure were discussed in Section III-C. These measurements were made to provide a means of comparing the Mössbauer results of this study with the resistivity results of earlier aging and radiation effects studies of Cu-Fe alloys.[3][5] The resistivity results from quenched and aged Cu-0.6% Fe samples are summarized in Table IV-8. For each sample, the Fe concentration in solid solution has been obtained from measured resistivity values using the experimental curve of Boltax[3] (also, see Linde[133]). For Cu-Fe alloys with Fe concentrations of $\lesssim$0.5 wt.% this curve is a straight line with a slope of about 8.2 $\mu\Omega$-cm per atom% (See Figure IV-13). Also given in the table for the aged samples is the fraction of Fe which is transformed ($\varepsilon \rightarrow \gamma$) as determined by

$$f_\rho = \frac{\rho_o - \rho}{\rho_o - \rho_f} \qquad \text{(IV.1)}$$

where ρ_o is the as-quenched resistivity, ρ the aged resistivity, and

TABLE IV-8

COMPARISON OF RESISTIVITY AND MÖSSBAUER RESULTS FOR HEAT TREATED Cu-Fe ALLOYS

Heat Treatment	Resistivity ($\mu\Omega$-cm)	C_o^{ρ}	f_{ρ}	$C_{\gamma o}^{M}$	f_M
Ave. Quenched	6.29(8)	.56	-	.41(1)	-
Quenched and Rolled	6.60(5)	.59	-	.461(4)	-
.1% Fe Quenched	2.51(8)	.09	-	.080(4)	-
285°C, 100 min.	5.57(6)	.47	.14	.265(2)	.35
285°C, 1000 min.	5.33(5)	.44	.24	.233(3)	.48
285°C, 5000 min.	4.67(5)	.36	.41	.19(1)	.60
335°C, 10 min.	5.52(5)	.46	.15	.294(2)	.30
335°C, 100 min.	4.91(4)	.38	.35	.24(1)	.43
335°C, 1000 min.	4.12(4)	.29	.54	.19(5)	.59
400°C, 10 min.	4.81(5)	.37	.35	.263(6)	.39
400°C, 100 min.	3.51(4)	.21	.66	.11(2)	.80
400°C, 1000 min.	2.86(3)	.13	.81	.07(2)	.91
400°C, 10,000 min.	2.58(4)	.10	.87	.09(2)	.84
600°C, 200 min.	3.68(3)	.23		.214(6)	
600°C, 1000 min.	3.49(3)	.215		.200(3)	

* Symbols:

ρ = resistivity, M = Mössbauer

f = fraction transformed to Fe clusters

C_o = Fe Concentration (atom%) in solid solution

ρ_f the equilibrium resistivity obtained from the equilibrium solubility at the aging temperature.*

For comparison, the Fe concentration in solid solution determined from the Mössbauer spectra (i.e., from the γ_o component of the three-line G-L fits)** is given for each sample. In addition, the fraction of Fe transformed f_M, which was calculated from the γ_o area fractions of the spectra for each sample in the quenched and aged conditions, is also listed in Table IV-8. Equation (IV-1) was used to determine f_M with area fractions replacing the resistivity values. (A nominal value of $A_f = .94$ was used to represent the equilibrium γ_o area fraction for the 285°-400°C aged samples). The fractional transformation values obtained from both measurement techniques are plotted as a function of isothermal annealing time in Figure IV-8. The large errors associated with the Mössbauer results of the 400°C data are due to the very poor resolution of the class II spectra. These errors were obtained from the fitting program and do not represent any inaccuracies in the assumed model.

The reasons for the significant differences in the fractional transformation values, as well as the estimated concentration of Fe in solid solution (γ_o), obtained from the two experimental methods will be discussed in Section IV-C.

---

*Estimated to be about 2 μΩ-cm for samples aged at temperatures of 285° - 400°C.

**For the aged samples the atom concentrations (in percent) were estimated from $C_o = 0.63A_o$, where A_o is the area fraction of the γ_o component and the constant 0.63 is the total atom percent Fe in the Cu-Fe alloy. Because of the small effective thicknesses involved, the errors associated with this approximation ($\lesssim 4\%$) are less than the uncertainty in the fitting model. In the case of quenched samples, for which γ_o is the dominant component, the procedure described in Section II-A.2 was used (i.e., Equation II.14).

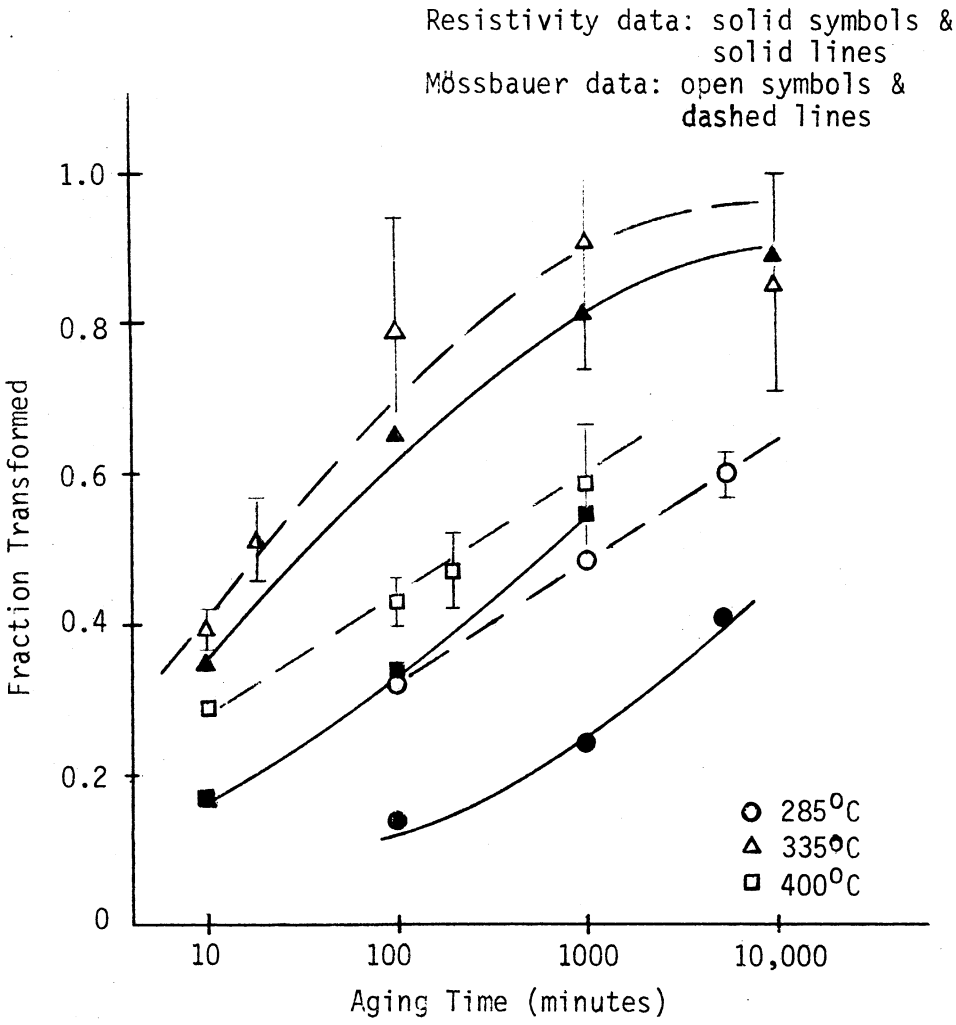

Figure IV-8.--Fraction of iron transformed from the solid solution phase to iron clusters as determined by Mössbauer and resistivity measurements.

C. Discussion of Annealing Results

The Mössbauer measurements of quenched and aged Cu-0.6% Fe alloy samples indicate that a variety of complex spectra are produced as a result of Fe cluster formation in the Cu matrix. This complexity ranges from the resolved two component spectra (γ_0 singlet and γ_2 doublet) of the quenched samples to the poorly resolved three line (class I) and two line (class II) spectra of samples isothermally aged at temperatures in the range 285° - 400°C. The samples aged at 600°C produced adequately resolved three component spectra (class III) that can be interpreted from our existing knowledge of the metallurgy of Cu-Fe alloys aged at temperatures 550°C or greater.[4] [84] The interpretation of the spectra of quenched alloys has been made by Window[8] and confirmed by Reno and Swartzenruber[12] using perturbed angular correlation measurement techniques (see Section II-B).

Before considering the effects of fast neutrons on these alloys, it is necessary to characterize the ME spectra associated with the early stages of aging; i.e., to relate the components of the class I and II spectra to the different phases or configurations of Fe in copper. Such a characterization is made in the present section through an argument based in part upon the systematic trends of the spectra and also upon metallurgical considerations.

1. Spectra Systematics and Other Considerations

The amount of Fe clustering in solution annealed and quenched alloys is a function of the Fe solute atom concentration and the quality of the quench. The former is illustrated in Figure IV-9, which shows the variation of the area fractions for the γ_0 singlet

and γ_2 doublet as a function of Fe concentration. The effect of cold-rolling on the break-up of Fe clusters is also indicated in the figure for the 0.6% Fe samples.

The γ_2 doublet is produced by small Fe clusters of two or more atoms. As discussed in Section II-B and Appendix B (also see Window[15]), the presence of one or more Fe neighbors causes a distortion in the 3d charge distribution of the resonant atom which produces an electric field gradient at the Fe^{57} nucleus. This in turn splits the excited level into two doubly degenerate states which give rise to the γ_2 component's splitting. For the Fe concentrations considered, the doublet's splitting remained essentially unchanged (for high quality quenches) indicating that the size of clusters remained essentially constant (probably two to four atoms) with an increase in Fe concentration up to 0.63%. (The magnitude of the splitting is slightly smaller for the G-L function fits than those using simple Lorentzian functions.) The increase in γ_2's area fraction is then probably associated with an increase in the number of small clusters. In the case of the less rapid quenches (e.g., see the 0.6% Fe "Q" sample in Table IV-1), a decrease in the doublet's splitting occurred in conjunction with its increase in relative area, indicating larger clusters were formed. The resolution of the spectra for the quenched samples is sufficient to allow an accurate determination of the γ_0 and γ_2 area fractions, and through Equation (II.14), the Fe concentrations of the two configurations.

The other spectra type for which an unambiguous characterization can be made is the class III spectra (see Figure IV-1c) obtained for the

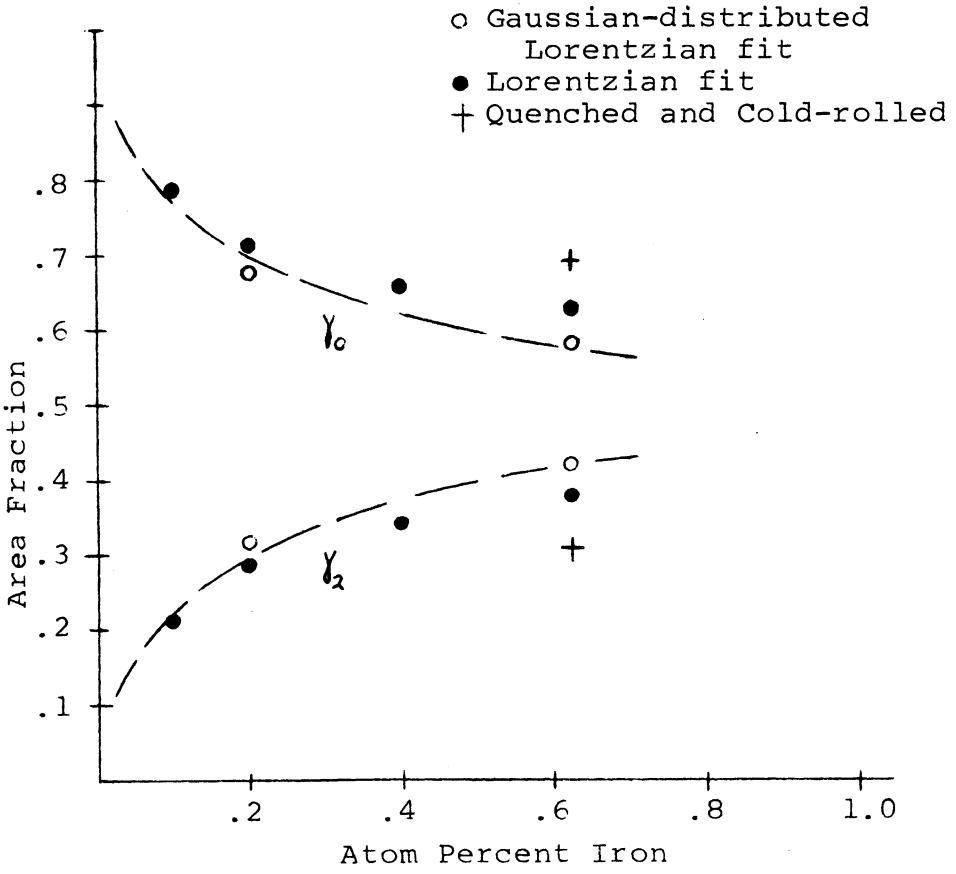

Figure IV-9.--Variation of γ_0 and γ_2 area fractions for quenched samples as a function of atom percent iron in copper.

"well aged" Cu-0.6% Fe samples (i.e., those aged at 600°C).* In these spectra the large component (γ_1) centered at approximately .17 - .18 mm/sec is mainly produced by γ-iron precipitates. Electron microscopy studies[85] have revealed these precipitates to be spherical in shape and fully coherent with the copper lattice.[85] The central component of these spectra is located at essentially the same position as the peak due to solid solution Fe (γ_0) in quenched samples, and is so identified. The small peak designated γ_2^R is the high energy component of the γ_2 doublet observed in the quenched samples, and can be associated with Fe pairs or small clusters in the Cu matrix. The other member of the doublet is located under the large γ_1 peak. That the γ_1 resonance line could be fit to a Lorentzian with relatively narrow width indicates the predominance of a single iron environment. Like the spectra of quenched samples, a fairly accurate determination of phase concentrations is possible through the relative areas of the spectral components.

Aging in the temperature range 285° - 400°C produces spectra that are intermediate to those discussed above. In the very early stages, the spectra appear to have three broad, partially resolved lines as was illustrated in Figures IV-3 and IV-4. Spectra of this type were identified as class I and were fit to (a) the sum of three Gaussian-distributed Lorentzian (G-L) functions as well as (b) the sum of a G-L singlet and an area constrained doublet. The second model assumes that Fe which is not in solid solution (γ_0 singlet) is in the form of clusters of a few atoms having a majority of copper nearest neighbors. This model was

---

*The expression "well aged" used here implies definite γ-iron (coherent) precipitate formation and should not be confused with the metallurgical connotation -- i.e., the formation of large incoherent precipitates with the concurrent reduction of hardness.

recently suggested by Window.[10] The first model makes no such assumption and has been adopted in the present study to characterize the Cu-0.6% Fe spectra. The results of both fitting schemes were summarized in Tables IV-4 and IV-5 and will be further compared below.

The effects of increased Fe clustering on the doublet's splitting and position are shown in Figures IV-10 and IV-11, respectively. (Both the γ_2 centroid (lower) and γ_2^R position (upper) are shown in Figure IV-11). For reference the γ_2 splitting and position parameters for quenched samples, designated by a cross, and the 600°-aged samples are also plotted in the figures. The open symbols represent the three component model (a), while the solid symbols represent the constrained two component model (b). The dashed lines for a given aging temperature are drawn to indicate trends in the variation of the plotted parameters.

In all cases the area constrained fitting model -- i.e., (b) above -- produced somewhat smaller splittings and greater decreases in the γ_2 centroid's position. Actually, the average parameter values of the spectral distribution probably fall within the limits determined by the two models. Of course, all of the foregoing is predicated on the assumption that the distribution of quadrupole splittings and isomer shifts of Fe^{57} in a variety of Fe and Cu nearest neighbor configurations can be effectively represented by Gaussian-broadened Lorentzians.

A major change in the trend of decreasing γ_2 position occurs for the samples aged at 400°C for 100 to 10,000 minutes (see lower graph of Figure IV-11). Spectra of these samples are class II and were fit to both two and three components; i.e., two G-L functions or one Lorentzian constrained at .484 mm/sec plus two G-L functions. The very broad singlet occuring between γ_0 and the left component γ_1 (see Figure IV-5

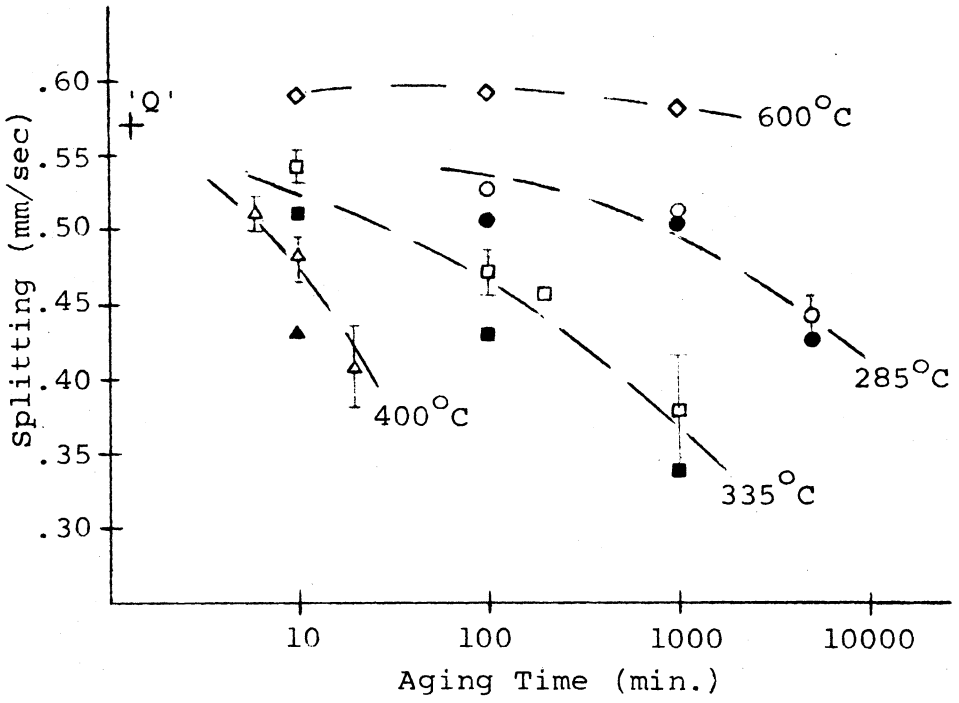

Figure IV-10.--Splitting of γ_2 doublet as a function of aging treatment.

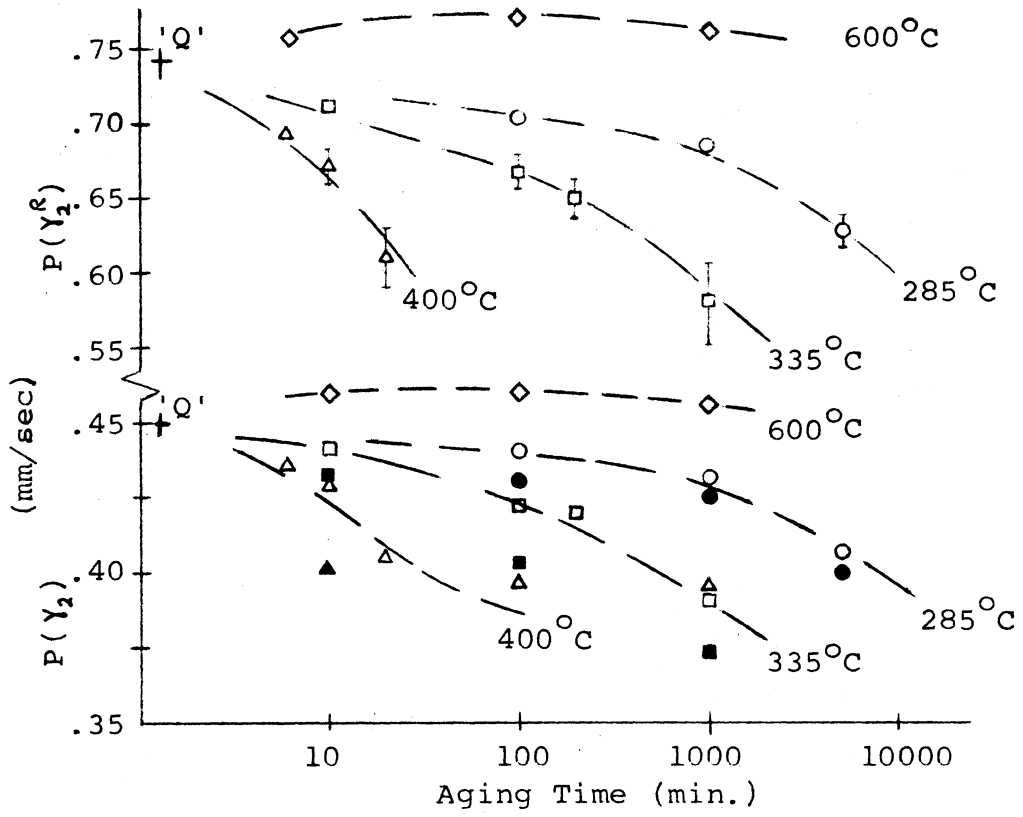

Figure IV-11.--Position of γ_2 centroid and γ_2^R as a function of aging treatment.

and Table IV-6) was taken to represent γ_2 iron; i.e., Fe^{57} with both Cu and Fe nearest neighbors. In these cases, the number of Fe nearest neighbors probably exceeds 5 or 6 (see Appendix B and discussion in Section IV-C.2). The large deviation of the centroid of this broad line from the isomer shift trend of γ_2 shown in Figure IV-11 indicates the failure of this simplified model to adequately characterize the class II spectra (except possibly for the 400°C - 10,000 min. sample). Certainly one would expect a monotonic decrease in isomer shift, although not necessarily linear, as Fe atoms are added to the nearest neighbor shell of the resonance atom. In the case of the 400°C - 10,000 minute sample, the broad γ_2 component might be half of a doublet, the other half being masked by the dominate γ_1 line.

Two other trends in the class I spectra (Table IV-4) are important. First, the position of the left component ($\gamma_2^L + \gamma_1$) increases in energy upon aging (from ~.16 mm/sec for quenched samples to ~.20 mm/sec for the sample aged 1000 min. at 335°C). This can be interpreted as being caused by a shift in γ_2^L, suggesting that small Fe clusters predominate. (Recall that the established position for the γ_1 line is at ~.17 mm/sec.) The other trend is associated with the behavior of the width (Gaussian broadening) of the ($\gamma_2^L + \gamma_1$) line. For the 285°C aging data, this width remains fairly constant and is approximately equal to that of the quenched samples (i.e., about .065 mm/sec). Since there is also a definite increase in the γ_2 area fraction and a concurrent decrease in splitting and isomer shift for these samples, it can be concluded that both the fraction of iron in clusters and average cluster size are increasing. The constancy in γ_2^L's width is then most likely caused by the simultaneous decrease

in the doublet's splitting and isomer shift. (This effect, as noted by Window[8] in a variety of quenched Cu-1.1% Fe alloy samples, produces a relatively narrow low energy member and broadened high energy member of the γ_2 doublet -- this is certainly evident in both Tables IV-4 and IV-5). In the case of the 335°C-aging data, a marked increase in the $(\gamma_2^L + \gamma_1)$ member's Gaussian width occurs with increasing annealing time. This could very well be the result of γ_1-iron being formed; i.e., Fe with at least its nearest neighbor shell (12 atoms) filled with other Fe atoms.

The same trends in $(\gamma_2^L + \gamma_1)$'s position and width are noted for the samples aged at 400°C for times in the range of 6 - 20 minutes. However, further annealing at this temperature results in a significant change in both the position and width parameters of the $(\gamma_2^L + \gamma_1)$ component. Comparison of Tables IV-4 and IV-6, reveals that the position of $(\gamma_2^L + \gamma_1)$ has decreased from .20 mm/sec (20 min. anneal) to about .17 mm/sec (100 to 10,000 min. anneals), while its width θ has decreased from .098 mm/sec to approximately .06 mm/sec. These values are similar to those associated with the γ_1-iron line of the well aged samples (compare Tables IV-6 and IV-7).* Thus, aging at 400°C for times 100 minutes or greater seems to produce significant quantities of γ_1-iron in Cu-0.6% Fe. The growth of these precipitates is characterized by the increase in the area

---

*Comparison of the width parameters (one Gaussian broadened, the other Lorentzian) can be made by converting θ for the 400°C data to the FWHM value for the convolution function by using Figure III-5. For example, the 100 minute case ($\theta \simeq .067$ mm/sec) yields an FWHM of about .25 mm/sec.

fraction of the left component in the two line fits (Table IV-6) and the decrease in the position of the right member.

The foregoing discussion emphasized parameters which qualitatively characterize the stages of aging in Cu-Fe alloys. For the purposes of this study it is desirable to be able to quantitatively determine the concentration of iron in its several forms in copper; i.e., α-iron precipitate, γ-iron precipitate (γ_1), Fe atoms with a mixed nearest neighbor configuration (γ_2), and solid solution iron (γ_0). As discussed in Section II-A.2, the resonant line area fraction either directly (for $T_i << 1$) or through Equation (II.14), is related to the fractional concentrations of Fe^{57} in an environment that gives rise to that particular spectral component. In the cases of quenched and well-aged (class III spectra) samples, the resolution between spectral components is sufficient to permit the quantitative determination of iron in its various phases (configurations). This is also true for those samples containing both γ- and α-iron precipitates (see Figure IV-7 and Table IV-7).

Unfortunately, however, such an unambiguous determination is not possible from the class I and II spectra associated with the early stages of aging. In the case of the partially resolved class I spectra, the relative fractions of iron in solid soultion and Fe clusters is obtainable if it is assumed that no γ_1-iron has been formed (i.e., clusters consist of 12 Fe atoms or less). Then the results of the constrained two component fitting model (singlet plus an area constrained doublet) apply. On the other hand, if some clusters of iron have grown to sizes sufficient to contain γ_1-iron (Fe^{57} with all 12 nearest neighbors being Fe atoms), it would be

necessary to interpret the aging data using the three component Guassian-Lorentzian fitting model. In any event, the actual fraction of Fe solute atoms remaining in solid solution should be bounded by those values predicted by the two G-L fitting models (refer to Tables IV-4 and IV-5). To estimate this fraction, one could use the mean value of the γ_0 area fractions obtained from the two fitting models. The uncertainty in the Fe solute atom concentration so obtained would range from about 5% for the 285°C and 335°C - 10 min. aging data to as much as 32% for the 335°C - 1000 min. data.

The resolution problem worsens in the case of class II spectra (samples aged at 400°C for 100 min. or more), and it becomes virtually impossible to make a definite phase identification from the spectra (except possibly in the case of the 400°C - $(10)^4$ min. sample). In these cases, both two and three line fitting models were used (Section B) to approximate the spectral contributions of γ_1 and γ_0-iron, and Fe atoms with a mixed Cu and Fe nearest neighbor shell configuration (γ_2). An exact quantitative determination of the Fe concentration in either cluster or solid solution configurations is not possible from these fits. However, either the "γ_1" component from the three line fits or the left component (γ_L) from the two line fits are a measure of the fraction of iron in large clusters. An increase in their area fractions indicates an increase in the number of Fe atoms in large clusters. (Consideration of cluster size for the various aging stages is made below.)

It is desirable for the irradiation effects phase of this study to be able to unambiguously measure changes occuring in the number of Fe atoms associated with the small clusters formed by aging

or irradiation. For this purpose, the area fraction of the ($\gamma_2^L + \gamma_1$) line in class I spectra will be used. (For convenience this component will be referred to as γ_L.) As shown in Table IV-9, the fitting parameters of γ_L, especially its area, are relatively insensitive to the fitting method used. Several fitting trials (as identified in Table IV-9) incorporating various constraints in the Gaussian-Lorentzian fitting models were tried on the 285°C - 5000 min. and 335°C - 1000 min. aging data in order to determine the sensitivity of the resonant line parameters to the fitting model. The results given in the table clearly demonstrate that the mixing of the γ_0 and γ_2^R components precludes an accurate determination of their relative areas. Since the γ_L component is relatively well separated from the remaining portion of the spectrum, its fitting parameters have remained essentially invariant of the fitting model used.

As previously discussed, γ_L consists of the left member of the γ_2 doublet representing Fe atoms with a Cu, Fe mixture of nearest neighbors plus possibly γ_1 representing Fe atoms with only Fe nearest neighbors. In either case it definitely represents iron in cluster form. Also, its area fraction is sensitive to small changes in the number of Fe atoms in clusters and thus can be used as an indicator of cluster formation or dissolution in the neutron irradiation studies (see Sections D and E). It is important to note that in all of the class I spectra fit by the two methods, the doubling of the area fraction of γ_L from the three-line model equals the γ_2 area fraction of the constrained two component model. The variation of the area fraction of γ_L with aging time at the four annealing temperatures

TABLE IV-9

COMPARISONS OF DIFFERENT GAUSSIAN DISTRIBURTED LORENTZIAN FITTING METHODS FOR CLASS I SPECTRA OF TWO AGED SAMPLES

Type of Fit	Position (mm/sec.)			Gaussian Width (mm/sec.)			Relative Area			χ^2/N
	$\gamma_2^L + \gamma_1$	γ_o	γ_2^R	$\gamma_2^L + \gamma_1$	γ_o	γ_2^R	$\gamma_2^L + \gamma_1$	γ_o	γ_2^R	
	(1) Sample aged at 285°C for 5000 minutes									
(a)	.187(4)	.487(6)	.63(1)	.069(2)	.065(10)	.14(1)	.374(3)	.30(2)	.32(1)	1.09
(b)	.187(4)	.484	.62(1)	.069(2)	.06(1)	.15(1)	.373(3)	.27(4)	.36(3)	1.10
(c)	.187(6)	.482(5)	.613(6)	.069(2)	.057(4)	.154(3)	.373(4)	.255(3)	.373(4)	1.09
	(2) Sample aged at 335°C for 1000 minutes									
(a)	.202(5)	.493(6)	.60(5)	.107(2)	.06(1)	.14(3)	.440(6)	.36(5)	.20(9)	1.28
(b)	.202(5)	.484	.58(4)	.106(2)	.05(1)	.14(2)	.439(6)	.31(8)	.25(7)	1.33
(c)	.200(6)	.488(5)	.538(6)	.099(2)	.02(1)	.174(5)	.420(6)	.16(1)	.420(4)	1.36

(a) Fit to three single unconstrained G-L functions.

(b) Same as (a) except γ_o line was constrained at .484 mm/sec.

(c) Fit to G-L singlet (γ_o) plus G-L doublet (γ_2) constrained to have equal areas.

studied is illustrated in Figure IV-12. The saturation of the 600°C data for long aging times indicates that the coalescence stage of precipitate particle growth has been reached (for discussion, see the next section).

2. Metallurgical Considerations

a. Aging at 600°C.--The metallurgy of copper-rich Cu-Fe alloys aged at temperatures of 550°C and greater has been well established. Easterling[134] using thin foil electron microscopy has shown that in this temperature range nucleation of γ-precipitates occurs homogeneously leading to fully coherent spherical precipitate particles. The precipitation kinetics studies of Denney[4] (see Section II-C) in this temperature range indicate that the precipitate growth is diffusion controlled with an activation energy of 1.65 ev. The Mössbauer results obtained in this study for a Cu-0.63 at.% Fe alloy aged at 600°C (see Table IV-7 and Figure IV-12) show that the fraction of iron in solid solution (γ_0) and γ-precipitates (γ_1) remains essentially constant for annealing times of about 1000 minutes or greater. This suggests precipitate growth by the coarsening mechanism;[135] i.e., the growth of large precipitate particles at the expense of smaller, less stable particles which are eventually redissolved. The extrapolation of the γ_0 area fractions (Table IV-7) to longer aging times indicates that about 30% of the Fe atoms should be in solid solution at equilibrium. This corresponds to an iron solubility in copper of about 0.2% at 600°C.

The reappearance of the high velocity member of the γ_2 doublet in the 600°C-aged samples at a location comparable to γ_2^R's position in

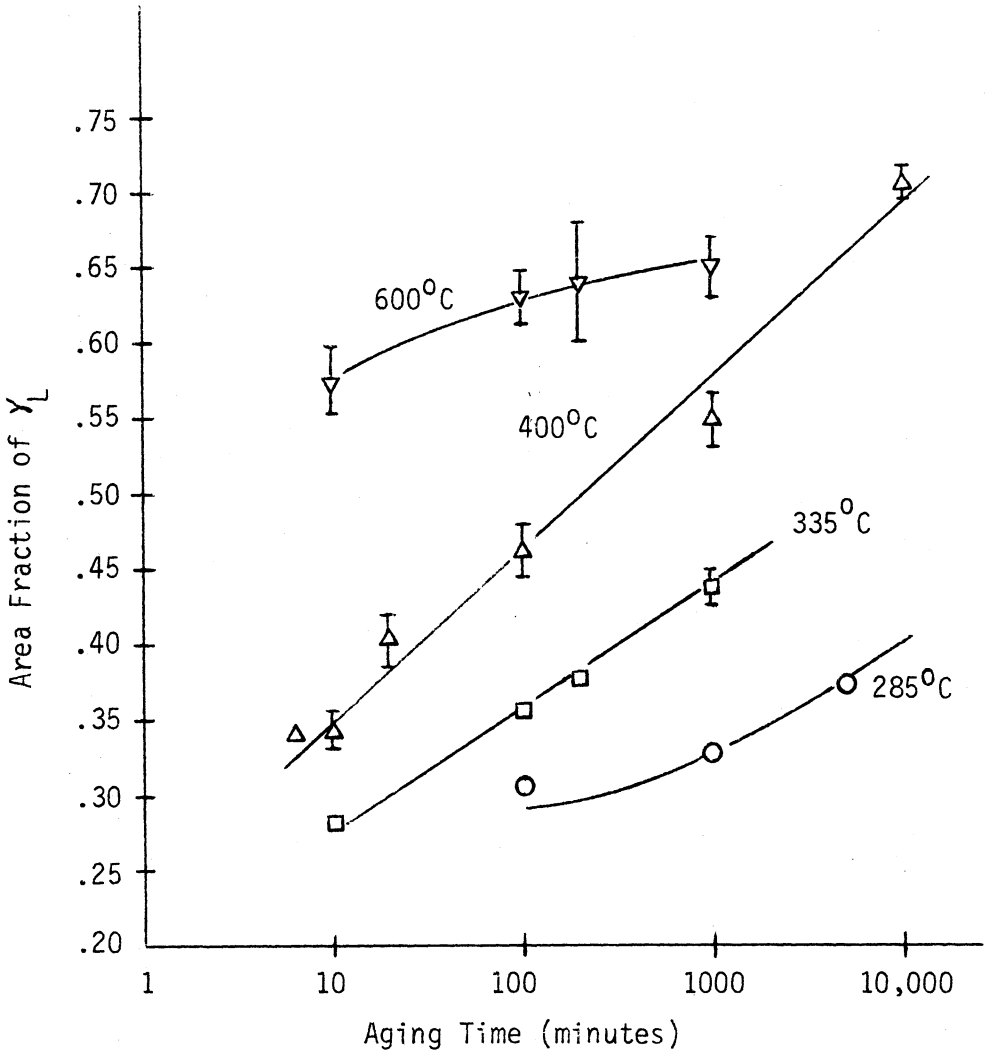

Figure IV-12.--Variation of the area fraction of the γ_L component with aging treatment.

quenched alloy samples was noted in the previous section. This is interpreted as being caused by small Fe clusters occuring in the iron-depleted Cu matrix. It is interesting to compare the atom concentration of iron in the form of small clusters in the case of the 600°C samples (obtained from twice the area fraction of γ_2^R in Table IV-7) with that of γ_2 for the quenched Cu-0.2%Fe alloy. (As discussed above, approximately 0.2% Fe is in solid solution in the 600°C samples.) Using the results of Figure IV-9 this value is about .06 at.% for the quenched sample, while the value obtained from the 600°C data is about .04 at.%. The closeness of these values suggests a common cause, possibly the random formation of Fe pairs and small clusters in the copper matrix.

Assuming random Fe clustering, the ratio $A(\gamma_2)/(A(\gamma_0) + A(\gamma_2))$ should be approximately equal to the sum of the probabilities for the occurrence of a cluster of n Fe atoms within one nearest neighbor shell; i.e.,

$$\sum_{n=2} P(n) = \sum_{n=2} \binom{13}{n} c^n (1 - c)^{13-n},$$

where n represents the number of Fe atoms in a cluster and c the Fe concentration. For random Fe pair formation, by far the most probable occurrence, $P(2) \sim 3x\ (10)^{-4}$, which is two orders of magnitude smaller than the above ratio. Thus, the γ_2 doublet in both cases is not caused by random Fe clustering. There are two other possibilities for its occurrence in the 600°C samples. It could be the result of the same homogeneous process which produced clusters in the samples aged at lower termperatures, or it could be produced by residual Fe clusters leftover from small precipitates being redissolved in the coarsening process. In either event, these small clusters should be unstable in the presence of large γ or α precipitates.

The Mössbauer results of this study also show that a γ-α transformation occurs in cold worked samples which were aged at 600°C for times of 1000 and 2000 minutes; the cold rolling treatment can be given either after aging (as previously demonstrated[85]) or before aging (see Figure IV-7 and Table IV-6). The mechanism initiating this transformation has been established by Easterling and coworkers[85][136] to be the passage of a moving dislocation through a large γ-precipitate particle of a critical size (~200 Å in diameter). During cold working following aging, the α-phase was found by these authors to nucleate as disks on dislocations in γ-precipitate particles. Although their microstructure is unknown, the transformation mechanism in the samples of this study which were cold-worked prior to aging is probably similar to the above mechanism. Dislocations existing after cold working very likey act as nucleation sites for γ-iron precipitation during annealing at 600°C. Upon quenching from the aging temperature, the dislocations could move under thermal stresses thereby initiating the γ-α martensitic transformation. The fact that there were no α-lines in the ME spectra of samples aged for less than 1000 minutes indicates that the γ-precipitate particles had not reached critical size. It is estimated that the 1000 min. anneal at 600°C produced γ-precipitates of 110-200 Å in diameter[7][86] which indicates a critical particle size of about 200 Å for the transformation.

b. Low Temperature Aging: Mössbauer Versus Resistivity.-- Until the recent Mössbauer study by Window[10] and the present work, the only extensive study of precipitation processes in copper-rich Cu-Fe alloys for aging treatments at 400°C and below was the work reported by Boltax.[3] Since the γ-precipitates (or clusters) formed at these temperatures

are too small to observe by electron microscopy or x-rays, previous studies have involved the measurement of either transport, magnetic or hardness properties (see Section II-C). In the case of Boltax, resistivity measurements were used to follow the precipitation of γ-iron in a Cu-1.7wt%Fe alloy after aging at temperatures from 200° - 700°C. Resistivity measurements were also made in the present study so that the Mössbauer results of the 0.6at% Fe alloy could be compared directly to the resistivity results of Boltax.[3][5] The resistivity results of this study were summarized in Table IV-8 along with the corresponding Mössbauer results; their relationship is discussed below. A discussion of precipitation kinetics based on the resistivity measurements from both studies is delayed until later in this section.

The basic assumption used by Boltax to interpret the resistivity data of aged[3] and irradiated[5] Cu-Fe alloys (see Sections II-c and II.D) was that the only contributors to an aged alloy's residual resistivity (i.e., $\Delta\rho$ caused by the presence of impurity atoms -- in this case iron) are the Fe atoms in solid solution. In particular, the effects of small γ-precipitates or clusters were ignored. Comparison of Mössbauer and resistivity data (see Table IV-8) indicates that the above assumption is erroneous for the early stages of aging. The results show that the concentrations of Fe in solid solution predicted from the Mössbauer spectra (using either the three line or constrained two component G-L fitting models) are significantly less than those values derived from the resistivity results. The differences are due to the inability of the resistivity measurements to distinguish between electron scattering by small Fe clusters and that by isolated

Fe atoms in solid solution. The Mössbauer data indicate that the contribution to the resistivity by small Fe clusters can be significant.

This effect is illustrated in Figure IV-13 where the resistivity values of aged and quenched alloys (vertical axis) are plotted against the concentration of Fe in solid solution (atom %) as determined from the area fraction of the γ_0 component in the Mössbauer spectra. As a reference, the straight line representing the extrapolation of measured resistivity values for Cu with impurity concentrations of Fe ($\lesssim$0.3at%) has been included.[3] This curve represents the effect of Fe solute atoms on resistivity. The y-intercept at 1.75 $\mu\Omega$-cm represents the resistivity of pure copper. For comparison, both the three component (open symbols) and constrained two component (closed symbols) Gaussian-distributed Lorentzian fitting results for class I spectra have been plotted in the figure. Error bars representing the combined uncertainties in the γ_0 area fraction and the measured total Fe concentration in the alloy are indicated in the figure, except in the case of class II spectra because of their extremely poor resolution. The uncertainties associated with the resistivity values were given in Table IV-8; most are about 1%.

Comparison of the experimental data of Figure IV-13 with the extrapolated residual resistivity curve provides an estimate of the excess resistivity which can not be accounted for by the iron in solid solution with copper. In the two samples where large precipitate

---

*The abscissa values obtained from the two fitting models represent approximate upper and lower limits to the concentration of Fe in the γ_0 phase for sampes exhibiting class I spectra.

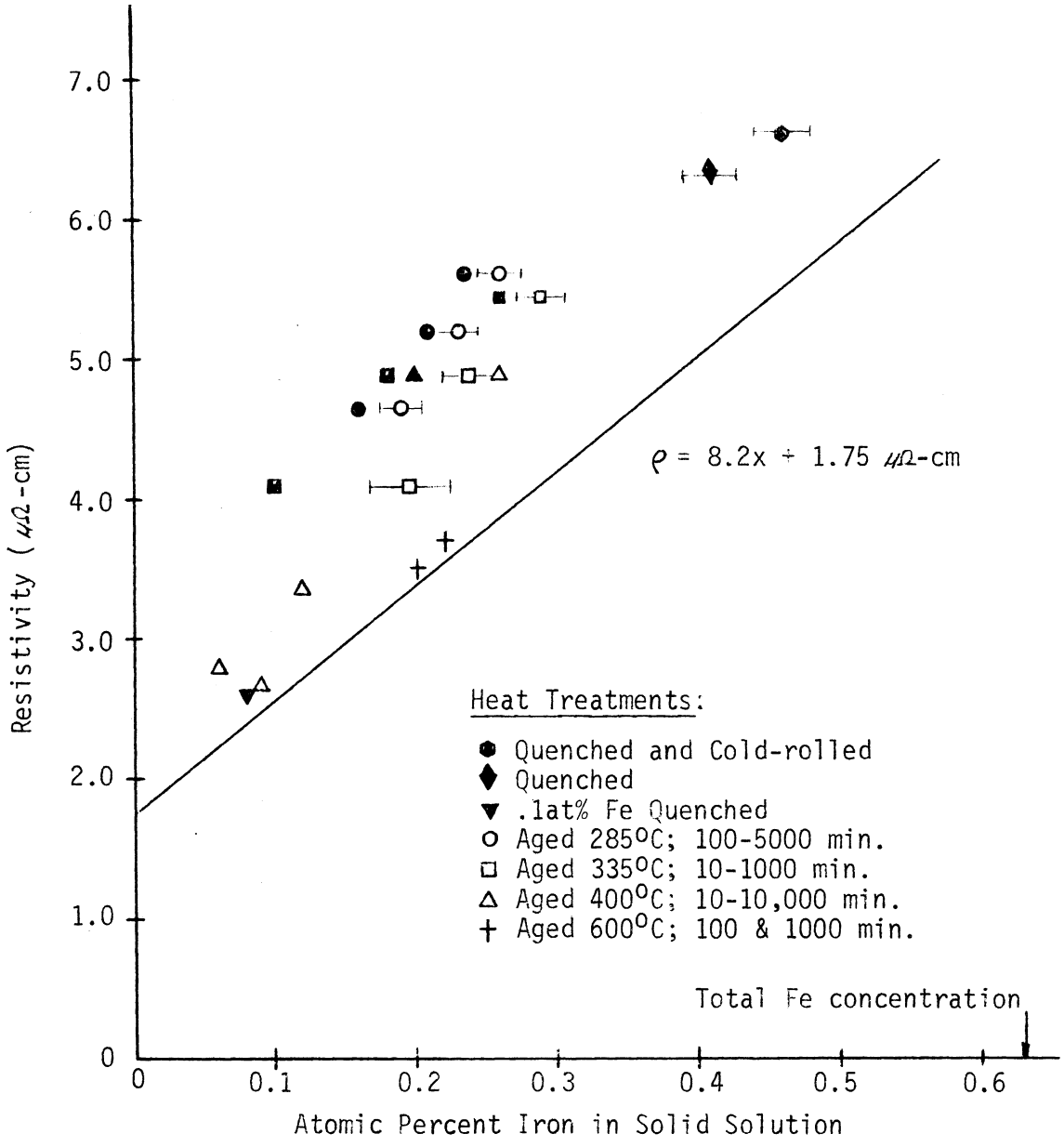

Figure IV-13.--Plot of resistivity versus atomic percent Fe in solid solution determined from Mössbauer spectra of heat treated copper-rich Cu-Fe alloys.

particles (>100A) are known to have formed (the 600°C-aging results designated by a cross), the resistivity values essentially fall on the extrapolated line. This indicates that in these cases only the Fe solute atoms remaining in solution with copper are effective in scattering electrons, and not the large precipitates. The resistivity of the 0.1% Fe quenched sample is also close to the extrapolated curve since very little clustering (as determined from the γ_2 component in its ME spectrum) has occured. On the other hand, deviations from the curve were significant for both the quenched and mildly aged (low temperature) Cu-0.6at%Fe alloy samples. In such cases, there exists an excess resistivity, $\Delta\rho$, which can be associated with the Fe clusters.*

The effectiveness of Fe clusters or precipitates in scattering electrons (i.e., their effective contribution to the resistivity) can be determined from Figure IV-13 as a function of heat treatment. Since the difference Δc, between the data points and the extrapolated curve represents the Fe solute concentration required to account for the excess resistivity, the relative effectiveness of the clusters may be defined as

$$\epsilon = \Delta c / c_2 \qquad \text{(IV.2)}$$

where c_2 is the overall concentration of Fe in clusters or small precipitates as determined from the Mössbauer spectra (i.e., γ_1 and γ_2). Values of ϵ are given in the following table for both quenched and aged samples.

---

*Other factors such as vacancies and strain fields associated with dislocations can cause anomolous electron scattering and thereby contribute to $\Delta\rho$. However, these effects should be small compared to the effect of Fe clusters (e.g., a $\Delta\rho$ of only 0.04 $\mu\Omega$-cm occurs when pure copper is cold-worked to an 87% reduction in area[137]).

Sample	ϵ	Sample	ϵ
Quenched & Rolled	.76	335°C - 1000 min.	.21
Quenched	.66	400°C - 10 min.	.38
285°C - 100 min.	.59	400°C - 100 min.	.15
285°C - 1000 min.	.52	400°C - 1000 min.	.11
285°C - 5000 min.	.39	400°C - 10,000 min.	.06
335°C - 10 min.	.49	600°C - 200 min.	.05
335°C - 100 min.	.38	600°C - 1000 min.	.03

The effectiveness parameter ϵ should decrease with increasing cluster size or with time at a given annealing temperature as indicated in the above table. For samples containing larger precipitates (600°C - 1000 min. and 400°C - 10,000 min.) ϵ approaches zero, in which case resistivity would be a direct measure of changes in the Fe concentration in solid solution. On the other hand, at the lower aging temperatures the large values obtained for ϵ indicate that resistivity would not be a good indicator of the concentration of Fe atoms in solid solution. This applies to most of the samples aged in the temperature range 285° - 400°C.

c. Low Temperature Aging: Growth of γ-Precipitates.--With regard to precipitate growth during the early stages of aging, Boltax[3] concluded that precipitation in Cu-Fe alloys probably occurs at dislocations formed during the pre-anneal quench from solution temperature. In this case, the precipitates would probably form as plates or disks on the dislocations. As mentioned in Section II.C, he based this conclusion on the isothermal kinetic behavior of the transformation fraction f (Equation IV.1) obtained from resistivity measurements. As will be discussed below, the Mössbauer results of Window[10] and this study do not support Boltax's suggested growth mechanism.

In order to make a direct comparison with his work, the resistivity results of the present study (Table IV-8) have been analyzed

in the manner of Boltax;[3] i.e., by application of the generalized rate equation

$$\frac{df}{dt} = K\,(1 - f)\,t^{n-1} \qquad \text{(IV.3)}$$

In the above expression, f is the fraction transformed given by Equation (IV.1), $K = A \exp(-nQ_R/RT)$ the rate constant, n the time exponent, and Q_R the activation energy. The f values versus aging time from the resistivity measurements were plotted in Figure IV-8 (solid curves). The log(t) at constant f values versus reciprocal temperature produced linear plots from which the activation energy Q_R was found to be about 37 kcal/mole (1.6 ev/atom). Plotting the function $\log(\log(\frac{1}{1-f}))$ versus log(t) (i.e., from the solution of Eq. IV.3) yielded a time constant of $n \sim .30$. Both values agree to within limits of experimental error with the results obtained by Boltax,[3] suggesting that identical growth processes occured in the alloys considered by the two studies. Since the resistivity data fails to directly account for Fe in small clusters which predominate at the lower aging termperatures, the resistivity derived kinetics results are not characteristic of the initial growth kinetics of Fe precipitates in copper. The combined effects of small clusters and isolated Fe atoms on resistivity are inseparable, making these kinetic parameters meaningless. This points up the general problem of trying to interpret microscopic properties through the use of bulk measurement techniques.

Because of the limited number of data points and the very poor resolution of the class II spectra, it is not possible to perform an analysis of the kinetics of Fe cluster formation and growth based on ME spectral data.* However, it does appear that the ME transformation

curves in Figure IV-8 (dashed lines) are not of the general sigmoidal shape characteristic of nucleation and growth reactions. As discussed below, the initial clustering of iron in the temperature range 285°C - 400°C, as characterized by Mössbauer spectroscopy, is instead suggestive of Guinier - Preston (G.P.) zone formation.**

G. P. zones are generally found in alloys where the difference in the atomic diameters of the solvent and solute atoms is small or where the supersaturation is large. Iron in copper satisfies both of these conditions. Its solubility in Cu at 600°C is about 0.2% (this study) and at 400°C and below is less than .05% (extrapolated from the high temperature portion of the solvus given in the phase diagram[77]). In addition, the room temperature lattice parameters of copper[139] and γ-iron[78] are 3.607 Å and 3.590 Å, respectively, the difference being only 0.5%.

Since G. P. zones in general, and Fe clusters in Cu-Fe in particular, tend to form at rates faster than would be expected from the lattice diffusion coefficient,*** their formation at low temperatures is very likely the result of excess vacancies quenched in during the solution treatment.[141] The enhanced diffusion occuring at low aging

---

*It is possible to estimate the activation energy for the clustering process from the ME transformation curves of Fig. IV-8. During the initial stage of Fe clustering, the three component G-L fitting results yield an activation energy of approximately 1.1 ev/atom (or ~26 kacal/mole).

**A general review of the properties and structure of Guinier-Preston zones or coherent clusters may be found in Christian.(138) In general, G.P. zones are a pre-precipitate phase in the form of solute-rich clusters that are coherent with the solvent's lattice.

***The lattice diffusion coefficient as a function of temperature is given by $D = D_0 \exp(-Q/RT)$. Using the values of $D_0 \sim 1.0$ cm^2/sec and $Q \sim 51.8$ kcal/mole obtained for Fe diffusion in copper at high

temperatures in the Cu-Fe system then would be due to the movement of the excess vacancies to grain boundaries and other vacancy sinks. The low activation energy estimated from the initial portion of the ME transformation curves is comparable to that for vacancy migration and not lattice diffusion. This is consistent with the excess vacancy mechanism of G.P. zone formation.

The difficulty with the excess vacancy hypothesis is that the lifetime of a vacancy is very short compared to the observed aging periods in alloys having G.P. zones. Hart[142] suggests that vacancies are retained for longer periods because of a strong attractive force between vacancies and solute atoms. The growth model proposed by Hart has vacancy and solute atom clusters migrating through the solvent's lattice picking up excess solute atoms along the way. Unfortunately an exact theoretical growth model for G.P. zones does not exist. However, the experimental evidence available on G.P. zone formation in alloys has been consistent with the proposed vacancy mechanism.[138]

The small atomic size misfit of Fe in Cu as well as the electron microscopy results of Easterling[134] for alloys with resolvable γ-precipitates indicate that incipient G.P. zones or small Fe clusters formed in copper are spherical in shape. Window's[10] recent work on aging in a Cu-1.0at%Fe alloy treats precipitate growth in this manner. On the assumption of spherical growth, it is possible to determine the number of surface atoms (i.e., Fe atoms having fewer than 12 Fe nearest neighbors) as a function of cluster size. As pointed out by Window[10]

---

temperatures by Mullen,[140] the value of D at 335°C would be only of the order of $3(10)^{-19}$ cm^2/sec. This is much too small to account for the significant clustering occuring at these low temperatures.

the surface atoms on small Fe clusters in Cu are responsible for the behavior of the γ_2 doublet in aged alloys. The calculations of Appendix B indicate that the γ_2 doublet probably remains well-defined (although considerably broadened by the variety of configurations) for Fe^{57} with up to five Fe nearest neighbors. Thus, during the incipient stage of clustering the Mössbauer spectra would be characteristic of Fe surface atoms in clusters (those having both Cu and Fe nearest neighbors) and Fe atoms in solid solution. To illustrate the role of surface atoms in small spherical clusters, the number of Fe nearest neighbors (n.n.) of iron atoms located in the first six shells about a central atom have been determined as a function of the number of filled shells. (The atoms were built on the FCC lattice in a spherical array through seven near neighbor shells.) The results are given in the table below.

# Fe Atoms in Shell		1	12	6	24	12	24	8
Shell Number		0	1	2	3	4	5	6
Filled Shells	1	12	5	4	2	1	0	0
	2	12	7	6	3	1	2	0
	3	12	11	8	5	5	4	3
	4	12	12	8	7	5	5	3
	5	12	12	12	9	7	7	3
	6	12	12	12	10	7	7	3
	7	12	12	12	12	11	9	9

As can be seen from the table, surface atoms having less than 12 Fe nearest neighbors predominate throughout the build up of the first six near neighbor shells. For example, with the first three shells filled there would be 24 Fe atoms with 5 Fe n.n., 6 with 8, 12 with 11 and only one with 12. Therefore, not until about six to seven shells are filled (clusters greater than $\sim$100 atoms) would one expect the γ_1 line due to γ-iron to be the predominant member of the γ_L (γ_2 + γ_1) component. As discussed previously in this section, this is believed to occur for samples aged at 400^{o}C for times greater than 100 minutes.

If the ratio of γ_1 to γ_2 Fe atoms could be accurately determined from the Mössbauer spectral areas, then an estimate of cluster size could be made from the preceding table. Unfortunately, the superposition of γ_1 and γ_2^L as well as the successively increasing overlap of the γ_0 and γ_2^R components renders this virtually impossible. However, by making use of the earlier discussion on spectra systematics (Section C.1) and Window's electric field gradient model (Appendix B), it is possible to make certain generalizations concerning Fe cluster size in aged Cu-.6%Fe alloys:

(1) The majority of clusters formed in samples aged at 285^{o}C and for short times (t<100 min.) at 335^{o}C most likely consist of fewer than 13 atoms. The ME spectra of these samples (Tables IV-4 and IV-5) retain a well defined γ_2 doublet with minimal traces of γ_1, indicating that Fe surface atoms predominate. Although the three component G-L fits indicate the possible presence of some γ_1-iron (3 to 7 % of the total Fe atoms in clusters), Window's[10] two component G-L model fits the data almost as well. Thus, very little if any γ_1-iron (i.e., Fe with completed Fe n.n. shell) has been formed in these

samples.

(2) In the samples aged for t>100 min. at 335^{o}C and for t<100 min. at 400^{o}C, the spectral components associated with Fe clustering are still predominately due to Fe atoms with less than a full shell (12) of iron nearest neighbors. The three component G-L fits indicate that possibly 20 - 30% of the clustered iron atoms have either a full shell or very close to a full shell of Fe nearest neighbors. A nearest neighbor shell of 10 or 11 Fe atoms would be expected to produce a quadrupole-broadened resonance line shifted slighly to higher velocities from the true γ_1 or γ-iron line. This might be the cause of the shift and broadening occuring in γ_L for these samples. If so, then the size of the clusters could extend to approximately three near neighbor shells ($\sim$43 atoms). On the other hand, the observed broadening and shift in the γ_L component could be the result of configurational and size variations in smaller clusters, in which case γ_L would be mainly comprised of the left member of the γ_2 doublet. This possibility can not be precluded since the two component G-L fitting model produced adequate fits to the data.

(3) The spectra of samples aged at 400^{o}C for t $\geq$ 100 minutes show definite signs of γ_1-iron formation; i.e., the γ_L component in either the two or three G-L line fits (Table IV-6) exhibited position and width characteristics similar to the dominant γ-iron line produced in the 600^{o}C - aged samples. On the basis of the n.n. configurations given in the preceding table, these clusters are very likely larger than six or seven n.n. shells in radius (i.e.,> 6.2 Å). In the case of the 400^{o}C - $(10)^4$ min. sample, it is possible to make a very crude estimation of the particle size as follows. The ratio of volume to

surface atoms can be approximated as

$$\frac{A_1 + A_2}{A_2} \cong \frac{4\pi R^3/3}{4\pi R^2 \Delta R} = R/3\Delta R$$

where A_1 and A_2 are spectral areas for γ_1- and γ_2-iron, respectively, and ΔR is the surface shell thickness (taken as the nearest neighbor spacing -- 2.47 Å). Using the results of Table IV-6, the above expression gives R~20 Å for the average precipitate radius in this alloy.

It is worthwhile to make a comparison between the very approximate Fe cluster sizes inferred from the Mössbauer data of Cu-.6%Fe with those found in the analogous Cu-Co system. (As discussed in Section II-D, the Co precipitate particles in Cu-Co are superparamagnetic which allows their sizes to be determined from magnetization measurements.) In the Cu-rich system the Co precipitates are coherent forming homogeneously in the Cu matrix, and are believed to be roughly spherical in shape.[105] In a Cu-2.0wt%Co alloy, Piercy[50] found precipitate particles of about 13 Å in radius upon aging at 395°C ($3 \lesssim t \lesssim 428$ hr.). This value falls within the size range estimated above for Cu-0.6%Fe aged at 400°C ($1.6 \lesssim t \lesssim 166$ hr.). Comparable precipitates are also found in the two systems after aging at 600°C. The similarity in the shape and sizes of the precipitates in the two alloy systems is not surprising considering the similarity of the Cu-rich ends of their respective phase diagrams.

According to the foregoing arguments, the range of precipitate or cluster sizes inferred from room temperature ME spectra using the three component G-L fitting scheme described in Section IV-B is somewhat larger than proposed by Window[10] in a recent Mössbauer study of

aging and cold-working in Cu-1.0%Fe. In that study, Window concluded that aging at temperatures of 300° to 400°C ($t \lesssim 180$ min.) produces Fe clusters with sizes less than 13 atoms. The room temperature spectra of the class I type (Figure IV-3) were fit to the sum of an area constrained G-L doublet representing γ_2-iron and a G-L singlet representing γ_0, thereby precluding any γ_1 contribution to the spectra. Window's estimation of cluster size was based on an interpretation of the magnetic field distributions, p(H) curves, derived from fitting the low temperature (4.2°K) hfs spectra of the aged alloys.

The effective fields at the iron sites in Fe clusters in Cu are believed to be due to localized moments on atoms in the nearest neighbor shell with the contributions from more distant neighbors leading to perturbations and broadening in the hyperfine field distributions. The unfolding of the extremely complex spectra associated with these fields is very difficult and in the case of Window,[76] was accomplished by using a synthesis of cosine functions to simulate the field distributions resulting from a variety of Fe cluster sizes and configurations. As a further approximation, quadrupole and isomer shift effects were neglected. The magnetic field distributions so obtained from the spectra of aged Cu-Fe alloys revealed that in small clusters the individual spins tend to align parallel producing a very broad p(H) distribution with some structure. Window [8][10] was able to associate a definite peak at ~80 kOe with Fe atoms having no Fe nearest neighbors and a very broad distribution at larger H with those in small clusters. Large clusters or precipitates of γ-iron, on the other hand, are known to behave antiferromagnetically (Abrahams et al.[142]). The critical cluster size for which antiferromagnetic ordering sets in is

not known. The Mössbauer spectrum of γ-iron precipitates below the Neél temperature* consists of a broadened resonance line containing unresolved hf structure characterized by a small effective field of ~20 kOe.[70] It was the absence of a low field peak in the p(H) distributions of moderately aged alloys which led Window to conclude that virtually no γ_1-iron (Fe with a completed n.n. shell of iron atoms) exists in clusters formed at low aging temperatures.

In contrast this study's room temperature spectra of Cu-0.6%Fe samples aged at 400°C for $t \geq 100$ minutes show substantial evidence of γ_1 formation. The analogy between the Cu-rich Cu-Fe and Cu-Co alloy systems lends further support for γ_1-iron formation at 400°C. The apparent discrepancy between the 300°K and 4.2°K spectra could be caused by differences in the effective contributions of neighbors outside the nearest neighbor shell to the three hyperfine interactions at an Fe^{57} site in a cluster. In the case of magnetic effects, this would include the influence of near neighbors on the type of order observed (e.g., in small precipitates, the relatively large number of surface atoms would influence the spins of internal or γ_1-iron atoms). For Fe clusters in Cu, the influence of neighbors outside the n.n. shell on the s-electron density and the electric field gradient of the resonant atom is probably much less than their magnetic ordering effects. This would explain the appearance of the apparent γ-iron component in the room temperature spectra but not in the 4.2°K spectra.

---

*The Neél temperature in Cu-rich Cu-Fe alloys appears to be dependent upon aging temperature and time. (70) This is probably caused by its dependence on particle size of the precipitate.

3. Summary

Mössbauer spectroscopy (at room temperature) was able to follow in a qualitative manner the early growth of coherent iron clusters in a copper-rich Cu-Fe alloy during the incipient stages of aging. The distribution of isomer shifts and quadrupole splittings associated with configurational variations of Fe in three different environments (Fe with only Cu nearest neighbors - γ_0, Fe with only Fe nearest neighbors - γ_1, and Fe with both Cu and Fe nearest neighbors - γ_2) were treated by using Gaussian-distributed Lorentzian functions to fit the complex spectra. Two fitting models were used: one consisting of three G-L singlets and the other consisting of one G-L singlet plus an area constrained G-L doublet (Window[10]).

Phase identification as well as the quantitative determination of iron concentrations could be unambiguously made in the cases of solution treated samples (contained predominantly γ_0 with some γ_2) and samples aged at 600°C (contained predominately γ_1 with some γ_0 and trace amounts of γ_2). In the case of samples aged at intermediate temperatures, poor spectral resolution resulting from excessive overlap of the spectral components prevented an exact quantitative determination of iron phase concentrations. However, upper and lower bounds to the phase concentrations were established through the application of the two G-L fitting schemes. Quantitative phase analysis was also performed on aged and cold-rolled samples containing both γ- and α-iron.

The Mössbauer results are consistent with the formation of spherical Guinier-Preston zones or pre-precipitates during the early stages of aging. The predominance of the broadened doublet component due to γ_2-iron in the spectra of samples aged at 400°C ($t < 100$ min.)

and lower temperatures indicates that the clusters formed consist of very few Fe atoms -- possibly up to three near neighbor shells at most. Aging for longer times at 400°C results in the formation of Fe clusters that are large enough ($\sim$5 or 6 near neighbor shells) to produce a significant γ-iron component in the 300°K Mössbauer spectra, while aging at 600°C is known to produce precipitates $\sim$100 Å in radius.[86] The results of the present study are in general agreement with those of Window's [10] recent work on aging in Cu-1.0at%Fe.

The Mössbauer results for copper-rich Cu-Fe alloys do not support the dislocation-enhanced growth mechanism suggested by Boltax[3] to explain the results of resistivity measurements in the same alloy system. Comparison of Mössbauer and resistivity results from both quenched and aged samples in the present study indicates that small Fe clusters significantly contribute to the alloy's residual resistivity, which was assumed by Boltax to be caused by isolated iron atoms only. It is the effects of very small Fe clusters, undetected in the resistivity measurements, which are responsible for the discrepancies in the results from the two measurement techniques. Mössbauer spectroscopy has the advantage of being able to detect small Fe clusters during the early stages of aging.

D. Results of Irradiation Experiments

The majority of the Cu-Fe alloy samples which were thermally treated in the manner described in Section IV-B were subsequently irradiated in the FNR at three different integrated fast fluxes. The results of these irradiations are described below.*

1. Solution Annealed and Quenched Samples

Table IV-10 summarizes the effects of fast neutron exposure on the ME spectral parameters of solution treated and cold-rolled Cu-Fe alloy samples. Parameter values are listed for both pre- and post-irradiation conditions. Initially, spectra from all of the quenched - irradiated samples were fit to the sum of three unconstrained Lorentzians. For the reasons given in Section IV-B, many were re-analyzed using the Gaussian-distributed Lorentzian (G-L) fitting model described in Section III-D. Representative Mössbauer spectra of quenched and cold-rolled Cu-0.6at%Fe samples in the pre-irradiated (fit with a G-L singlet and area constrained doublet) and post-irradiated (fit with three G-L singlets) conditions are displayed in Figure IV-14.

Comparison of Tables IV-4 and IV-10 as well as Figures IV-6 and IV-14 reveals that fast neutron irradiation produces similar effects on the Mössbauer spectra of solution treated alloys as thermal aging; e.g., the increase in the area fractions of γ_2^R and γ_L ($\gamma_1 + \gamma_2^L$), the significant broadening of γ_2^R, and the slight positional shifts in γ_2^R (negative) and γ_L (positive). These spectral changes signify that iron clustering has occured (see Section IV-C.1) and are direct evidence of irradiation-induced aging. The changes in spectral parameters are even more pronounced when the constrained two component G-L fitting model is applied to the post-irradiation spectra. For comparison, the results from the two fitting methods are listed in the

---

*Following irradiation many of the thin Cu-Fe foils contained pin holes and small tears. As a result, meaningful resistivity measurements were able to be performed on only a few of the post-irradiated samples.

TABLE IV-10

EFFECTS OF FAST NEUTRON IRRADIATION ON THE MÖSSBAUER SPECTRA OF QUENCHED Cu-Fe ALLOYS

Sample[c]		Position[a] (mm/sec)			Line Width[b] (mm/sec)			Relative Area			χ^2/N
		$\gamma_2^L + \gamma_1$	γ_o	γ_2^R	$\gamma_2^L + \gamma_1$	γ_o	γ_2^R	$\gamma_2^L + \gamma_1$	γ_o	γ_2^R	
(1) Fast neutron fluence $\phi t \sim 4(10)^{18}$ n/cm^2:											
Quenched & Rolled (G-L fits)	b	.157(4)	.481(4)	.741(4)	.075(3)	.060(2)	.074(3)	.163(3)	.674(4)	.163(3)	1.02
	a	.166(4)	.482(4)	.738(5)	.073(3)	.054(1)	.088(4)	.218(2)	.583(1)	.199(4)	1.11
Quenched (Lorentzian fits)	b	.158(4)	.484(4)	.744(5)	.231(3)	.244(5)	.251(8)	.184(6)	.632(9)	.184(6)	1.15
	a	.165(4)	.485(4)	.729(6)	.246(4)	.254(6)	.285(7)	.228(4)	.566(5)	.206(7)	1.21
(2) Fast neutron fluence $\phi t \sim 2.7(10)^{19}$ n/cm^2:											
.2% Fe "Q" (G-L fits)	b	.164(4)	.483(4)	.738(4)	.066(2)	.038(2)	.085(3)	.158(3)	.683(4)	.158(3)	1.04
	a	.175(4)	.483(4)	.722(5)	.072(2)	.042(3)	.100(4)	.242(2)	.553(3)	.206(5)	1.12
Quenched (G-L fits)	b	.170(4)	.484(4)	.738(6)	.065(2)	.048(3)	.092(4)	.199(4)	.602(2)	.199(4)	1.11
	a	.174(4)	.486(4)	.728(6)	.067(2)	.055(3)	.096(4)	.274(2)	.495(2)	.230(6)	1.20
Quenched & Rolled (Lorentzian fits)	b	.152(4)	.480(4)	.742(5)	.234(2)	.265(2)	.249(4)	.138(4)	.723(7)	.138(4)	1.03
	a	.164(4)	.482(4)	.730(5)	.260(4)	.266(4)	.271(6)	.239(6)	.58(1)	.183(9)	1.38

TABLE IV-10 (continued)

EFFECTS OF FAST NEUTRON IRRADIATION ON THE MÖSSBAUER SPECTRA
OF QUENCHED Cu-Fe ALLOYS

Sample		Position[a] (mm/sec)			Line Width[b] (mm/sec)			Relative Area			χ^2/N
		$\gamma_2^L + \gamma_1$	γ_o	γ_2^R	$\gamma_2^L + \gamma_1$	γ_o	γ_2^R	$\gamma_2^L + \gamma_1$	γ_o	γ_2^R	
(3) Fast neutron fluence $\phi t \sim 9(10)^{19}$ n/cm^2:											
.1% Fe "Q" (Lorentzian fits)	b	.155(4)	.483(4)	.743(4)	.231(2)	.229(1)	.244(3)	.109(3)	.782(2)	.109(3)	0.99
	a	.168(4)	.486(4)	.714(5)	.240(3)	.236(2)	.276(5)	.216(3)	.601(3)	.183(7)	1.14
Quenched (G-L fits)	b	.165(4)	.483(4)	.736(5)	.063(2)	.044(2)	.096(3)	.20(1)	.600(5)	.20(1)	1.02
	a	.178(4)	.485(4)	.704(6)	.077(2)	.057(3)	.112(5)	.313(2)	.434(4)	.254(9)	0.96
Quenched & Rolled (G-L fits)	b	.165(4)	.482(4)	.737(5)	.077(2)	.061(2)	.073(2)	.166(3)	.667(4)	.166(3)	0.97
	a	.173(4)	.482(4)	.705(6)	.078(2)	.049(3)	.116(5)	.292(2)	.471(3)	.237(9)	0.98

[a] Position referred to SNP

[b] Lorentzian fit: FWHM Γ; Gaussian-distributed Lorentzian fit: width of Gaussian broadening θ

[c] b = before; a = after irradiation

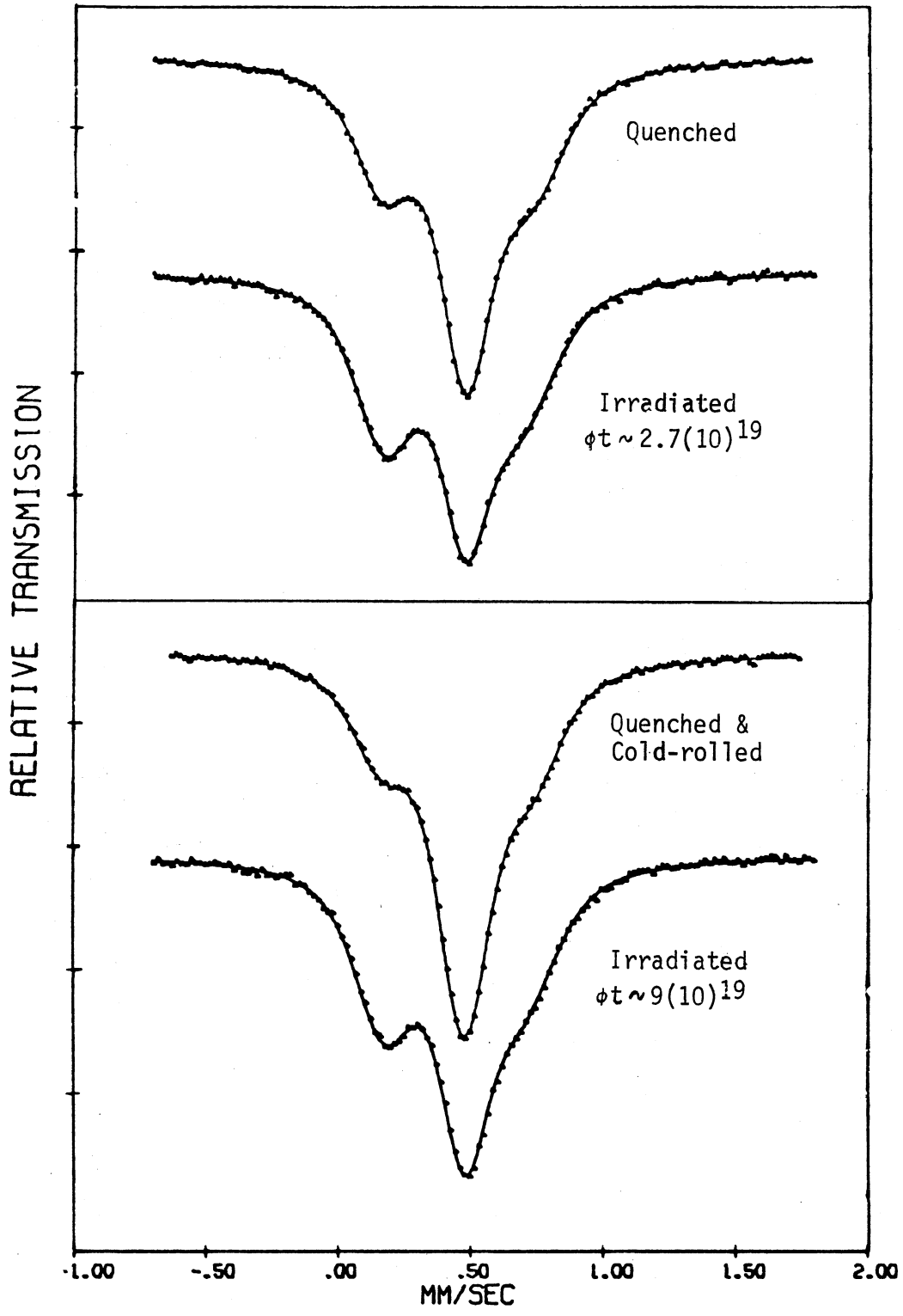

Figure IV-14.--Effects of fast neutron exposure on spectra of solution treated and cold-rolled Cu-0.6at%Fe alloy samples.

table immediately below for a quenched Cu-0.6%Fe alloy irradiated to a fast fluence of~$9(10)^{19}$ n/cm^2. (For reference, spectral parameters of the quenched alloy are also given.)

	P_L	P_o	P_R	θ_L	θ_o	θ_R	A_L	A_o	A_R	χ^2/N
(a) Quench	.165	.483	.736	.063	.044	.096	.200	.600	.200	1.02
(b) 3 G-L	.178	.485	.704	.077	.057	.112	.313	.434	.254	0.96
(c) 2 G-L	.178	.481	.676	.078	.025	.147	.313	.374	.313	1.05

Here, P represents the components' isomer shift with respect to SNP, θ the Gaussian broadening parameter, and A the area fraction. The subscript "o" refers to γ_o-iron, while "L" and "R" refer to the left ($\gamma_1 + \gamma_2^L$ for 'b' and γ_2^L for 'a' and 'c') and right (γ_2^R) components, respectively. As discussed previously for thermal aging, the γ_o area fractions from the two fitting schemes represent upper (three component model) and lower (two component model) bounds to the fraction of Fe atoms with a complete Cu nearest neighbor shell. A previous comparison of the fitting schemes also revealed that the spectral parameters for γ_L (left-most component) in the case of class I spectra remained relatively insensitive to the fitting model used. This is also apparent in the above table for the irradiated samples.

It was shown in Section IV-C that the area fraction of the γ_L component represents the most reliable indicator of iron cluster formation (i.e., it is only representative of Fe atoms in a cluster configuration). Therefore, in Figure IV-15 the irradiation-induced change in the γ_L area fraction (converted to Fe concentration) for solution treated samples has been plotted versus the initial or pre-irradiation concentration of Fe in solid solution (γ_o). Data from alloy samples containing 0.1 and 0.2 at% Fe as well as from 0.6%Fe-samples which had been cold-rolled following solution treatment are also

plotted to indicate the strong dependence of irradiation-induced clustering on the degree of supersaturation. The ordinate values, in the case of the two component model, represent one-half the concentration of Fe atoms that have left the solid solution phase to form small clusters.

Resistivity measurements were successfully performed on two of the quenched samples which were irradiated at fluences of $2.7(10)^{19}$ and $9(10)^{19}$ n/cm^2. Changes in resistivity ($\Delta\rho$) between the pre- and post-irradiated samples are given in the table below.

Fluence	$\Delta\rho$($\mu\Omega$-cm)	ΔC_ρ	ΔC_M(3 G-L)	ΔC_M(2 G-L)
$2.7(10)^{19}$ n/cm^2	-.44	-.054	-.067(5)	-.102(8)
$9(10)^{19}$ n/cm^2	-.77	-.094	-.104(8)	-.14(1)

Also included in this table are the associated concentration changes in solid solution Fe (ΔC_ρ) derived from the $\Delta\rho$ values, along with the corresponding concentration changes (ΔC_M) derived from the γ_0 area fractions of the Mössbauer spectra. (Concentration values are reported in atom% Fe.) The ΔC_ρ values in the above table were obtained using the slope (8.21 $\mu\Omega$-cm/at% Fe) of the electrical resistivity versus Fe concentration curve of Figure IV-13, while the ΔC_M values were obtained using the procedure described in Section II-A. The results of both measurement techniques show that the concentration of iron in the solid solution phase of quenched alloys decreases significantly following fast neutron irradiation.

2. Aged Samples

The results of the fast neutron irradiation studies of aged alloys using Mössbauer spectroscopy are summarized in Tables IV-11

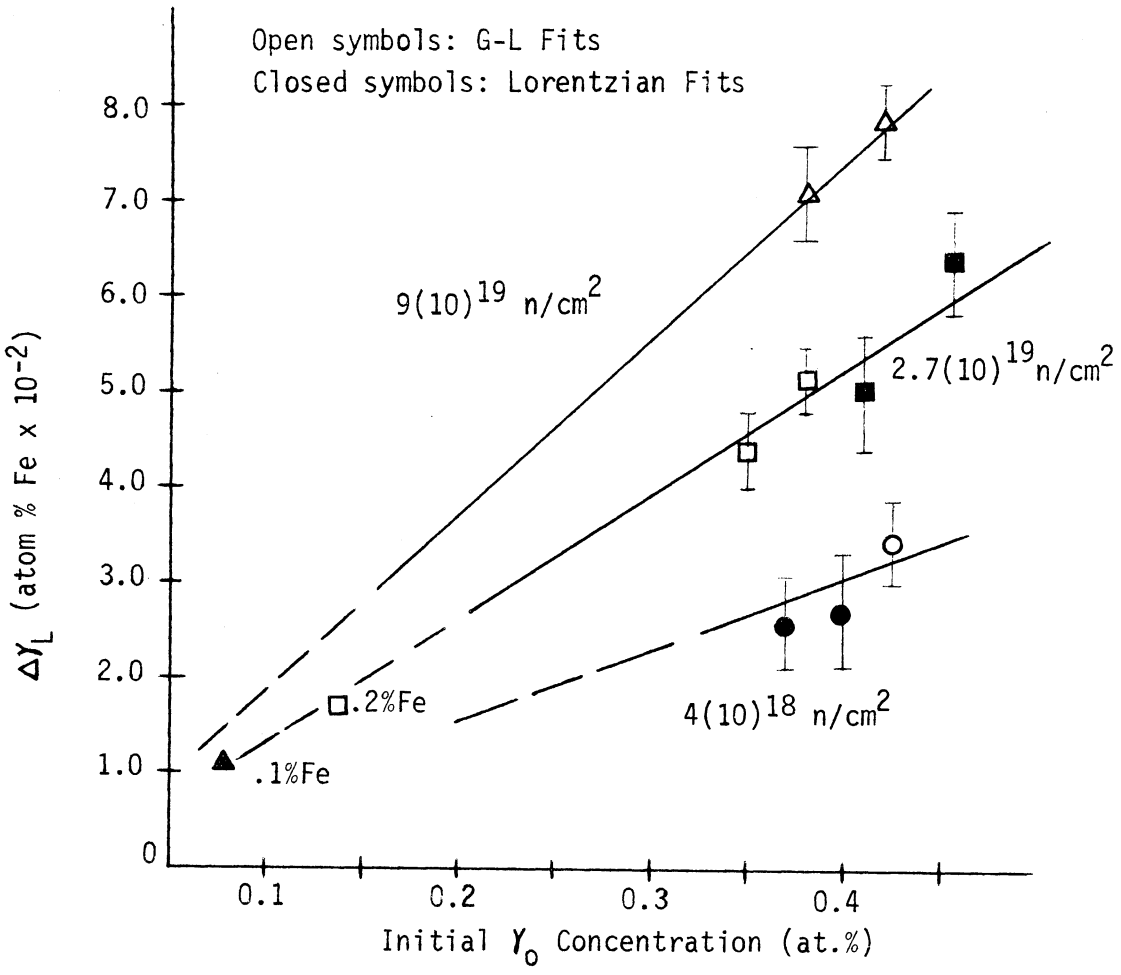

Figure IV-15.--Irradiation-induced change in the γ_L spectral component (atom % Fe) versus pre-irradiated concentration of iron in solid solution for solution treated Cu-Fe alloys.

through IV-16 and Figures IV-16 through IV-18. For comparison, spectral parameters for both pre- and post-irradiation conditions have been included in the tables. The spectra associated with the irradiated samples are categorized in the manner of Section IV-B; i.e., into three classes according to their appearance. These classes as applied to both aged and irradiated samples are representative of the various stages of iron precipitation in Cu: class I (broadened, apparent three line spectra) of incipient Fe cluster formation; class II (broadened, apparent two line spectra) of an intermediate stage of cluster formation; and class III (three relatively narrow resonance lines) of large iron precipitate formation. The exposure of aged Cu-Fe samples to fast neutrons caused subtle, but significant changes in their Mössbauer spectra which can be interpreted in terms of either increases or decreases of Fe in cluster form. The spectral changes due to irradiation are evaluated below on the basis of the knowledge gained from the previous detailed study of aged alloys.

The majority of the Cu-0.6at%Fe samples were irradiated to a fast neutron exposure of approximately $2.7(10)^{19}$ n/cm^2; however, many of the samples were also irradiated to fluences of $4.0(10)^{18}$ and $9(10)^{19}$ n/cm^2. The effects of an exposure of $2.7(10)^{19}$ n/cm^2 on the Mössbauer spectral parameters of moderately aged alloy samples (class I spectra) are shown in Table IV-11. Like their aged counterparts, these spectra were fit to the sum of three G-L functions with the spectral components as defined previously (see Section IV-B). In the case of the 335^{o}C - samples, the spectra were also fit with the two component G-L model ($\gamma_0 + \gamma_2$); the resulting parameters are given in Table IV-12. Comparison of the two tables indicates that the

TABLE IV-11

THREE G-L COMPONENT SPECTRA PARAMETERS FOR HEAT TREATED Cu-0.6% Fe ALLOY SAMPLES BEFORE AND AFTER FAST NEUTRON EXPOSURE OF ~2.7(10)^{19} n/cm^2

Heat Treatment		Position (mm/sec.)			Gaussian Width (mm/sec.)			Relative Area			χ^2/N
		$\gamma_2^L + \gamma_1$	γ_o	γ_2^R	$\gamma_2^L + \gamma_1$	γ_o	γ_2^R	$\gamma_2^L + \gamma_1$	γ_o	γ_2^R	
Sol. anneal & quench	b	.158(4)	.484(4)	.739(5)	.065(2)	.042(2)	.089(4)	.189(4)	.633(4)	.178(6)	1.06
	a	.173(4)	.486(4)	.724(5)	.067(2)	.050(2)	.098(4)	.276(2)	.496(2)	.229(6)	1.14
285°C 100 min.	b	.178(4)	.485(4)	.703(6)	.066(2)	.053(2)	.112(4)	.310(1)	.421(3)	.269(7)	1.32
	a	.178(4)	.486(4)	.712(6)	.078(2)	.059(3)	.111(4)	.319(1)	.421(3)	.261(6)	1.30
285°C 1000 min.	b	.176(4)	.481(5)	.687(6)	.064(2)	.046(3)	.121(5)	.325(1)	.370(5)	.304(9)	1.38
	a	.178(4)	.484(5)	.699(6)	.077(2)	.051(3)	.116(4)	.330(2)	.390(5)	.28(1)	1.16
285°C 5000 min.	b	.187(4)	.487(6)	.63(1)	.069(3)	.065(10)	.141(1)	.374(3)	.30(2)	.33(1)	1.09
	a	.184(4)	.482(5)	.67(1)	.076(2)	.057(6)	.129(8)	.361(2)	.33(1)	.31(2)	1.08
335°C 10 min.	b	.171(4)	.485(4)	.712(6)	.061(2)	.041(3)	.102(5)	.283(2)	.470(3)	.248(6)	1.06
	a	.174(4)	.483(4)	.705(5)	.077(3)	.051(3)	.107(6)	.314(2)	.437(3)	.249(9)	1.13
335°C 100 min.	b	.191(5)	.487(5)	.661(9)	.078(2)	.061(4)	.12(1)	.356(2)	.39(1)	.26(2)	1.08
	a	.185(4)	.486(5)	.682(8)	.085(2)	.052(4)	.126(7)	.350(2)	.370(7)	.28(1)	0.97
335°C 1000 min.	b	.202(5)	.484(*)	.58(3)	.106(3)	.05(1)	.14(2)	.439(6)	.31(8)	.25(7)	1.34
	a	.186(4)	.484(*)	.63(1)	.096(2)	.047(5)	.150(9)	.410(4)	.27(2)	.32(2)	1.01
400°C 10 min.	b	.189(4)	.487(5)	.67(1)	.082(2)	.049(4)	.13(1)	.341(2)	.42(1)	.24(2)	0.98
	a	.181(4)	.484(5)	.678(9)	.089(3)	.048(5)	.135(9)	.363(3)	.380(9)	.26(2)	1.19

b = before; a = after

*Positions were constrained at 0.484 mm/sec., the isomer shift for solid solution Fe in copper during the fitting.

TABLE IV-12

TWO G-L COMPONENT SPECTRA PARAMETERS FOR AGED (335°C) Cu-0.6% Fe ALLOY SAMPLES BEFORE AND AFTER FAST NEUTRON EXPOSURE OF ~2.7(10)^{19} n/cm^2

Heat Treatment		Position (mm/sec.)		γ_2 Splitting	Gaussian Width (mm/Sec.)			Relative Area		χ^2/N
		γ_0	γ_2		γ_2^L	γ_0	γ_2^R	γ_0	γ_2	
Sol. Anneal & quench	b	.483(4)	.450(4)	.575(1)	.065(2)	.035(2)	.091(3)	.622(3)	.378(4)	1.11
	a	.484(4)	.434(5)	.515(1)	.067(2)	.038(3)	.129(4)	.448	.552(4)	1.17
335°C 10 min.	b	.480(4)	.430(4)	.509(1)	.062(2)	.027(3)	.132(3)	.425(3)	.575(5)	1.20
	a	.475(4)	.424(4)	.500(1)	.079(2)	.033(3)	.146(3)	.369(4)	.631(7)	1.31
335°C 100 min.	b	.483(4)	.405(5)	.428(2)	.078(2)	.045(3)	.155(3)	.290(3)	.710(6)	1.11
	a	.481(4)	.418(4)	.465(1)	.081(2)	.037(2)	.155(2)	.299(3)	.701(6)	1.03
335°C 1000 min.	b	.488(5)	.369(5)	.338(2)	.099(3)	.019(8)	.174(5)	.16(1)	.84(1)	1.46
	a	.485(4)	.390(4)	.414(2)	.093(2)	.024(7)	.173(3)	.198(4)	.802(6)	1.04

b = before; a = after

paramaeters associated with γ_L from the two fitting models agree within experimental error as was found previously for other class I samples.

Figure IV-16 illustrates the effects of increasing fast neutron exposure upon the spectra of samples aged at 335°C for 1000 minutes. The spectral parameters are listed in Table IV-13 for three different fluences. A cursory examination of the figure and table reveals that the spectra associated with increasing neutron exposure have reverted to forms characteristic of a less advanced stage of aging; i.e., they exhibit an increase in splitting between the right (γ_2^R) and left ($\gamma_1 + \gamma_2^L$) components as well as decrease in area fraction of γ_L. On the other hand, several samples aged for short times at temperatures of 285°-400°C showed characteristics (see Tables IV-11 and IV-12) of increased aging as also occured in solution treated alloys following irradiation. This distinctly opposite behavior is related to the stage of Fe clustering in the pre-irradiated alloy. Detailed interpretation of these phenomena is delayed until all of the results have been presented.

The effects of an exposure of $2.7(10)^{19}$ n/cm^2 on the 400°C-aged samples which exhibited class II spectra (Figure IV-5) are shown in Table IV-14. Both two and three line fits were made of the data. Although poor resolution prevents a detailed interpretation of the pre- and post-irradiation spectra, it is apparent from the decrease in the left component's area fraction (both fits) and the large increase in the broadening of γ_2 (3-line fit) or the right component (2-line fit) that irradiation-induced precipitate or cluster break-up has occured. This was not the case with those samples aged at 600°C

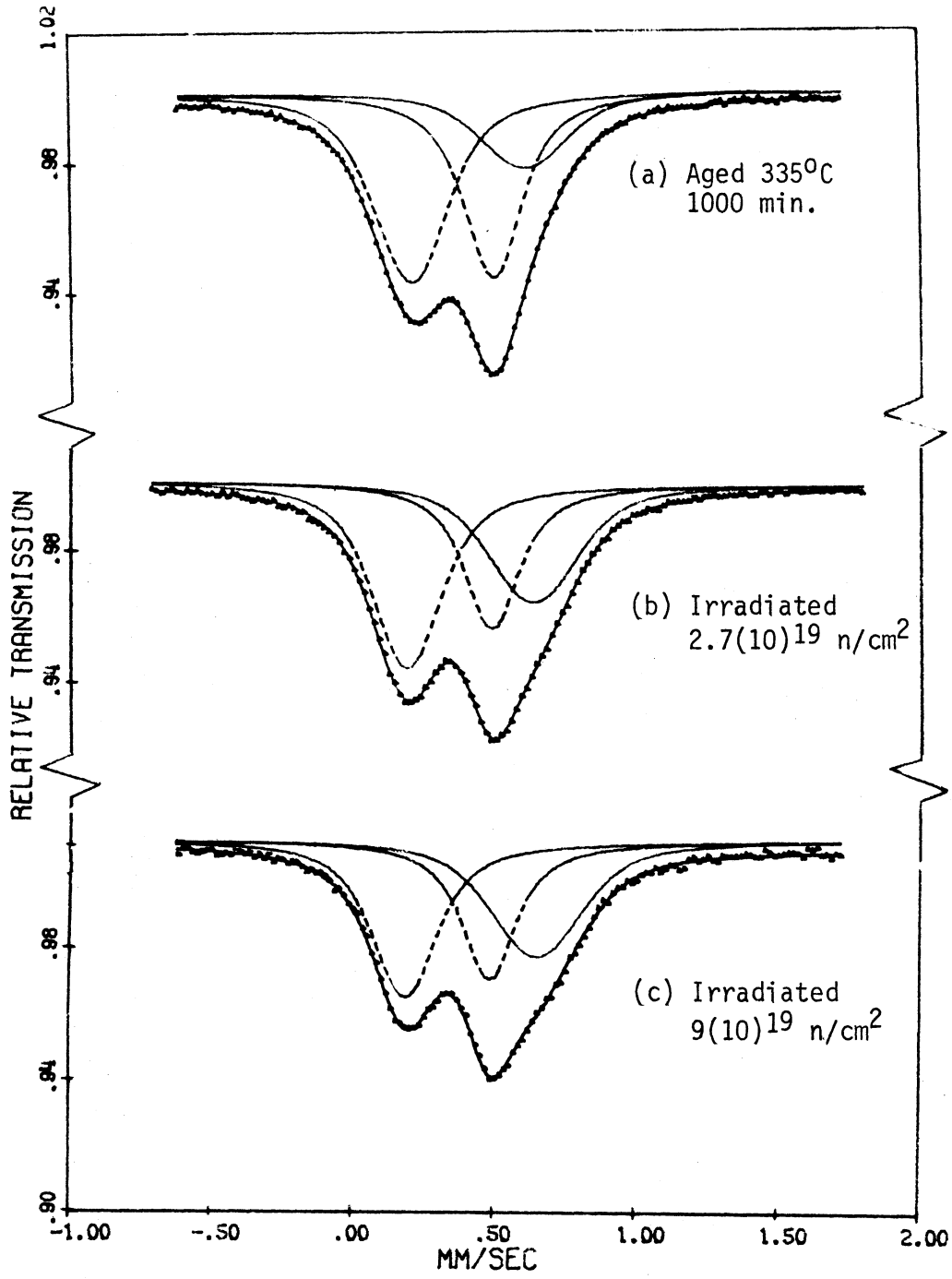

Figure IV-16.--Effects of increasing fast neutron exposure on the Mössbauer spectrum of Cu-0.6at%Fe aged at 335°C for 1000 minutes. The spectra were fit with three Gaussian-distributed Lorentzian functions.

TABLE IV-13

EFFECTS OF INCREASING FAST NEUTRON EXPOSURE ON MOSSBAUER SPECTRAL PARAMETERS FOR A Cu-0.6% Fe ALLOY AGED AT 335°C FOR 1000 MIN.[a]

Fast Neutron Exposure (n/cm^2)	Position (mm/sec)			Gaussian Width (mm/sec)			Relative Area			χ^2/N
	$\gamma_2^L + \gamma_1$	γ_o[b]	γ_2^R	$\gamma_2^L + \gamma_1$	γ_o	γ_2^R	$\gamma_2^L + \gamma_1$	γ_o	γ_2^R	
Aged Sample Before Irradiation	.202(5)	.484	.58(3)	.106(3)	.05(1)	.14(2)	.439(6)	.31(8)	.25(7)	1.34
$4.0(10)^{18}$ n/cm^2	.197(4)	.484	.60(1)	.095(3)	.045(8)	.155(12)	.42(1)	.29(9)	.29(6)	1.13
$2.7(10)^{19}$ n/cm^2	.186(4)	.484	.63(1)	.096(2)	.047(5)	.150(9)	.410(4)	.27(2)	.32(2)	1.01
$9.0(10)^{19}$ n/cm^2	.187(5)	.484	.65(1)	.080(2)	.039(5)	.153(8)	.367(3)	.28(2)	.35(1)	1.09

[a] Spectra were fit to the sum of three Gaussian-distributed Lorentzian functions.

[b] Constrained at the γ_o position for quenched samples.

TABLE IV-14

MÖSSBAUER SPECTRA PARAMETERS FOR Cu-0.6% Fe ALLOY SAMPLES AGED AT 400°C (CLASS II SPECTRA) BEFORE AND AFTER A FAST NEUTRON EXPOSURE OF ~2.5(10)^{19} n/cm^2

Sample		Position (mm/sec)			Line Width[c] (mm/sec)			Relative Area			χ^2/N
		γ_1	γ_o	γ_2	γ_1	γ_o	γ_2	γ_1	γ_o	γ_2	
					(1) 3-line fits:[a]						
400°C	b	.165(5)	.484	.41(1)	.067(4)	.21(1)	.22(1)	.35(1)	.17(3)	.48(1)	1.34
100 min.	b	.164(5)	.484	.44(1)	.071(4)	.23(1)	.26(1)	.32(1)	.21(2)	.47(1)	1.16
400°C	b	.160(5)	.484	.39(1)	.057(3)	.20(3)	.169(9)	.466(7)	.10(4)	.43(1)	1.28
1000 min	a	.158(5)	.484	.40(1)	.052(3)	.20(2)	.25(1)	.35(1)	.09(1)	.56(1)	1.11
					(2) 2-line fits:[b]						
		P(L)	P(R)		θ(L)	θ(R)		A(L)	A(R)		
400°C	b	.180(5)	.461(5)		.065(3)	.106(3)		.461(6)	.539(2)		3.10
100 min	a	.165(5)	.482(6)		.076(4)	.156		.407(7)	.593(5)		2.55
400°C	b	.175(5)	.437(5)		.069(2)	.116(3)		.548(5)	.452(2)		1.57
1000 min	a	.164(5)	.451(5)		.071(2)	.161(4)		.482(6)	.518(7)		2.55

b = before; a = after irradiation

[a] Data fit to the sum of two Gaussian-distributed Lorentzian functions plus a Lorentzian singlet constrained at .484 mm/sec representing γ_o.

[b] Data fit to the sum of two Gaussian-distributed Lorentzian functions (L = left; R = right).

[c] For the 3-line fits: γ_o line width reported as FWHM Γ, while γ_1 and γ_2 widths are reported as the Gaussian broadening parameter θ.

(class III spectra) and then irradiated with fast neutrons. The results for two such samples have been listed in Table IV-15, while an example spectrum was illustrated in Figure IV-1c (Section IV-A). The spectra of the irradiated 600°C-samples show a definite increase in γ_L's area fraction and corresponding decrease in γ_0; i.e., an increase of iron in precipitates at the expense of the solid solution phase. A sizable fraction (60%) of γ_L's increase, however, is due to an increase in the concentration of iron in small clusters (from γ_2^L), although γ_L is comprised primarily of γ-iron (γ_1).

The effects of fast neutrons on the Mössbauer spectra of aged Cu-Fe alloys are most reliably characterized by changes in the area fraction of γ_L for the reasons detailed in Section IV-C. Figures IV-17 and IV-18 show the changes in the area fraction, converted to Fe concentration (C_L), of the left-most component (γ_L) as a function of pre-irradiation heat treatment (IV-17) and fast neutron exposure (IV-18). A decrease in C_L signifies that Fe clusters or small precipitates have been broken-up by the irradiation. As seen from the figures, this occurs for most annealed samples, except those with very small clusters (e.g., the solution annealed and 335°,10 min.- aged samples) and those with very large precipitate particles (the 600°C- aged samples).

In order to determine the effects of fast neutrons on a possible γ-α phase transformation, two identical samples which had been cold-rolled and aged at 600°C for 1000 min. containing α-iron precipitates were irradiated at fluences of $2.7(10)^{19}$ and $9(10)^{19}$ n/cm^2. (A spectrum of an unirradiated sample showing the α-iron six line hf structure was shown in Fig. IV-7). The pre- and post-irradiation spectral parameters of the sample given the higher exposure are listed in Table IV-16. The

TABLE IV-15

MÖSSBAUER SPECTRA PARAMETERS FOR Cu-0.6% Fe SAMPLES AGED AT 600°C (CLASS III SPECTRA) BEFORE AND AFTER IRRADIATION

Sample[a]		Position (mm/sec)			Lorentzian Width (mm/sec)			Relative Area			χ^2/N
		$\gamma_2^L + \gamma_1$	γ_o	γ_2^R	$\gamma_2^L + \gamma_1$	γ_o	γ_2^R	$\gamma_2^L + \gamma_1$	γ_o	γ_2^R	
		(1) Fast fluence $\phi t \sim 2.7(10)^{19}$ n/cm^2:									
600°C 100 min	b	.178(4)	.479(5)	.775(7)	.238(2)	.248(4)	.23(3)	.631(6)	.342(5)	.027(4)	1.05
	a	.172(4)	.481(4)	.758(8)	.251(2)	.255(4)	.24(2)	.661(8)	.293(9)	.046(6)	0.96
		(2) Fast fluence $\phi t \sim 9(10)^{19}$ n/cm^2:									
600°C 10 min	b	.181(4)	.482(4)	.773(6)	.250(2)	.266(4)	.23(2)	.574(6)	.395(5)	.032(5)	1.17
	a	.174(4)	.484(4)	.728(8)	.248(2)	.266(5)	.30(2)	.630(8)	.30(1)	.07(1)	1.20

b = before; a = after irradiation

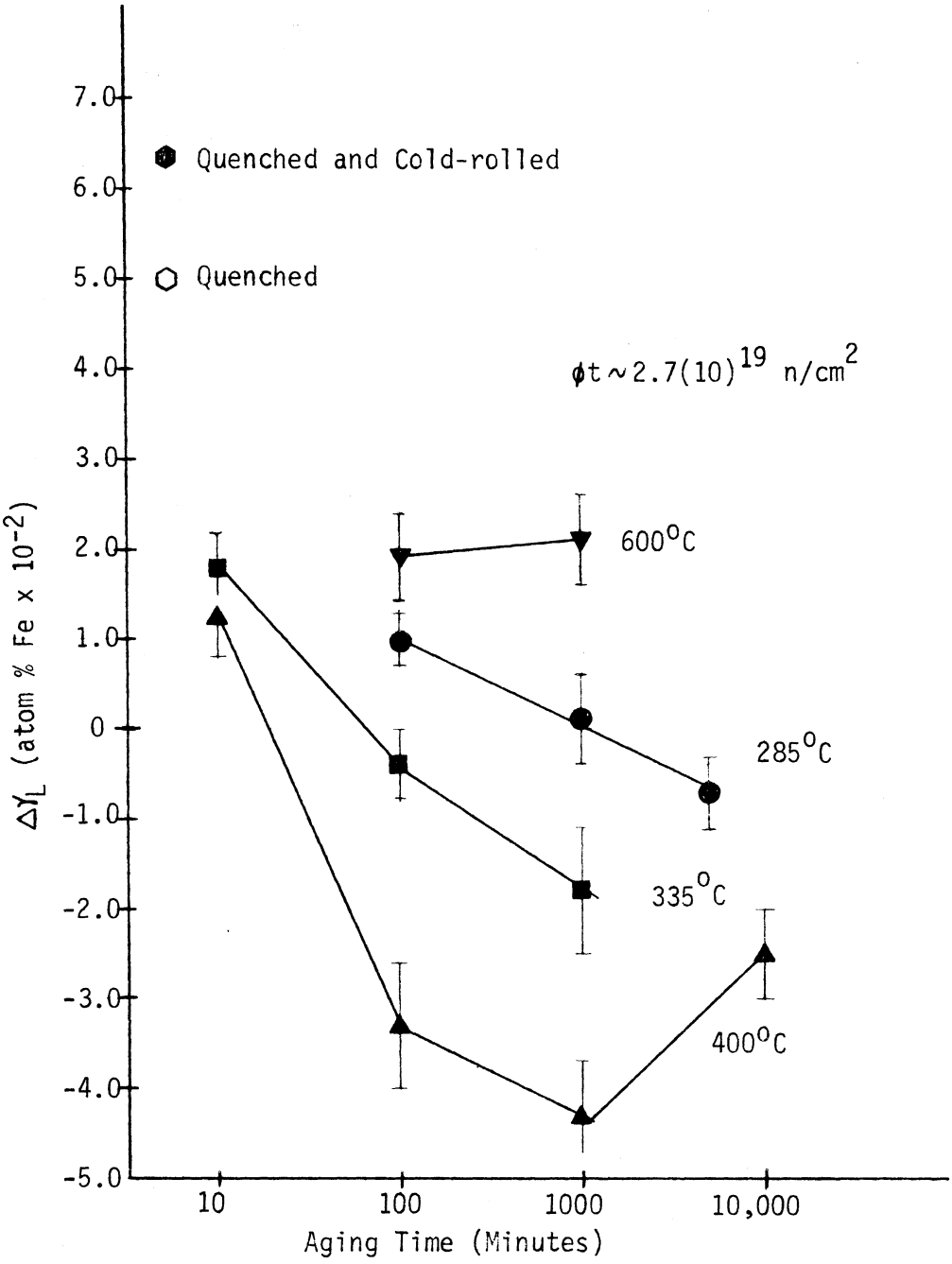

Figure IV-17.--Irradiation-induced change in the γ_L spectral component (in atom % Fe) as a function of pre-irradiation condition for annealed Cu-0.6at%Fe.

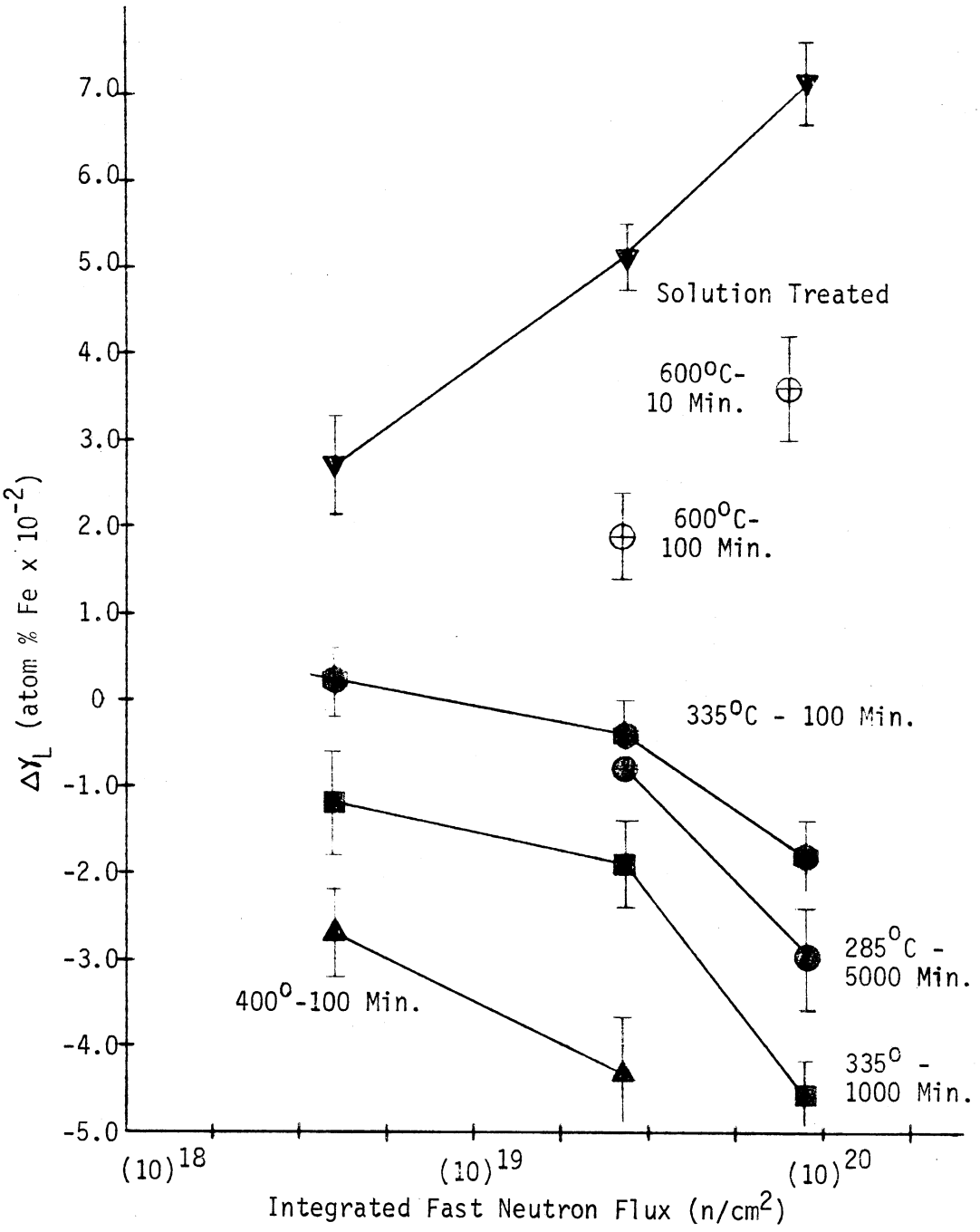

Figure IV-18.--Irradiation-induced change in the γ_L spectral component (in atom % Fe) versus fast neutron fluence for solution treated and aged Cu-0.6at%Fe alloy samples.

TABLE IV-16

MÖSSBAUER SPECTRA PARAMETERS BEFORE AND AFTER FAST NEUTRON EXPOSURE OF $\sim 9(10)^{19}$ n/cm^2 FOR A Cu-0.6% Fe SAMPLE AGED AT 600°C AND COLD-ROLLED

		Position (mm/sec)			Lorentzian Width (mm/sec)			Relative Area			
Type of Iron		$\gamma_2^L + \gamma_1$	γ_o	γ_2^R	$\gamma_2^L + \gamma_1$	γ_o	γ_2^R	$\gamma_2^L + \gamma_1$	γ_o	γ_2^R	χ^2/N
600°C 1000 min											
γ-iron	b	.178(4)	.484(5)	.75(1)	.244(2)	.231(5)	.24(3)	.413(8)	.303(8)	.041(6)	1.06
	a	.170(4)	.483(5)	.72(1)	.252(2)	.242(4)	.28(3)	.49(1)	.24(2)	.08(1)	1.03
		Centroid	Δ34	Δ25	Δ16	Aα					
α-iron	b	.26(8)	1.69(1)	6.142(7)	10.64(1)	.24(1)					
	a	.26(1)	1.70(2)	6.14(1)	10.632(9)	.19(1)					

b = before; a = after irradiation

results of the lower exposure are similar but less pronounced. Like the samples aged at 600°C which contained precipitates of only γ-iron, the spectra of the cold-rolled samples show an increase in the γ-iron phase and a corresponding decrease in solid solution iron as a result of irradiation. In addition, there also occurs a significant decrease in the area fraction of the six α-iron lines. This may be interpreted as evidence of either an irradiation-induced phase transformation, or simply a partial dissolution of the α-iron precipitate phase.

Finally, resistivity measurements were also performed on a few of the aged-irradiated samples. Because of the delicate nature of the thin foils (~½ mil in thickness) required for the Mössbauer measurements, only a few came through the irradiations without significant damage (i.e., pin holes and tears). Results from these samples are given in Table IV-17 below. The calculated concentration changes of Fe solute atoms were obtained using $\Delta\rho/\Delta c = 8.2\ \mu\Omega$-cm/at%Fe from Fig. IV-13. Making allowance for the difference in Fe concentrations, the results of Table IV-17 are in general agreement with Botax's resistivity data of irradiated Cu-1.7wt%Fe.

TABLE IV-17

IRRADIATION-INDUCED CHANGES IN RESISTIVITY OF AGED Cu-0.6at%Fe

Sample	Fluence	$\Delta\rho$ ($\mu\Omega$-cm)	ΔC(at%Fe)
335°C-10 min.	$2.7(10)^{19}$	-.126	-.016
335°-1000 min.	$4(10)^{18}$	+.16	+.02
335°-1000 min.	$2.7(10)^{19}$	+.32	+.04
400°-100 min.	$2.7(10)^{19}$	+.196	+.024
400°-1000 min.	$2.7(10)^{19}$	+.124	+.015
Quenched	$2.7(10)^{19}$	-.44	-.054
Quenched	$9(10)^{19}$	-.77	-.094

E. Discussion of the Irradiation Results

1. Irradiation-Induced Aging

One of the goals of the present research was to determine the extent of Fe precipitation induced by fast neutron irradiation in the copper-rich Cu-Fe system. In the past irradiation aging has been demonstrated in both the Cu-Be[102][144] and Cu-Fe[5] systems by bulk measurement techniques -- resistivity and hardness in the former and resistivity in the latter. In neither alloy system could any conclusions regarding the size of the precipitates formed be made, and only in Cu-Fe (Boltax[5]) was an attempt made to correlate resistivity with the quantity of iron precipitated. As shown in Section IV-C.2b, such a correlation is tenuous since anomalous resistivity effects are caused by the small Fe clusters that are formed by the irradiation. It is shown below that Mössbauer spectroscopy allows an estimation of not only the number of Fe atoms clustered during the irradiation of solution treated Cu-Fe alloys, but the approximate cluster size as well.

The Mössbauer results of the previous section clearly demonstrate the phenomenon of irradiation aging. As a result of the irradiations, the spectra of solution treated samples (Fig. IV-14) were converted to the Class I form characteristic of the incipient stages of clustering in Cu-rich Cu-Fe alloys. (Compare spectral parameter values of Table IV-10 with those of Table IV-4, especially the 285°-100 min. and 335°-10 min. aged samples). The very small negative shift in the centroid of γ_2^R (or the small decrease in the γ_2 doublet's splitting) as well as the relatively small changes which

occured in the Gaussian broadening parameters indicate that the Fe clusters formed during irradiation consist of only a very few atoms. The largest clusters are very likely those which already existed in the quenched sample prior to irradiation. It is tempting to attribute the difference in area fractions of the γ_L ($\gamma_1 + \gamma_2^L$) and γ_2^R components to larger clusters (>13 atoms) which might have been heterogeneously nucleated in displacement spikes or cascades. However, all of the other spectral parameter values (i.e., centroid positons and Gaussian broadening parameters) are suggestive of the formation of very small clusters as was discussed in Section IV-C.2 with regard to thermal aging. Also the post-irradiation spectra were able to be fit satisfactorily with Window's[10] constrained two component G-L model* with only a slightly enlarged χ^2 value over that of the three component fits. Therefore, it is very unlikely that Fe clusters extending beyond one nearest neighbor shell (or 13 atoms) have been formed during the irradiations. In short, the Mössbauer results in quenched-irradiated Cu-Fe are consistent with the formation of Fe clusters of a few atoms, and not full scale precipitate particles as suggested by Boltax.[5]

In addition to providing an insight into the size of Fe clusters formed by the irradiation of quenched Cu-Fe, the Mössbauer results also provide a very good estimation of the number of Fe atoms

---

*A comparison of the two and three component G-L fitting results for a typical quenched-irradiated 0.6at% Fe alloy was made on p. 140. The parameter values derived from both of the fitting methods indicate that only a very small change in the average size of Fe clusters occured during the irradiation. The average size of clusters existing in solution treated alloys is believed to be less than five atoms.

precipitated' or clustered from the solid solution phase. The table on p. 141 compares the irradiaton-induced concentration changes (at% Fe) determined from the resistivity results and the two Mössbauer fitting models for a typical quenched sample. The values obtained from the constrained two component fits to the ME data (2 G-L in the table) are the most representative of the depletion of iron from solid solution. The electrical resistivity results definitely underestimate the amount of iron depleted from solid solution due to the 'anomalous' scattering effects of the small clusters (Section IV-C.2b).

The actual number of Fe atoms per unit volume involved in the clustering process for a given irradiation can be simply determined from $N_C = N_o \Delta C_M$, where N_o is the atom density of copper and ΔC_M is the irradiation-induced concentration change obtained from the ME spectral areas of the γ_o phase before and after irradiation. The number of primary collisions per unit volume responsible for the clustered iron can be obtained from the time integrated form of Eq. II.27; i.e., $N_p \cong N_o \bar{\sigma}_s \bar{\Phi}$, where $\bar{\Phi}$ is the integrated fast neutron flux and $\bar{\sigma}_s$ the energy averaged (over fission spectrum) scattering cross section. In the table below values representing the number of Fe atoms clustered as well as the number of primary collision events responsible for the clustering are summarized for typical solution treated 0.6at% Fe samples.

Fluence (n/cm^2)	(1) $\#/cm^3$ Fe atoms clustered	(2) $\#/cm^3$ of primary collisions	(1)/(2)
$4(10)^{18}$	$4.4(10)^{19}$	$1.0(10)^{18}$	~ 44
$2.7(10)^{19}$	$8.6(10)^{19}$	$6.7(10)^{18}$	~ 13
$9(10)^{19}$	$1.2(10)^{20}$	$2.3(10)^{19}$	~ 5

From the last column in the above table, it is seen that the effectiveness of primary knock-ons in causing clustering decreases with increasing fluence; e.g., at the lowest fluence approximately 44 atoms were clustered per primary knock-on event, while at the highest exposure only about 5 atoms per primary were clustered. This phenomenon, also observed by Boltax[5] from resistivity data, is the combined result of a gradual depletion of Fe atoms from solid solution and the competitive process of irradiation-induced dissolution. The latter effect is discussed in detail later in this section. The effect of the concentration of solute atoms (i.e., the degree of supersaturation) upon irradiation-induced clustering was illustrated in Figure IV-15. As seen from this figure a depletion of Fe solute atoms leads to a decreased rate of iron clustering.

As discussed in Section II-D, irradiation aging occurs primarily by the enhancement of diffusion due to the introduction of excess vacancies into the lattice by fast neutron displacements. If a nominal value for $\bar{\nu}$ -- the number of displacements per primary knock-on event -- of 300 is taken as the number of vacancies created by one primary event, then from about $3(10)^{20}$ to $7(10)^{21}$ vacancies were created during the course of the irradiations. Most of these were probably annealed-out by migrating to various lattice sinks. However, according to Hart's[142] theory (see p. 127) many of the irradiation created vacancies should be attracted to solute atoms and Fe clusters, and thereby retained in the lattice. If so, then short term annealing at a low aging temperature, say $335^{o}C$, should cause Fe clustering in excess of that occuring in a solution treated sample identically aged. To test this hypothesis one of the quenched-

irradiated samples ($\phi t = 2.7 \times 10^{19}$ n/cm^2) was aged for 10 minutes at 335°C. The resulting spectrum (similar to Fig. IV-3b) showed a significant increase in the area fractions of γ_L and γ_2^R as well as a greater decrease in the splitting of the γ_2 doublet over that of the routinely aged sample. Since these are signs of a more advanced stage of aging, it is quite possible that vacancies in Cu-Fe are attracted to Fe solute atoms and/or Fe clusters.

2. Dissolution of Precipitates

The observed effects of fast neutrons on the Mössbauer spectra of aged alloys are caused by two competing irradiation-induced processes: enhanced diffusion leading to an increase in Fe clustering, and the dissolution of existing clusters within large displacement cascades (or spikes). The former process was discussed with regard to solution treated alloys. The latter mechanism, displacement spikes, was orginally proposed by Brinkman[96] and has since been studied by computer simulation[92][99] and also observed experimentally.[5][50] A summary of these studies and applicable theory was given in Section II-D.

The results reported in Section D.2 of this chapter show that the irradiation-induced changes in the Mössbauer spectra of aged alloys depend upon the stage of iron clustering (i.e., cluster size) in the pre-irradiated alloy.* Those samples containing very small

---

*As was indicated for thermally aged alloy samples, the extent and type of information (qualitative or quantitative) extractable from the ME spectra is also dependent upon the stage of clustering (i.e., it is linked to the ability to resolve the spectral components from the three classes of spectra observed). Thus, a quantitative analysis of irradiation-induced phase changes can be

clusters (e.g., the 335°C-10 min. and 285°C-100 min. samples in Tables IV-11 and IV-12) showed a net increase in the number of clustered atoms after an exposure of $\sim 2.7(10)^{19}$ n/cm^2, indicating that more Fe atoms were clustered than were dissolved by the irradiation. The small changes that occured in the positional and width (or Gaussian broadening broadening) parameters in the spectra of these samples indicate that the average size of the clusters following irradiation changed very little from the pre-irradiation value. The effects of an increasing fast neutron exposure on an aged alloy with very small clusters can be seen in Figure IV-18 (335°C-100 min. sample). At the lowest fast neutron exposure, the relative area of γ_L (i.e., the concentration of Fe cluster atoms producing γ_L) increases, whereas at higher exposures a net decrease in γ_L has occured. These results indicate that early in the irradiation, the formation and growth rate of the clusters due to vacancy migration exceeds the rate of dissolution of existing clusters by the displacement cascades. When clusters reach a critical size the rate of dissolution exceeds the rate of cluster formation and growth, and a net decrease in the cluster phase occurs. According to the discussion of Section IV-C.2c, this critical cluster size is probably less than 13 atoms.

---

performed satisfactorily in well-aged (600°C) samples and in those samples containing Fe clusters of less than about 13 atoms (i.e., solution treated and mildly aged samples). Irradiation-induced changes in Cu-Fe samples in an intermediate stage of clustering (all class II and advanced class I spectra) can only be followed in a semi-quantitative manner through changes in the area fraction of γ_L, the left-most component produced by both surface and volume Fe atoms in clusters.

The effects of irradiation on aged alloys with slightly larger clusters (but still exhibiting class I spectra) were illustrated in Figure IV-16 for the 335°C-1000 min. sample. (The associated 3-line spectral parameters were listed in Table IV-13 for all three fast neutron exposures while Table IV-12 gives the two G-L component parameters for the intermediate exposure.) These results clearly demonstrate the retrogression effects of displacement cascades or spikes on aged alloys containing small coherent clusters. (In this case the cluster size was estimated to be anywhere from about one to at most three near neighbor shells in radius; i.e., about 13 to 43 Fe atoms -- see table on p. 128). Depending upon the fitting model used, two slightly different interpretations can be made of the data. In using the two component G-L fit ($\gamma_0 + \gamma_2$), it is assumed that both the pre- and post-irradiated samples contain clusters of 12 atoms or smaller. With this in mind, the spectral parameters of Table IV-12 for the 335°-1000 min. sample show a definite decrease in the number of Fe cluster atoms (from the decrease in γ_2's relative area) as well as a decrease in the average cluster size (from the increase in γ_2's splitting and the slight positive shift in its centroid) as a result of the irradiation.

The three component G-L fits (Table IV-13) possibly provide a better insight into the dissolution process, assuming the clusters to be larger than 12 atoms in the aged sample. The results of Table IV-13 show a monotonic decrease in the relative area of γ_L and a concurrent increase in that of γ_2^R with increasing fast neutron exposure.* This could be interpreted as evidence that the dissolution or break-up of larger clusters in this alloy is incomplete; i.e.,

that all of the atoms in a cluster enveloped by a displacement spike do not go into solid solution but form smaller clusters in the wake of the displacement cascade. It is very possible that 'thermal' spikes[95] associated with the displacements would cause localized annealing or aging of the supersaturated Fe solute atoms dispersed in the damage cascade. The large positive shift of γ_2^R's centroid indicating a decrease in the average cluster size is consistent with this mechanism, although not necessarily conclusive proof of it. In any event, at some stage of aging only a partial break-up of clusters by displacement spikes would be expected.

This is definitely the case with the Cu-0.6at%Fe samples that were aged for 100 minutes at 400°C prior to irradiation (Table IV-14). The pre- and post-irradiation spectra of these samples are of the class II type, characteristic of the early and intermediate stages of -precipitate (large cluster) growth. (Recall from Section IV-C that the left component is comprised mainly of the γ_1- or γ-iron singlet while the very broad right component consists of some γ_0-iron and an unresolved doublet due to γ_2-surface iron. The three line Gaussian-distributed Lorentzian fits were an attempt at unfolding this complex structure.) The large decrease in the relative area

---

*The decrease shown for the γ_0 component in the 335°-1000 min. sample could very well be due to the inadequacy of the fitting model and not an actual decrease in Fe solute atoms. The large increase in ρ (Table IV-17) measured for the sample exposed to a fluence of $2.7(10)^{19}$ n/cm^2 indicates that an increase in the number of solute atoms has occured; however, a sizable fraction of this resistivity increase is very likely caused by small residual clusters from the dissolution process.

of γ_L (see Table IV-14 and Figures IV-17 and IV-18) signifies the breaking-up of γ-precipitates or large iron clusters by the displacement spikes. The increase in broadening of the right component as well as its positive positional shift could be due to a combination of an increase in the γ_o phase and a decrease in the average cluster size. Comparison of the resistivity changes (Table IV-17) observed for the 335°-1000 min. sample ($\Delta\rho$ = +.322) and the 400°-100 min. sample ($\Delta\rho$ = +.196) after irradiation indicates that the 'dissolved' clusters in the former are more highly dispersed (i.e., they have a greater effect on the resistivity). Thus, it can be concluded that the broadening and shift in the right component of the 400°-aged samples is primarily caused by the incomplete break-up of iron clusters in the displacement spikes and the resulting smaller average cluster size.

In Section IV-C.2 it was concluded that the clusters formed in the 0.6% Fe samples aged at 400°C for more than 100 minutes were of the order of 6 Å or greater in radius. The displacement spikes or damage cascades would in turn have to be considerably larger than this to produce the observed effects. (Boltax[5] and Piercy[50] estimated the spike size to be about 35 Å in radius).* Figure IV-17 shows that aging at 400°C for times of ~10,000 minutes causes a decrease in the observed dissolution effects as a result of the increased size of the precipitates. (Recall that a cluster size of about 20 Å was roughly

---

*Boltax's size value, although reasonable, was based on a faulty calculation of precipitate particle size as well as an estimation of irradiation-induced concentration changes in the γ_o phase from rather misleading resistivity data.

estimated from the Mössbauer data for this sample.) Further aging at 400°C, or an increase in annealing temperature would eventually produce clusters too large to be significantly effected by the damage cascades.

This occured for all of the samples aged at 600°C (see Table IV-15 and Figure IV-17). The Mössbauer results -- which for the class III spectra can be interpreted quantitatively -- indicate a significant decrease in Fe solute atoms and a slight increase or growth of the large γ-iron precipitates. (Some 60-70% of the increase in the γ_L component is due to γ_2-iron.) The increase in γ_2's area fraction and the negative shift in the γ_2^R centroid indicate that the small clusters observed in the 600°-aged alloys (see p.118) have grown slightly during the irradiation.

The extent of irradiation-induced dissolution in the aged Cu-0.6at%Fe samples (i.e., the approximate number of iron atoms 'dissolved' during the course of the irradiation) can be approximated from the changes in the spectral area of γ_L. (The results should be good to within a factor of about two for most of the aged samples.) The problem is complicated because of the competing effects of irradiation-induced aging and dissolution on the concentration of Fe in clusters or precipitates. Assuming that the irradiation aging of the supersaturated solid solution can be treated independently from the re-solution of clusters, then the desired result can be obtained with the aid of Figures IV-15 and IV-17 in the following manner. The total concentration (atom %) of Fe atoms in an aged sample 'dissolved' by displacement spikes can be approximated by subtracting the aging contribution to γ_L --i.e., the change in γ_L expected

for a solution treated alloy with the same initial solute (γ_o) concentration as the aged sample -- from the appropriate $\Delta\gamma_L$ values of Figure IV-17. The results are shown in Figure IV-19 as dashed lines along with the uncorrected data (solid lines). The total number of cluster atoms per unit volume 'dissolved' in displacement spikes is then obtained by multiplying the concentration values of the figure by the atom density of copper ($\sim 8.5 \times 10^{22}$). Taking the 335^{o}-1000 min. sample as an example, the approximate number of Fe cluster atoms broken-up by a fast neutron exposure of $2.7(10)^{19}$ n/cm^2 is about $3.7(10)^{19}$ atoms/cm^3; or approximately 5 atoms 'dissolved' per primary knock-on event. At the lowest exposure this value is about 30 atoms per primary event, whereas at the highest exposure it decreases to only 3 atoms per primary knock-on. This decrease in the re-solution effectiveness with increasing fast neutron exposure is most likely the result of saturation effects caused by the overlapping of the damage cascade volumes.

A secondary objective of this research was to ascertain whether fast neutron irradiation could induce a γ-α transformation in well aged Cu-Fe alloys. Although not conclusive proof to the contrary, there was no evidence of the α-iron six line structure in the spectra of a 0.6at% sample aged at 600^{o}-1000 min. and exposed to a fluence of $2.7(10)^{19}$ n/cm^2. Similar samples which had been cold-rolled either before or after aging showed definite signs of α-iron formation in their ME spectra (Fig. IV-7). Upon irradiating two of these cold-rolled samples to exposures of $2.7(10)^{19}$ and $9(10)^{19}$ n/cm^2, a decrease of significant magnitude in the area fraction of α-iron occured (Table IV-16)--an opposite effect to what was previously

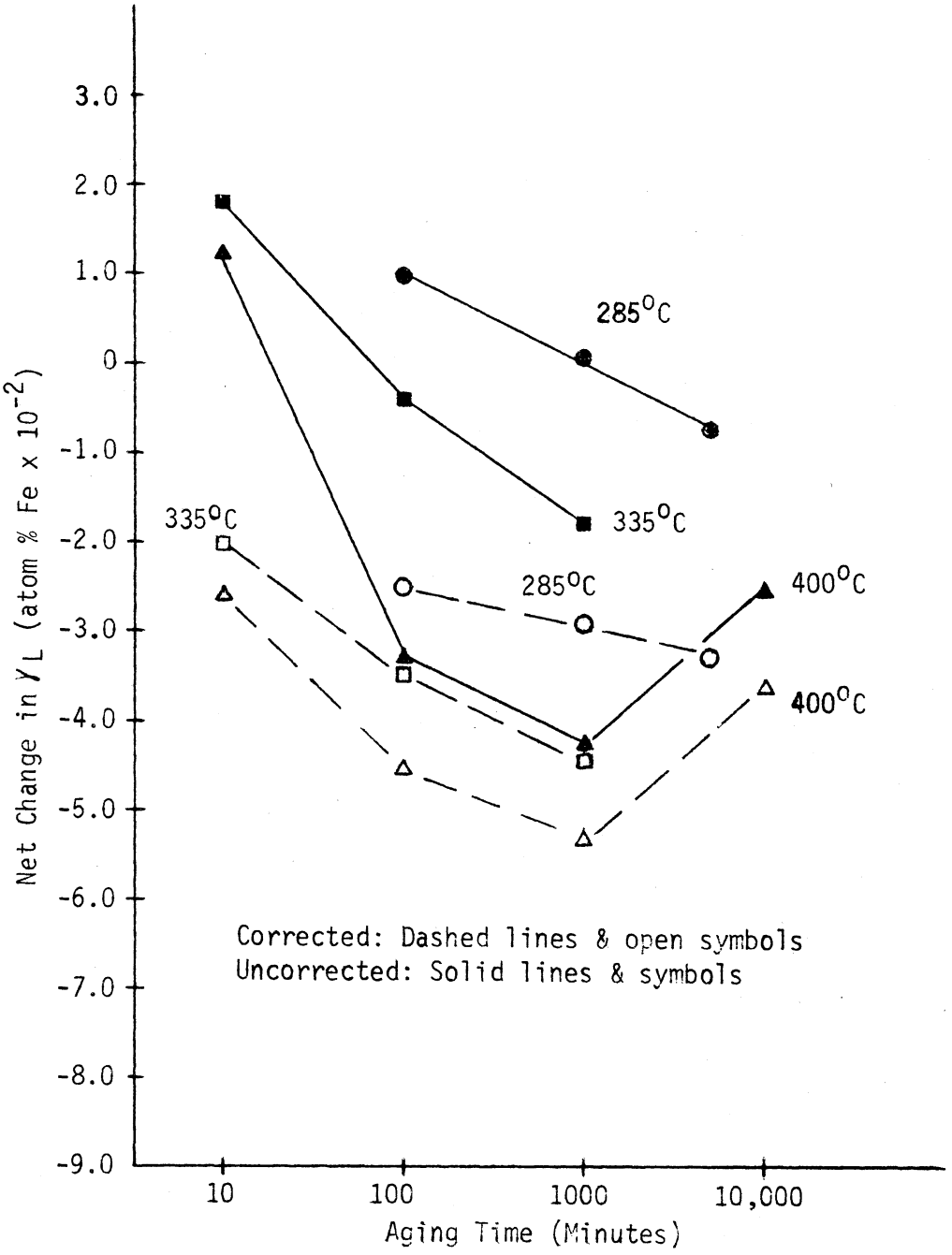

Figure IV-19.--Net Re-solution Effects of Displacement Spikes as a Function of Pre-irradiation Heat Treatment.

reported.[108] Evidently Fe atoms existing in α-iron platlets within large γ-iron precipitates were converted by the displacement spikes to the γ-form.

3. Summary

The effects of fast neutron irradiation on solution treated and aged Cu-0.6at%Fe samples has been followed with some success by Mössbauer spectroscopy. In general, the results have confirmed the conclusions of similar studies using resistivity[5] and magnetization[50] measurement techniques; i.e., that high fast neutron exposure causes both aging and re-solution effects in age-hardening alloys. In addition, the Mössbauer technique provided an insight into the local environment of the precipitate or cluster phase in both pre- and post-irradiated alloy samples that was not possible with the other techniques.

Specifically, in the case of solution treated alloys, the Mössbauer spectra provided information concerning both the extent of irradiation-induced aging and the approximate size of the clusters formed. The results are consistent with the formation of very small clusters of less than 12 atoms in the quenched-irradiated alloys.

The re-solution effects of displacement cascades caused by fast neutron interactions in aged Cu-0.6at%Fe samples was shown to be extremely dependent upon the stage of aging or the cluster size. Aged samples containing very small clusters ($<$12 atoms) experienced essentially complete dissolution of Fe clusters, whereas those with clusters of intermediate sizes (up to about 20 Å in radius) experienced incomplete cluster break-up in the displacement cascades.

In contrast, well-aged samples containing large γ-iron precipitates (> 50 Å) did not experience any dissolution effects, but instead exhibited a very slight growth in the γ-iron phase. Finally, the Mössbauer measurements were also able to determine the effects of irradiation on the equilibrium precipitate phase, α-iron.

APPENDIX A

SPECTRAL AREA CONSIDERATIONS

The results of Chapter IV indicate that the spectral components for FCC iron 'phases' in copper are not well resolved. Therefore, before applying the ideas of Section II-A.2 it is necessary to consider saturation and overlap effects in Equation (II.10) for the Cu-Fe alloy absorbers used in this study. Since there are many similar Fe configurations which produce a given absorption line, it is assumed that $k_i(E)$ in Equation (II.10) can be represented by a Lorentzian distribution with a broadened width. The results of this work indicate that Gaussian distributed Lorentzian functions provide better fits to the data; however, a broadened Lorentzian distribution is used for $k_i(E)$ in the following argument because of its mathematical simplicity.

As given by Equation (II.10) the total area under an absorption spectrum is

$$A = f_s \int_{-\infty}^{\infty} dE[1-e^{-T_i k_i(E)}] \qquad (A.1)$$

where the sum over i includes any split components; e.g., the quadrupole split doublet designated γ_2. Since the f value for small FCC iron clusters is not known, it is assumed that the f_i's for FCC iron configurations are equal to the value for isolated Fe in copper (f = 0.73). The effective thickness T_i for the ith phase can then be approximated as

$$T_i \simeq A_i^* T \qquad (A.2)$$

where T is the total effective absorber thickness and A_i^* is the experimental area fraction for the ith spectral component (i.e. $A_i^* = A_i/A$). For the majority of the Cu-Fe absorbers used in this work, $0.6 \leq T_a \leq 1.0$. The maximum absolute value of the argument in the exponential function of Equation (A.1) will be less than T_a since the Cu-Fe spectra contain at least three partially separated components. The effective thickness per component in most annealed samples is < 0.4. Making allowances for the overlapping of the absorption lines, the following upper limit can be established:

$$\text{Max}[\sum_i^N T_i k_i(E)] \lesssim 0.5$$

To obtain an expression for the error associated with neglecting overlap effects in our Cu-Fe absorbers consider the expanded form of Equation (A.1),

$$A = f_s \int_{-\infty}^{\infty} dE\{1 - \prod_i^N [\sum_k \frac{(-1)^k}{k!} T_i^k k_i^i(E)]\} \qquad (A.3)$$

where the product is over N absorption lines. Keeping only terms of second order or less in T_i, Equation (A.3) can be approximated to better than 3% by

$$A \simeq f_s \int_{-\infty}^{\infty} [\sum_i^N T_i k_i(E) - \frac{1}{2} \sum_{ij}^{NN} T_i T_j k_i(E) k_j(E)] dE \qquad (A.4)$$

The integral of the first term of Equation (A.4) is given by

$$I = \frac{1}{2}\pi f_s \sum_i^N T_i \Gamma_i \qquad (A.5)$$

which is just the thin absorber result for well separated lines. Integration of the second term can be accomplished in the complex plane using the Theory of Residues. The integral can be written as

$$II = -\frac{f_s}{2} \sum_{i,j}^N T_i T_j \int_{-\infty}^{\infty} k_i(E) k_j(E) dE$$

or

$$II = -\frac{f_s}{2} \sum_{i,j}^N T_i T_j \int_{-\infty}^{\infty} \frac{a_i^2 a_j^2}{[(E-E_i)^2+a_i^2][(E-E_j)^2+a_j^2]} dE$$

where $a_i = \Gamma_i/2$. The path of integration is taken in the upper half of the complex plane about the poles at (E_i+ia_i) and (E_j+ia_j). The result is

$$II = -\frac{f_s}{2} \sum_{i,j}^N T_i T_j \{2\pi i a_i^2 a_j^2 [\frac{1}{2ia_i[E_i-E_j+i(a_i+a_j)][E_j-E_j+i(a_i-a_j)]}$$

$$+ \frac{1}{2ia_j[E_j-E_i+i(a_i+a_j)][E_j-E_i-i(a_i-a_j)]}]\}$$

$$II = -\frac{\pi}{16} f_s \sum_{i,j}^N T_i T_j (\Gamma_i+\Gamma_j) \frac{\Gamma_i \Gamma_j}{\Delta_{ij}^2+(\Gamma_i+\Gamma_j)^2/4} \qquad (A.6)$$

$$= -\frac{\pi}{8} f_s \sum_i \Gamma_i T_i^2 \quad ; \text{ for } j = i$$

where $\Delta_{ij} = (E_i-E_j)$.

Combining Equation (A.5) and (A.6) gives the desired approximation for the total spectral area,

$$A \simeq \frac{\pi}{2} f_s \left[\sum_i^N \Gamma_i T_i \left(1 - \frac{T_i}{4}\right) - \frac{1}{8} \sum_i^N \sum_{j \neq i}^N (\Gamma_i + \Gamma_j) T_i T_j \frac{\Gamma_i \Gamma_j}{\Delta_{ij}^2 + (\Gamma_i + \Gamma_j)^2/4} \right] . \quad (A.7)$$

The first term above represents the second order approximation to the total spectral area for N non-overlapping lines, while the second term accounts for overlapping of the ith and jth absorption lines. The fractional error in the total area cuased by ignoring the overlap terms can thus be approximated by

$$\varepsilon \simeq \frac{\frac{1}{8} \sum_i^N \sum_{j \neq i}^N T_i T_j (\Gamma_i + \Gamma_j) \frac{\Gamma_i \Gamma_j}{\Delta_{ij}^2 + (\Gamma_i + \Gamma_i)^2/4}}{A/(\pi f_s/2)} \quad (A.8)$$

Similarly, the fractional error in the ith spectral component's area is approximately

$$\varepsilon_i \simeq \frac{\frac{T_i}{8} \sum_{j \neq i}^N T_j (\Gamma_i + \Gamma_j) \frac{\Gamma_i \Gamma_j}{\Delta_{ij}^2 + (\Gamma_i + \Gamma_i)^2/4}}{A/(\pi f_s/2)} \quad (A.9)$$

The errors associated with neglecting overlap effects were estimated for several Cu-Fe samples which were representative of the various heat treatments. This was accomplished by using the experimental values obtained for the linewidth Γ_i (for the Gaussian-distributed Lorentzian fits this was taken as the FWHM of the convolution--see Chapter III, Section D) and the spacings Δ_{ij} in the above equations. In general, the spectra contained three partially resolvable components

(e.g., see Figure IV-1), although the lower energy (left) spectral line is most likely a superposition of two individual lines. In determining the "overlap" errors, it was treated as a single component. Except for the samples annealed at 400°C, these errors amounted 4% or less. In the case of those samples annealed at 400°C for periods of 100 minutes or greater, the "overlap" errors approach 10% because of the extremely poor spectral component resolution. In all cases these errors are in the same direction, i.e., neglecting ε causes an underestimation of the atom concentration. As a result, "overlap" errors tend to cancel when differences in identical spectral components are taken to determine phase changes; e.g. before and following irradiation.

APPENDIX B

POINT CHARGE CALCULATIONS OF QUADRUPOLE SPLITTINGS IN Cu-Fe

According to Window[8,15] the screening charge distortion that occurs when two or more Fe atoms cluster in a Cu or Au lattice produces an electric field gradient (EFG) that gives rise to a resolved doublet in their Mössbauer spectra. To estimate the EFG caused by Fe clustering in Cu, we assume that the screening charge distortion can be approximated by an effective point charge q located along the lines joining adjacent Fe atoms. Only nearest-neighbors are considered in the calculation, since the EFG varies as $1/r^3$ and the Fe screening charge does not extend appreciably past the nearest-neighbor shell.

For a distribution of n equal point charges q about a test nucleus, the ij^{th} element of the EFG is given by[126]

$$V_{ij} = \sum_{k=1}^{n} q(3x_{ki}x_{kj} - r_k^2\delta_{ij})r_k^{-5} \qquad (B.1)$$

where r_k is the distance between the test point and the k^{th} charge, and (x_{k1},x_{k2},x_{k3}) is the position of the k^{th} charge. As discussed in Chapter II (see Equation II.18), an electric field gradient $\bar{\nabla}\bar{E}$ gives rise to a quadrupole splitting in Fe^{57} spectra of

$$\Delta E = \frac{eQV_{zz}}{2}\left(1+\frac{\eta^2}{3}\right)^{1/2} \qquad (B.2)$$

where η is given by Equation (II.19). The principal value V_{zz} and the asymmetry parameter η are determined by diagonalizing the EFG whose components are obtained from Equation (B.1).

From Equation (B.2) the splitting observed when an Fe^{57} nucleus in Cu has one Fe nearest-neighbor atom is $\Delta E_1 = Q_1 q_1$, where $Q_1 = eQ/\langle r^3 \rangle$ and q_1 is the effective charge. As the number of Fe nearest-neighbors increases, the effective charge localized along an Fe-Fe direction would be expected to decrease. The seven screening electrons of the test atom would be expected to be distributed according to the density of available d states on the twelve nearest neighbors. Assuming the charge is distributed uniformly among the available states and assuming the effective charge q_n can be approximated by the difference between the charge localized on each of the n Fe-Fe axes and that localized on each of the (12-n) Fe-Cu axes, the effective charge on each of n Fe neighbor axes is given by

$$q_n = \frac{11+\alpha}{(12-n) + n\alpha} q_1 \qquad \text{(B.3)}$$

where α is the ratio of the densities of states (Fe to Cu) and q_1 is the effective charge for one Fe neighbor.

This is the same model as used by Window to fit Au-Fe spectra.[15,16] For his Au-Fe data, $\alpha = 17$ was found to give the most consistent fits to spectra for alloys with Fe concentrations in the range 2-31%. This value is about four times that expected from calculations, which is not too surprising since the radial distribution of the screening charge and the effects of core polarization through anti-shielding were not accounted for in Window's model.

Recognizing its deficiencies, it is still instructive to apply the point charge model to estimate the quadrupole splittings that occur when small Fe clusters form in Cu. This has been done in Table B-1 for Fe^{57} with up to five Fe nearest-neighbors. Since the effects of Fe in Cu and Au are similar, the value $\alpha = 17$ obtained by Window[16] for Au-Fe alloys is used here to calculate the effective charge from Equation (B.3). The EFG for a given near-neighbor configuration is calculated from Equation (B.1) and is expressed in terms of an effective charge q_n, which is determined from Equation (B.3). The quadrupole splitting for a given configuration is determined from Equation (B.2) and is expressed in units of Q_1--see the third column in Table B-1. The fifth column of the Table lists the ratios of the quadrupole splittings resulting from n Fe nearest-neighbors to that for a single Fe neighbor. The values given in parentheses in the final two columns were obtained using the value $\alpha = 5$ in Equation (B.3), which is more representative of the density of states ratio.[15] On the basis of this simplified point charge model, the results of Table B-1 indicate that the cluster doublet for Fe in Cu should remain fairly well resolved for up to 5 Fe nearest-neighbors.

It is interesting to compare the quadrupole splitting observed for the doublet in quenched Cu-Fe alloys ($\sim$.58 mm/sec--see Chapter IV and References 7 and 8) with that for a high spin ferrous compound. The splitting of the Fe^{57} excited state expected for a single d electron in a pure orbital state is about 3 mm/sec.[127] Assuming that the anti-shielding factors and covalency effects are about the same in both cases, a charge asymmetry of about 0.17e in the 3d state for an Fe pair in Cu is indicated.

TABLE B-1

ESTIMATED QUADRUPOLE SPLITTINGS
FOR Fe CLUSTERS IN COPPER

# Nearest Neighbors	Configuration*	$\Delta En/Q_1$	q_n/q_1	$\Delta En/\Delta E_1$
1	1-z axis	q_1	(1) 1	(1) 1
2	2-xy	q_2	(0.8) 0.64	(0.8) 0.64
2	2-z axis	$2q_2$	(0.8) 0.64	(1.6) 1.28
3	3-xy	$1.7q_3$	(0.67) 0.47	(1.1) 0.82
3	2-xy, 1-xz	$1.2q_3$	(0.67) 0.47	(0.8) 0.57
4	4-xy	$2q_4$	(0.57) 0.37	(1.1) 0.74
4	3-xy, 1-xz	$1.7q_4$	(0.57) 0.37	(0.97) 0.64
5	4-xy, 1-xz	$2q_5$	(0.50 0.30	(1.0) 0.60

*Indicates the number of nearest neighbors in a given plane or on a given axis; e.g., 3-xy, 1-xz indicates three nearest neighbors are in the xy plane of the test nucleus, while one Fe nearest-neighbor atom is located in the xz plane.

APPENDIX C

MÖSSBAUER SPECTROMETER DETAILS

A. Drive System Design Considerations

As discussed in Section B of Chapter III, modification of the original drive system was necessitated by the desire to (a) decrease equipment broadening of the resonant lines, (b) improve the velocity stability of the spectrometer, and (c) reduce the frequency of repairs and tuning operations required to keep the drive system on-line. To accomplish these objectives, an ultrastable function generator external to the MCA's time base system and a drive amplifier containing recent solid state components were designed and constructed. The function generator-drive amplifier combination was designed to provide a synthesis of square, triangular and parabolic waveforms which approximates the voltage signal required to give the drive transducer a linear velocity response. Details are given below.

1. The Drive Signal

Although design details may differ between the many electro-mechanical Mössbauer drive systems presently in use, they all possess one feature in common--negative feedback. Basically, these systems employ a velocity transducer coupled to the drive's moving member which produces a voltage proportional to the instantaneous velocity. A reference signal of the desired form is derived from an external function generator[111] or from the multichannel analyzer-time

base system[37,109] and is compared with the signal from the velocity pick-up transducer. The resulting difference voltage, called the error signal, is fed to the driving transducer, thereby controlling the system's motion. Usually, such systems employ a single feedback loop and control the drive's motion with only the error signal. This method requires a relatively high loop gain which, in turn, leads to poor frequency stability.

An improved approach to the problem is to derive a signal which approximates the exact waveform needed to give the desired velocity response (in this case, triangular) and employ negative feedback only to correct for small deviations from the desired motion. This concept has been used by M. B. Stearns* and was adopted by Ullrich[34] in the design of the Nuclear Engineering Department's original ME spectrometer. A similar approach has been described by Kankeleit.[112]

In order to construct the required drive signal, it was necessary to determine the electro-magnetic and mechanical characteristics of the drive transducer. The transducer used consists of a drive coil rigidly coupled to the pick-up coil through a moving shaft whose motion is constrained at both ends by two linear leaf springs. Both coils move in their own permanent magnetic fields, which (a) for the drive coil produces a driving force proportional to its current; i.e.,

$$F(t) = cI(t) \ ,$$

and (b) for the pick-up coil produces a voltage proportional to its velocity. The equation of motion for the drive is

---

*Ford Scientific Laboratory, Ford Motor Company, Dearborn, Michigan.

$$m\frac{d^2x}{dt^2} + \beta\frac{dx}{dt} + kx = cI(t) \ , \qquad (C.1)$$

where k is the spring constant, β the damping factor, m the mass of the moving member (includes the source, both coils and the drive shaft), and I(t) the current supplied to the drive coil. The drive coil also possesses a resistance R and an inductance L. In addition, its motion in a constant magnetic field produces a back e.m.f. (Lenz's law) of $c\frac{dx}{dt}$, where the constant c is the same as that appearing in Equation (C.1). Thus, the voltage across the drive coil is given by

$$V(t) = RI(t)+L\frac{dI(t)}{dt} + c\frac{dx}{dt} \ . \qquad (C.2)$$

Eliminating the current I(t) from Equations (C.1) and (C.2) gives the desired relation between the signal voltage and the drive's motion.

$$V(t) = \frac{Lm}{c}\frac{d^3x}{dt^3} + \left(\frac{L\beta+Rm}{c}\right)\frac{d^2x}{dt^2}$$

$$\left(\frac{Lk+R\beta}{c} + c\right)\frac{dx}{dt} + \frac{Rk}{c}x \ . \qquad (C.3)$$

The drive coil's force constant c was given by the transducer's manufacturer as 28 Nt./amp. All of the other transducer characteristics were either measured directly or determined experimentally.* The values obtained are as follows: resistance, R = 100a; inductance, L ≃ 1.5 mH; mass, m = .306 kg; spring constant, k ≃ $3.4(10)^3$ Nt./m; and damping

---

*The spring constant k and damping factor β were obtained from the response of the drive to an initial displacement of the drive shaft as determined from the pick-up transducer's voltage.

factor, $\beta \simeq .74$ kg/sec. The system's natural frequency is then

$$f_o = \frac{1}{2\pi}\sqrt{\frac{k}{m}} \simeq 17 \text{ Hz} .$$

Because of the coil's relatively small inductance value, terms in Equation (C.3) containing L can be ignored without causing significant error in the design. Thus, the drive system's response to the voltage signal V(t) can be written as

$$V(t) \simeq \frac{Rm}{c}\frac{d^2x}{dt^2} + (\frac{R\beta}{c} + c)\frac{dx}{dt} + \frac{Rk}{c}x \quad . \qquad (C.4)$$

Since the desired velocity, $\frac{dx}{dt}$, is to be triangular in shape, Equation (C.4) requires the driving voltage to be the sum of square, triangular and parabolic waveforms. One method of determining the relative amplitudes of these waveforms as a function of frequency and maximum velocity is to expand the parabolic displacement x in a Fourier series and then substitute the expansion into Equation (C.4); i.e.,

$$x(t) = x_m P(t) = \frac{32}{\pi^2} x_m \sum_n \frac{\sin(2n+1)\omega t}{(2n+1)^3}$$

$$V(t) \simeq \frac{-Rm}{c}\omega^2 x_m (\frac{32}{\pi^2}) \sum_n \frac{\sin(2n+1)\omega t}{2n+1}$$

$$+ (\frac{R\beta}{c} + c)\omega x_m (\frac{32}{\pi^2}) \sum_n \frac{\cos(2n+1)\omega t}{(2n+1)^2}$$

$$+ \frac{Rk}{c} x_m (\frac{32}{\pi^2}) \sum_n \frac{\sin(2n+1)\omega t}{(2n+1)^3} \qquad (C.5)$$

Noting that the maximum velocity is $v_m = \frac{4}{\pi}\omega x_m$ or $8fx_m$, and that the terms

$$T(t) = \frac{8}{\pi^2}\sum_n \frac{\cos(2n+1)\omega t}{(2n+1)^2}$$

and

$$S(t) = -\frac{4}{\pi}\sum_n \frac{\sin(2n+1)\omega t}{2n+1}$$

are the Fourier expansions of the triangular and square waveforms, Equation (C.5) can be written as

$$V(t) \simeq \frac{4Rm}{c} v_m f S(t) + \left(\frac{R\beta}{c} + c\right) v_m T(t) + \frac{Rk}{c}\frac{v_m}{f} P(t) \ . \qquad (C.6)$$

In this expression the functions S(t), T(t) and P(t) represent the square, triangular and parabolic waveforms with unit amplitudes. Their coefficients given in Equation (C.6) relate the respective amplitudes of the individual waveforms to the transducer's characteristics. The amplitude coefficients are:

$$A_s = \frac{4Rm}{c} v_m f \ , \quad A_t = \left(\frac{R\beta}{c} + c\right) v_m \ , \quad A_p = \frac{Rk}{c}\frac{v_m}{f} \ . \qquad (C.7)$$

The ratios A/v_m are plotted against the drive frequency in Figure C-1 along with their measured values obtained at two frequencies. In the design of the drive system, Figure C-1 was used to determine the proper resistive feedback ratios at the summing amplifier for the three waveforms.

2. The Drive System

Figures C-2 and C-3 show the schematic diagrams of the function generator and drive amplifier, respectively. Two of the three required waveforms are provided by the function generator (Figure C-2), while the third, the parabolic wave, is obtained by integration of the triangular wave at OA-5* (operational amplifier #5, Figure C-3). The synthesis of the three waveforms occurs at the summing junction of the drive amplifier, just prior to the driver or booster amplifier stage. The relative amplitudes of the triangular and parabolic waves are determined by the variable resistors R_t and R_p in the drive amplifier, while the square wave's amplitude is controlled by the variable feedback resistor R_s in the function generator's output circuit (OA-4). Negative feedback is provided by the output of OA-7 in which the triangular reference signal is compared to the amplified (x50) velocity pick-up signal. The relative weight of the resulting error or correction signal is controlled by the variable resistor R_c.

The function generator of Figure C-2 is a modified version of Cohen's design[113] and produces precise, ultra-stable triangular and square waves. (The triangular wave's linearity and stability are better than .04%, while the square wave's halves are equal to within .01%). This is accomplished by the operational amplifiers OA-1 and OA-2, which act as an integrator and comparator, respectively. Because of positive feedback, any positive input voltage tends to drive OA-2 to saturation. Its output, however, is clipped at about +9v by the Zener

---

*All operational amplifiers were obtained from Philbrick/Nexus Research of Dedham, Massachusetts. Their ± 15v DC bias supply was provided by two Sorensen Model QSA 18-1.1 power supplies.

diodes, Z_1 and Z_2, and the resulting constant 9v signal is integrated (and inverted) by OA-1 to produce a negative ramp function. When the comparator's input is driven negative by OA-1's output, the output of OA-2 reverses polarity and is clipped at a -9v by the Zener diodes. Thus, the output of the comparator (OA-2) is a square wave, and the output of the integrator (OA-1) is a triangular wave. The signal frequency is determined by the product of C and $(R_{f1}+R_{f2})$ and can be varied by changing the setting of R_{f2}. Both the triangular and square waves are fed to the drive amplifier through two high stability, low drift operational amplifiers, OA-3 and OA-4. The ratio of the variable feedback resistor R_t to the 11 kΩ input resistor of OA-3 determines the amplitude of the triangular reference signal, and thus the maximum velocity of the source's motion. The trigger generator provides a synchronizing pulse a few microseconds long once per cycle to initiate the MCS sweep.

Since the operational amplifiers are DC coupled in the drive system, care was taken to minimize DC drifts. All of the operational amplifiers at the output of the function generator and in the signal shaping and input stages of the drive amplifier were chosen for their high precision, high stability and low drift characteristics. Initially, it was believed that chopper-stabilized amplifiers would be required at the inputs to the drive amplifier to eliminate DC voltage drifts. However, the use of recent low drift operational amplifiers in these key locations gave satisfactory results. Shifts in the zero velocity channel positions were within .015 mm/sec per month, while trimming to eliminate the DC offset drifts had to be performed only once every one to two months.

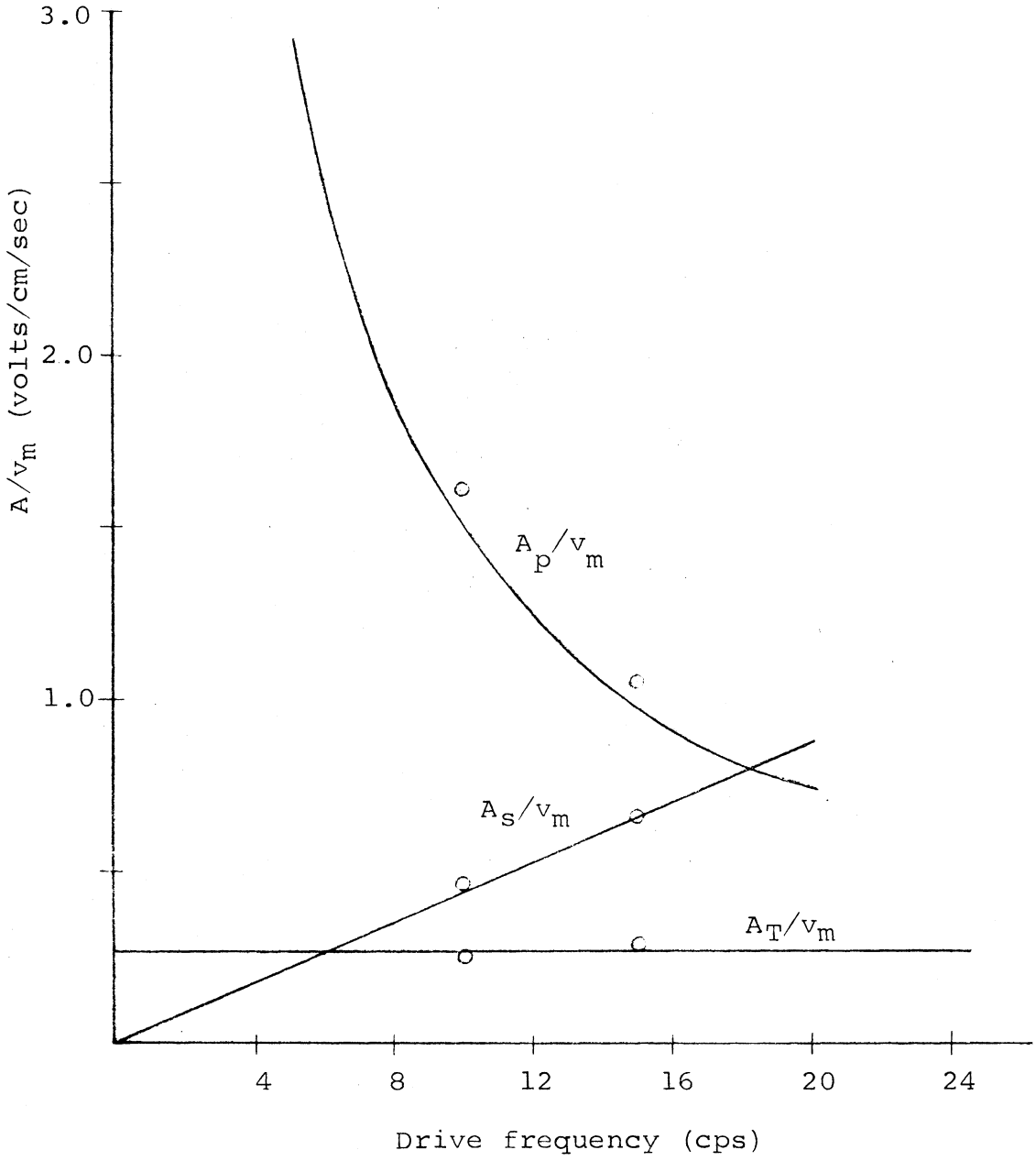

Figure C-1. Waveform amplitudes required to give drive transducer a triangular velocity response versus frequency.

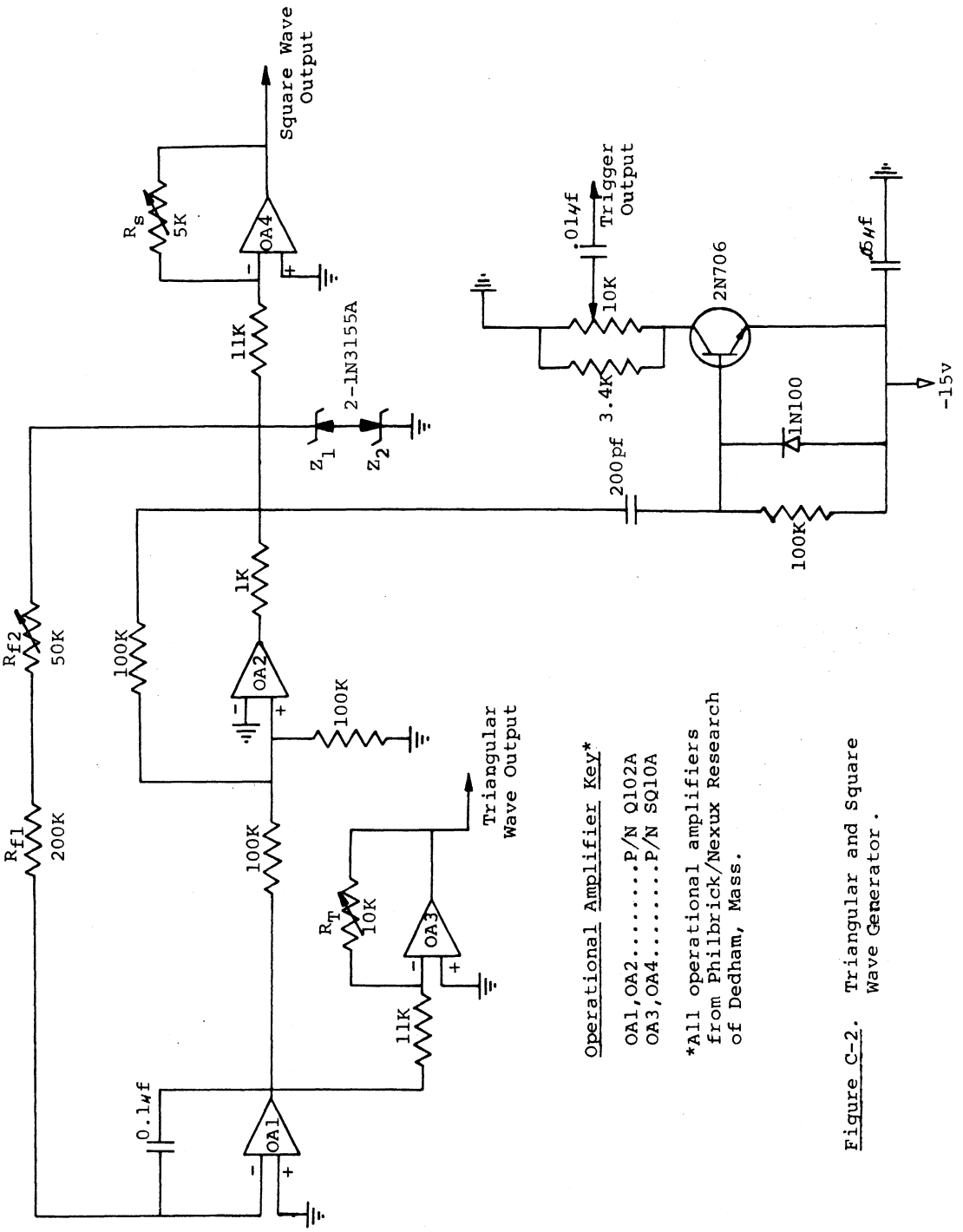

Operational Amplifier Key*

OA1,OA2.....P/N Q102A
OA3,OA4.....P/N SQ10A

*All operational amplifiers from Philbrick/Nexux Research of Dedham, Mass.

Figure C-2. Triangular and Square Wave Generator.

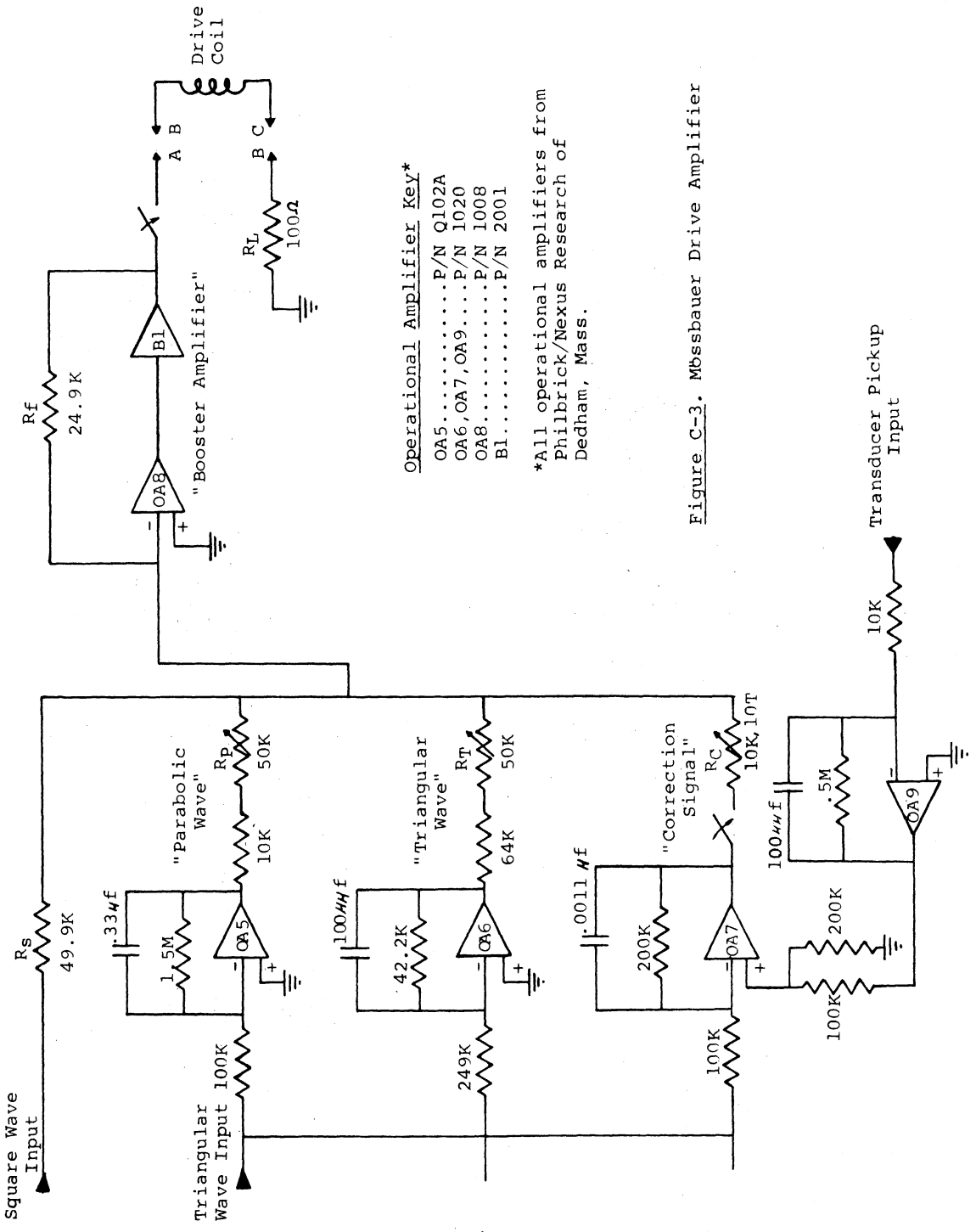

Operational Amplifier Key*

OA5.....P/N Q102A
OA6,OA7,OA9....P/N 1020
OA8.....P/N 1008
B1.....P/N 2001

*All operational amplifiers from Philbrick/Nexus Research of Dedham, Mass.

Figure C-3. Mössbauer Drive Amplifier

B. Commercial Components Used in Mössbauer Spectrometer System

Pickup Calibrator/Exciter

Model: C31, MB Electronics, New Haven, Connecticut.

Multichannel Analyzer

Model: ND-180FM, Nuclear Data, Inc., Palatine, Illinois.

Time Base Generator

Model: ND-180ITB, Nuclear Data, Inc., Palatine, Illinois.

Oscilloscope

Type 503, Tektronix, Inc., Beaverton, Oregon.

Teletype

Model: 33TC, Teletype Corporation, Skokie, Illinois.

Kr-CO_2 Proportional Counter

Model: RSG-61-M1, Reuther-Stokes Electronic Components, Inc., Cleveland, Ohio.

High Voltage Supply

Model: HV-1544, Power Designs Pacific, Inc., Palo Alto, California.

Preamplifier

Model: 109PC, Ortec, Incorporated, Oak Ridge, Tennessee.

Linear Amplifier

Model 451, Ortec, Incorporated, Oak Ridge, Tennessee.

Single Channel Analyzer

Model: NC-15, Hamner Electronics Corporation, Princeton, New Jersey.

APPENDIX D

DATA ANALYSIS DETAILS

A. Description of Programs

As summarized in Chapter III, the experimental Mössbauer data are fit to a sum of distribution functions by a non-linear least squares fitting program similar to other published programs.[37,120] The method used for finding the set of parameters which minimizes chi-square is the Gauss-Newton iteration method.[119] The resonant lines are fit to a combination of Lorentzian functions or Gaussian-distributed Lorentzians, while the non-resonant background is fit to a parabola. These functions, as well as their partial derivatives with respect to the fitting parameters, are supplied to the main program, which performs the least squares analysis, by special sub-programs named THEORY. The partial derivatives are used to set up the "normal equations" whose solutions are the parameter increments for the next iteration.

The functions performed by the main program and its supportive subroutines include the following: the main program reads in the control and fitting parameters, sets up the normal equations, determines convergence, calculates and prints out the fitting parameters and their standard deviations, and also provides the input data for the Calcomp plotting program. The subroutine DREAD reads the input data (usually from a file where the MCA paper-tape output is stored) and makes background corrections if required. At present a maximum of 25 parameters

may be fitted to a spectrum consisting of 512 data points. The normal equations are solved by a linear systems subprogram called DPINVS. The inverted coefficient matrix of the normal equations, called the error matrix, is also supplied by DPINVS. In addition to THEORY, there exists a unique subprogram TAREA for each function being fit. TAREA calculates the area of each line or pair of lines and its standard deviation, and also determines the ratios of these areas and the ratios' errors.

The printed output includes the fitting parameters and the normalized χ^2 after each iteration; the final parameter values and their standard deviations; the total and individual resonant line areas; the distribution in units of standard deviation of errors between the measured and fitted spectrum; and an area ratio matrix containing the ratios of individual line areas as off-diagonal elements and individual to total areas along the diagonal. As an option, the error correlation matrix can also be provided. The Calcomp program plots the normalized experimental data and fitted function on the same graph as well as a distribution of their differences on a separate graph.

The main data analysis program, its subroutines and the Calcomp plotting program are listed in Section C of this Appendix. All programs were written in the Fortran IV language. Only the two THEORY subprograms (plus TAREA) used most often in fitting the data are listed. Other THEORY subprograms used to provide special constraints on the fitting parameters involved only minor modifications of these two general subprograms, and therefore, are not listed.

B. The Fitting of Gaussian-Lorentzian Convolution Functions

Gaussian-distributed Lorentzians are used to account for the small variations in isomer shifts and quadrupoles splittings that occur when the Fe^{57} nuclei experience a distribution of local Fe configurations. For solid solution Fe these configurations involve further than nearest neighbors, while for Fe in clusters both nearest and distant neighbors are involved.

The fitting of the G-L convolution function by the Gauss-Newton iteration scheme requires that its value and the value of its partial derivatives be calculated for each velocity or channel number. Unlike the Lorentzian function, the distribution function of Equation (III.4) can not be obtained in closed form. The function and its derivatives must be calculated numerically for each data point. How this has been accomplished is described below.

The first step is to recognize that the G-L convolution $d_j(v)$, in Equation (III.4) can be expressed in terms of the real part of the complex error function;[124] i.e., the real part of

$$w(z) = \left(\frac{i}{\pi}\right)\int_{-\infty}^{\infty}\frac{e^{-s^2}}{z-s}ds \qquad (D.1)$$

or, its more common form

$$w(z) = e^{-z^2}\left[1 + \frac{2i}{\sqrt{\pi}}\int_{\infty}^{\infty}e^{t^2}dt\right] \qquad (D.2)$$

where $z = x+iy$. To accomplish this consider the following variable transformations in Equation (III.4):

$$s = \frac{v'-v_j}{\theta_j}, \quad x_j = \frac{v-v_j}{\theta_j}, \quad y_j = \frac{\Gamma}{2\theta_j}. \qquad (D.3)$$

Making these transformations, the G-L convolution becomes

$$d_j(v) = \frac{A_j}{\pi\sqrt{\pi\theta_j}} \int_{-\infty}^{\infty} \frac{y_j e^{-s^2}}{(x_j-s)^2+y_j^2} ds \ . \qquad (D.4)$$

To see the relationship between $d_j(v)$ and Re[w(z)], Equation (D.1) can be rewritten as

$$w(z) = \frac{1}{\pi} \int_{-\infty}^{\infty} \frac{y e^{-s^2}}{(x-s)^2+y^2} ds + \frac{i}{\pi} \int_{-\infty}^{\infty} \frac{(x-s) e^{-s^2}}{(x-s)^2+y^2} ds \qquad (D.5)$$

or,

$$w(z) = R(x,y) + iI(x,y) \qquad (D.6)$$

where R(x,y) and I(x,y) are the real and imaginary parts of w(z). Comparison of Equations (D.4), (D.5) and (D.6) then leads to

$$d_j(v) = \frac{A_j}{\sqrt{\pi\theta_j}} R(x_j,y_j) \qquad (D.7)$$

which is the desired result.

Thus, the required resonant line function, $d_j(v)$, is directly proportional to the real part of the complex error function which can readily be evaluated by existing numerical techniques. For this purpose, the subroutine COMER* is used. COMER evaluates both the real and imaginary parts of w(z) for arguments z = x+iy in the first quadrant of the complex plane. Using the symmetry relations R(x,y) = R(-x,y) and I(-x,y) = -I(x,y), the functions can be evaluated in all four

---

*Obtained from the Computing Technology Center, Union Carbide Corporation, Oak Ridge, Tennessee.

quadrants. The recursive procedure used to calculate w(z) in COMER is described by Gautschi.[125]

In addition to the function $d_j(v)$, the partial derivatives--$\frac{\partial d_j}{\partial A_j}$, $\frac{\partial d_j}{\partial v_j}$ and $\frac{\partial d_j}{\partial \theta_j}$ --are also required in the fitting procedure. These partial derivatives can be expressed in terms of R(x,y) and I(x,y), and thus can also be evaluated using COMER. The expressions for the derivatives can be obtained either directly from Equation (D.4) or by using Equation (D.7) and the expression for the total derivative of w(z). The latter approach involves less algebra and is given below.

From Equations (D.7) and (D.3) the required partials are

$$\frac{\partial d_j(v)}{\partial A_j} = \frac{1}{\sqrt{\pi}\theta} R(x_j, y_j) \ , \tag{D.8a}$$

$$\frac{\partial d_j(v)}{\partial v_j} = \frac{A_j}{\sqrt{\pi}\theta_j} \frac{\partial R}{\partial v_j} = \frac{A_j}{\sqrt{\pi}\theta_j} \frac{\partial R}{\partial x_j} \frac{\partial x_j}{\partial v_j}$$

$$= \frac{-A_j}{\sqrt{\pi}\theta_j^2} \frac{\partial R}{\partial x_j} \ , \tag{D.8b}$$

and

$$\frac{\partial d_j(v)}{\partial \theta_j} = \frac{A_j}{\sqrt{\pi}} \left| -\frac{1}{\theta_j^2} R + \frac{1}{\theta_j} \left[\frac{\partial R}{\partial x_j} \frac{\partial x_j}{\partial \theta_j} + \frac{\partial R}{\partial y_j} \frac{\partial y_j}{\partial \theta_j} \right] \right|$$

$$= \frac{-A_j}{\sqrt{\pi}\theta_j^2} \left[R + x_j \frac{\partial R}{\partial x_j} + y_j \frac{\partial R}{\partial y_j} \right] \ . \tag{D.8c}$$

Only the first expression, (D.8a) above, is in final form; the others involve the partial derivatives $\frac{\partial R}{\partial x_j}$ and $\frac{\partial R}{\partial y_j}$ which can be determined from

the derivative of w(z). From the second form for w(z) given by Equation (D.2)

$$w'(z) = \frac{2i}{\sqrt{\pi}} - 2zw(z)$$

$$= 2[yI(x,y)-xR(x,y)]$$

$$+2i\left[\frac{1}{\sqrt{\pi}} - xI(x,y)-yR(x,y)\right] \qquad (D.9)$$

where use has been made of Equation (D.6). Making use of the fact that w(z) is analytic and applying the Cauchy-Riemann conditions (i.e., $\frac{\partial R}{\partial x} = \frac{\partial I}{\partial y}$ and $\frac{\partial R}{\partial y} = \frac{-\partial I}{\partial x}$), the partial derivatives $\frac{\partial R}{\partial x}$ and $\frac{\partial R}{\partial y}$ can be obtained directly from Equation (D.9) and are given by

$$\frac{\partial R}{\partial x_j} = 2[y_j I(x_j,y_j)-x_j R(x_j,y_j)] \qquad (D.10)$$

and

$$\frac{\partial R}{\partial y_j} = -2[\frac{1}{\sqrt{\pi}} - x_j I(x_j,y_j)-y_j R(x_j,y_j)] \ . \qquad (D.11)$$

Combining the results of Equations (D.8b) and (D.8c) with Equations (D.10) and (D.11) above, leads to the desired expressions for $\frac{\partial d_j}{\partial v_j}$ and $\frac{\partial d_j}{\partial \theta_j}$:

$$\frac{\partial d_j(v)}{\partial v_j} = \frac{2A_j}{\sqrt{\pi}\theta_j^2}[x_j R(x_j,y_j)-y_j I(x_j,y_j)] \qquad (D.12)$$

$$\frac{\partial d_j(v)}{\partial \theta_j} = \frac{2A_j}{\sqrt{\pi}\theta_j^2}\left[(x_j^2-y_j^2-\frac{1}{2})R(x_j,y_j)-2x_j y_j I(x_j,y_j) + \frac{y_j}{\sqrt{\pi}}\right] \qquad (D.13)$$

The expression for $\frac{\partial d_j}{\partial A_j}$ is given by Equation (D.8a).

The proportionality between the G-L convolution integral and its partial derivatives with either the real or imaginary parts of the complex error function allows their evaluation by existing numerical methods. The subroutine COMER, which is listed in Section C of this Appendix, is used to evaluate these functions in conjunction with the THEORY subroutine.

C. Listing of Mössbauer Computer Programs

1. Main Program

```
C     MOSFIT PROGRAM
      INTEGER SP,P3S,P2S,P1S,POS,IP(8)
      REAL*4 INCR
      REAL*8 SETUP(18),P(25),REF,X(512),AM(25,25),DP(25),WT,DIF,BZ,
     1AZ,DF(25),AV(25,25),C(25),PS(25),FYI,Q
      DIMENSION FYJ(512,8),FY(512),YNRM(512),FIT(512),XV(512),
     1CVR(25,25),YS(512),SIG(25),VR(25),DIFF(512),BN(8)
      COMMON/CONTR/M,NS,NP,NB,NL,NK,IUP,ILP,IS
      COMMON/DATA/YS,ADDC,MM,IM,IDT,JDT
      COMMON/LIN/AM,AV,DP
      COMMON/PAR/FYI,BN,PX1,PX2,PX3,PX4,VCAL,RZP
      COMMON/AREAS/P,CVR,VR,AREA,ARS
C     IGNORE BLANCS ON INPUT
      CALL FCVTHB(1)
      IPR=6
      IRD=5
C     READ AND PRINT DATA
  952 FORMAT('1',7A8/7A8//14HVELOCITY CAL= ,F8.5,
     110H MM/SEC/CH,3X,6H ZERO=,F8.3,7H CH VS ,A8/I4,9H CHANNELS
     2,3X,I3,11H PARAMETERS,3X,I3,13H SINGLE LINES,3X,I3,4H PRS)
  125 READ(IRD,901,END=100)(SETUP(I),I=1,14),REF,MM,
     1NDECKS,M,NS,NP,NB,IDT,LPL,KSC,ICAL,IDIF,ILP,IUP,IMIN,IMAX,
     2YM,YMX,SFX,SFY,FF,CON
  901 FORMAT(7A8/7A8/A8,2I3/9I3/4I4/4F5.3/2F6.0)
      JDT=0
    1 READ(IRD,902)RZP,VCAL,PX1,PX2,PX3,PX4
  902 FORMAT(6F8.0)
      READ(IRD,905)(P(I),I=1,M)
  905 FORMAT(7F8.0)
    2 CALL DREAD
C     CHECK FOR PROPER CONDITIONS FOR ANALYSIS
      IF(M.GT.0.AND.M.LE.25)GO TO 4
      WRITE(IPR,907)M
  907 FORMAT('0',20X,48HONLY 1 TO 25 FITTING PARAMETERS ARE ALLOWED, NOT
     1,I3)
      GO TO 125
    4 IF(IM.LE.512)GO TO 5
      WRITE(IPR,908)IM
  908 FORMAT('0',20X,42HONLY 1 TO 512 DATA POINTS ARE ALLOWED, NOT,I3)
      GO TO 125
    5 CONTINUE
C     SETTING UP NORMAL EQUATIONS
      DO 500 I=1,IM
  500 X(I)=DFLOAT(I)
      WRITE(IPR,952)(SETUP(I),I=1,14),VCAL,RZP,REF,IM,M,NS,NP
      WRITE(IPR,951)
  951 FORMAT('0',24X,'INTERMEDIATE RESULTS'/1X,'ITERATION',2X,'CHISQ/NN
     1',19X,'PARAMETERS')
```

```
      JIT=0
      KIT=0
      NK=0
      Q=DBLE(FF)
    7 WVAR=0.
      DO 8 K=1,M
      C(K)=0.0
      DO 8 L=1,M
    8 AM(K,L)=0.0
      DO 9 I=ILP,IUP
      CALL THEORY(X(I),P,AZ,BZ,F,DF)
      WT = 1.0/DBLE(YS(I))
      DIF=DBLE(YS(I)-F)
      WVAR=WVAR+WT*DIF**2
      DO 9 K=1,M
      C(K)=C(K)+WT*DIF*DF(K)
      DO 9 L=1,M
    9 AM(K,L)=AM(K,L)+WT*DF(K)*DF(L)
      CHISQ=WVAR/(IUP-ILP-M)
      NK=0
      WRITE(IPR,911) JIT,CHISQ,(P(I),I=1,M)
  911 FORMAT('0',3X,I3,4X,E14.6,2X,3D14.6/(27X,3D14.6))
C     TEST FOR CONDITIONS OF ITERATION
      IF(CHISQ.GT.500.0) GO TO 99
      IF(JIT.EQ.0) GO TO 10
      ABV=ABS(WVAR-VC)
      IF(ABV.LE.CON) GO TO 22
      IF(KIT.EQ.0 .AND. WVAR.GT.VO) GO TO 18
      IF(KIT.EQ.1 .AND. WVAR.GT.VO) GO TO 21
      IF(JIT-20.EQ.0) GO TO 21
C     SOLUTION OF EQUATIONS
   10 CONTINUE
      DO 11 K=1,M
   11 DP(K)=C(K)
      CALL DPINVS(M,-1,ISIG)
      IF(ISIG.NE.0) GO TO 100
C     CHECK VALUES OF ITERATION
      CD=0.0
      DO 14 K=1,M
   14 CD=CD+C(K)*DP(K)
      IF(CD.GT.0) GO TO 16
      DO 15 K=1,M
   15 DP(K)=-DP(K)
      WRITE(IPR,925)
  925 FORMAT('0',3X,'VECTOR PRODUCT NEGATIVE')
   16 CONTINUE
      DO 17 K=1,M
      PS(K)=P(K)
      DP(K)=Q*DP(K)
   17 P(K)=P(K)+DP(K)
      VO=WVAR
      JIT=JIT+1
      KIT=0
      GO TO 7
   18 CONTINUE
      DO 180 K=1,M
      P(K)=PS(K)
  180 PS(K)=PS(K)+DP(K)/2.
```

```
      V1=0.0
      DO 185 I=ILP,IUP
      CALL THEORY(X(I),PS,AZ,BZ,F,DF)
      WT=1./DBLE(YS(I))
      DIF=DBLE(YS(I)-F)
  185 V1=V1+WT*DIF**2
      V2=(WVAR+V0)/2.
      IF(V1.GT.V2) GO TO 20
      ALPHA=.5*(WVAR-4.*V1+3.*V0)/(2.*WVAR-4.*V1+2.*V0)
      WRITE(IPR,912) ALPHA
  912 FORMAT(10X,'ALPHA=',1X,F6.4)
      DO 19 K=1,M
   19 P(K)=P(K)+ALPHA*DP(K)
      KIT=1
      JIT=JIT+1
      NK=0
      GO TO 7
C TERMINATION OF ITERATION
   20 WRITE(IPR,913)
  913 FORMAT('0',5X,'FURTHER ITERATION UNSUCCESSFUL')
      GO TO 80
   21 WRITE(IPR,914)
  914 FORMAT('0',10X,'CONVERGENCE CRITERIA NOT MET')
      IF(JIT.GT.4) GO TO 22
      GO TO 80
   22 WRITE(IPR,915)
  915 FORMAT('0',10X,'FINAL RESULTS')
C     NORMALIZATION OF DATA & CALCULATION OF AREAS
      AREA=0.0
      ARS=0.0
      DO 25 I=ILP,IUP
      CALL THEORY(X(I),P,AZ,BZ,F,DF)
      FIT(I)=BZ
      YNRM(I)=YS(I)/AZ
      DIFF(I)=YNRM(I)-FIT(I)
      AREA=AREA-YNRM(I)+1.0
      ARS=ARS-FIT(I)+1.0
       DO 24 J=1,NL
   24 FYJ(I,J)=BN(J)
   25 FY(I)=FYI

C     CALCULATION OF ERRORS
      WRITE(IPR,930) CHISQ
  930 FORMAT('0',5X,'FINAL CHISQ/NN=',2X,E14.6)
      CALL DPINVS(M,0,ISIG)
      IF(ISIG.NE.0) GO TO 100
      DO 26 K=1,M
      VR(K)=CHISQ*DABS(AV(K,K))
      SIG(K)=SQRT(VR(K))
      DO 26 L=1,M
      CVR(K,L)=CHISQ*AV(K,L)
   26 CVR(L,K)=CVR(K,L)
```

```
C     ERROR DISTRIBUTION
      SD=DSQRT(AZ)/AZ
      P3S=0
      P2S=0
      P1S=0
      P0S=0
      N0S=0
      N1S=0
      N2S=0
      N3S=0
      DO 27 I=ILP,IUP
      IF (DIFF(I).GT.SD*3.0)P3S=P3S+1
      IF (DIFF(I).GT.SD*2.0.AND.DIFF(I).LT.SD*3.0)P2S=P2S+1
      IF (DIFF(I).GT.SD*1.0.AND.DIFF(I).LT.SD*2.0)P1S=P1S+1
      IF (DIFF(I).GT.0.0.AND.DIFF(I).LT.SD*1.0)P0S=P0S+1
      IF (DIFF(I).GT.-SD*1.0.AND.DIFF(I).LT.0.0)N0S=N0S+1
      IF (DIFF(I).GT.-SD*2.0.AND.DIFF(I).LT.-SD*1.0)N1S=N1S+1
      IF (DIFF(I).GT.-SD*3.0.AND.DIFF(I).LT.-SD*2.0)N2S=N2S+1
   27 IF (DIFF(I).LT.-SD*3.0)N3S=N3S+1
C     DATA PRINT OUT
      WRITE(IPR,917)
  917 FORMAT('0',20X,'FITTING PARAMETERS')
      DO 30K=1,M
   30 WRITE(IPR,918)K,P(K),SIG(K)
  918 FORMAT(' ',3X,I3,10H PARAMETER,2X,
     1D15.6,4H +- ,E15.6)
      WRITE(IPR,919) P3S,P2S,P1S,P0S,N0S,N1S,N2S,N3S
  919 FORMAT('0',5X,18HERROR DISTRIBUTION,8I5)

C       CALCULATION OF AREAS THRU SUB TAREA
      CALL TAREA
      IF(LPL.NE.1) GO TO 37
      WRITE(IPR,920)
  920 FORMAT('0',5X,'COVARIANCE ELEMENTS FROM ERROR
     1MATRIX'//)
      DO 35 K=1,M
      KP1=K+1
      WRITE(IPR,922)(CVR(K,L),L=KP1,M)
  922 FORMAT(' ',2X,6(E10.3,1X))
      WRITE(IPR,923)
  923 FORMAT(' ')
   35 CONTINUE
   37 CONTINUE
      IF(LPL.EQ.-1 .AND. JDT.EQ.0) GO TO 80
C       PRINT OUT FOR CALCOMP PLOT PROGRAM
      IF(JDT.EQ.1) GO TO 125
  970 FORMAT(' ',4F7.3,2F9.4/5I3,4I4)
  971 FORMAT(' ',10F8.4)
      WRITE(7,970)SFX,SFY,YM,YMX,RZP,VCAL,NL,KSC,ICAL,IDIF,
     1IM,IMIN,IMAX,IUP,ILP
      WRITE(7,971)(FY(I),I=1,IM)
      WRITE(7,971)(YNRM(I),I=1,IM)
      WRITE(7,971)(FIT(I),I=1,IM)
      WRITE(7,971)(DIFF(I),I=1,IM)
```

```
      DO 320 K=1,NL
  320 WRITE(7,971)(FYJ(J,K),J=1,IM)
   80 IF(IDT)125,125,81
   81 JDT=1
      GO TO 1
   99 WRITE(IPR,921)
  921 FORMAT('3','  CHISQ GREATER THAN 500 _ THEORY INCORRECT OR
     1ESTIMATES VERY BAD')
  100 CALL SYSTEM
      END


      SUBROUTINE DREAD
C     READ AND ARRANGE MCA DATA
      DIMENSION Y(512),YS(512),YZ(512)
      COMMON/DATA/YS,ADDC,MM,IM,IDT,JDT
  100 FORMAT(F8.0)
  101 FORMAT(8(F6.0,2X))
      IF(JDT.EQ.1) GO TO 50
      IF(IDT)3,3,5
    3 IM=MM
      GO TO 10
    5 IM=MM/2
   10 DO 15 I=1,MM
   15 YZ(I)=0.0
      READ(5,100)ADDC
      DO 20 J=1,NDECKS
      READ(4,101)(Y(I),I=1,MM)
      DO 20 I=1,MM
   20 YZ(I)=-YZ(I)+Y(I)+ADDC
      IF(IDT)30,25,25
   25 DO 26 I=1,IM
      LM=1+IM-I
   26 YS(I)=YZ(LM)
      GO TO 80
   30 DO 35 I=1,IM
   35 YS(I)=YZ(I)
      GO TO 80
   50 DO 55 I=1,IM
      KM=IM+I
   55 YS(I)=YZ(KM)
   80 CONTINUE
      RETURN
      END
```

2. Theory Subprograms for Lorentzian Functions.

```
      SUBROUTINE THEORY(XT,PT,AT,BT,FT,DFT)
C      THEORY FOR NS INDIV LINES + NP PAIRS OF EQUAL LINES CENTERED AT
C      SAME CENTROID. MAX. NO. LINES + PAIRS = NL
C      J=INDIV. LINE NO, K=PAIR NO.    JMAX=NS,KMAX=NP+NS, KMIN=NS+1
C      INDIV LINE PARAMS. P(3*J-2)=POS., P(3*J-1)=INT., P(3*J)=GAM/2
C      PAIR PARAMETERS. P(3*NS+1)=CENT., P(3*K-1)=SPLIT, P(3*K)=INT.
C         P(3*K+1)=GAM/2
C      BKGRD. PARAM. NP=0. P(3*NS+1)=CONST, P(3*NS+2)=LIN. COEF.,
C         P(3*NS+3)=QUAD. COEF.
C      BKGRD PARAM. NP.NE.0    P(3*NL+2)=CONST, P(3*NL+3)=LIN. COEF.
C         P(3*NL+4)=QUAD.COEF.
C      TYPE OF BKGRD: NB=-1(LIN); NB=0(CONST); NB=1(QUADRATIC).
      IMPLICIT REAL*8 (A-H,O-Z)
      REAL*4 FT,BI(8),PX1,PX2,PX3,PX4,VCAL,RZP
      DIMENSION PT(25), DFT(25)
      COMMON/PAR/BS,BI,PX1,PX2,PX3,PX4,VCAL,RZP
      COMMON/CONTR/M,NS,NP,NB,NL,NK,IUP,ILP,IS
      BS=1.0
      IF(NK.EQ.1) GO TO 6
      NL=NS+NP
      NL3=3*NL
      NS3=3*NS
    4 AT=PT(NL3+1)
      IF(NP.NE.0) AT=PT(NL3+2)
    6 CONTINUE
      IF(NS.EQ.0) GO TO 30
C      INDIVIDUAL LINES' FUNCTIONS AND DERIVATIVES
      DO 20 J=1,NS
      JJ=3*J
      XO=PT(JJ-2)
      G=PT(JJ)
      G2=G*G
      T=PT(JJ-1)
      C=T*G2
      Z=XT-XO
      D=Z*Z+G2
      BI(J)=1.0-C/D
      BS=BS-C/D
      DFT(JJ-2)=-2.0*AT*C*Z/(D*D)
      DFT(JJ-1)=-AT*G2/D
   20 DFT(JJ)=-2.0*AT*G*((T*D-C)/(D*D))
      IF(NP.EQ.0) GO TO 50
   30 DFT(NS3+1)=0.0
      NSS=NS+1
C      PAIR FUNCTIONS AND DERIVATIVES
      DO 40 K=NSS,NL
      KK=3*K
      XL=PT(NS3+1)-.5*PT(KK-1)
      XR=PT(NS3+1)+.5*PT(KK-1)
      T=PT(KK)
      G=PT(KK+1)
      G2=G*G
      C=T*G2
```

```
      ZL=XT-XL
      ZR=XT-XR
      DL=ZL*ZL+G2
      DR=ZR*ZR+G2
      BI(K)=1.0-C/DL-C/DR
      BS=BS-C/DL-C/DR
      DFT(NS3+1)=DFT(NS3+1)-2.0*AT*C*(ZL/(DL*DL)+ZR/(DR*DR))
      DFT(KK-1)=AT*C*(ZL/(DL*DL)-ZR/(DR*DR))
      DFT(KK)=-AT*(G2/DL+G2/DR)
   40 DFT(KK+1)=-2.0*G*((T*DL-C)/(DL*DL)+(T*DR-C)/(DR*DR))*AT
      GO TO 80
C      BACKGROUND
   50 CONTINUE
      IF(NB)55,65,60
   55 BT=BS+PT(NS3+2)*XT
      DFT(NS3+2)=AT*XT
      GO TO 70
   60 BT=BS+PT(NS3+2)*XT +PT(NS3+3)*XT*XT
      DFT(NS3+2)=AT*XT
      DFT(NS3+3)=AT*XT*XT
      GO TO 70
   65 BT=BS
   70 DFT(NS3+1)=BT
      GO TO 99
   80 CONTINUE
      IF(NB)85,95,90
   85 BT=BS+PT(NL3+3)*XT
      DFT(NL3+3)=AT*XT
      GO TO 96
   90 BT=BS+PT(NL3+3)*XT+PT(NL3+4)*XT*XT
      DFT(NL3+3)=AT*XT
      DFT(NL3+4)=AT*XT*XT
      GO TO 96
   95 BT=BS
   96 DFT(NL3+2)=BT
   99 FT=AT*BT
      NK=1
      RETURN
      END



      SUBROUTINE TAREA
C      AREAS, RATIOS OF AREAS AND ERRORS
C      FOR LORENTZIAN SINGLETS AND/OR DOUBLETS
      REAL*8 P(25)
      REAL*4 AA(8,8),RSG(8,8),CVR(25,25),VR(25),AR(8),SGA(8),VRA(8)
      DIMENSION IP(8)
      COMMON/CONTR/M,NS,NP,NB,NL,NK,IUP,ILP,IS
      COMMON/AREAS/P,CVR,VR,AREA,ARS
      VRT=0.0
      IPR=6
      IF(NS.EQ.0) GO TO 272
      DO 271 I=1,NS
      II=3*I
      I1=II-1
      AR(I)=3.14159*P(II)*P(I1)
      ARE=ARE+AR(I)
```

```
      VRA(I)=AR(I)*AR(I)*(VR(I1)/(P(I1)*P(I1))+
     1VR(II)/(P(II)*P(II))+2*CVR(II,I1)/(P(II)*P(I1)))
      SGA(I)=SQRT(VRA(I))
  271 VRT=VRT+VRA(I)
      IF(NP.EQ.0) GO TO 280
  272 NS1=NS+1
      DO 273 K=NS1,NL
      KK=3*K
      K1=KK+1
      AR(K)=6.28318*P(KK)*P(K1)
      ARE=ARE+AR(K)
      VRA(K)=AR(K)*AR(K)*(VR(KK)/(P(KK)*P(KK))+
     1VR(K1)/(P(K1)*P(K1))+2*CVR(K1,KK)/(P(K1)*P(KK)))
      SGA(K)=SQRT(VRA(K))
  273 VRT=VRT+VRA(K)
  280 CONTINUE
      IF(NS.EQ.0) GO TO 292
      DO 291 I=1,NS
      II=3*I
      I1=II-1
      IZ=I+1
      IF(IZ.GT.NS) GO TO 292
      DO 291 J=IZ,NS
      JJ=3*J
      J1=JJ-1
      VRT=VRT+2*AR(I)*AR(J)*(CVR(I1,J1)/(P(I1)*P(J1))+
     1CVR(I1,JJ)/(P(I1)*P(JJ))+CVR(II,JJ)/(P(II)*P(JJ)))
      AA(I,J)=AR(I)/AR(J)
      AA(J,I)=AR(J)/AR(I)
      RV=VRA(I)/(AR(I)*AR(I))+VRA(J)/(AR(J)*AR(J))
     1-2*CVR(I1,J1)/(P(I1)*P(J1))-2*CVR(I1,JJ)/(P(I1)*P(JJ))
     2-2*CVR(II,J1)/(P(II)*P(J1))-2*CVR(II,JJ)/(P(II)*P(JJ))
      RSG(I,J)=AA(I,J)*SQRT(RV)
  291 RSG(J,I)=AA(J,I)*SQRT(RV)
  292 NS1=NS+1
      IF(NP.EQ.0) GO TO 297
      DO 296 K=NS1,NL
      KK=3*K
      K1=KK+1
      KZ=K+1
      IF(KZ.GT.NL) GO TO 294
      DO 293 L=KZ,NL
      LL=3*L
      L1=LL+1
      VRT=VRT+2*AR(K)*AR(L)*(CVR(K1,L1)/(P(K1)*P(L1))+
     1CVR(K1,LL)/(P(K1)*P(LL))+CVR(KK,LL)/(P(KK)*P(LL)))
      AA(K,L)=AR(K)/AR(L)
      AA(L,K)=AR(L)/AR(K)
      RV=VRA(K)/(AR(K)*AR(K))+VRA(L)/(AR(L)*AR(L))-2*
     1CVR(K1,LL)/(P(K1)*P(LL))-2*CVR(K1,L1)/(P(K1)*P(L1))
     2-2*CVR(KK,LL)/(P(KK)*P(LL))-2*CVR(KK,L1)/(P(KK)*P(L1))
      RSG(K,L)=AA(K,L)*SQRT(RV)
  293 RSG(L,K)=AA(L,K)*SQRT(RV)
  294 CONTINUE
```

```
      IF(NS.EQ.0) GO TO 296
      DO 295 I=1,NS
      II=3*I
      I1=II-1
      VRT=VRT+2*AR(I)*AR(K)*(CVR(I1,K1)/(P(I1)*P(K1))+
     1CVR(I1,KK)/(P(I1)*P(KK))+CVR(II,K1)/(P(II)*P(K1))+
     2CVR(II,KK)/(P(II)*P(KK)))
      AA(I,K)=AR(I)/AR(K)
      AA(K,I)=AR(K)/AR(I)
      RV=VRA(I)/(AR(I)*AR(I))+VRA(K)/(AR(K)*AR(K))-2*
     1CVR(I1,K1)/(P(I1)*P(K1))-2*CVR(I1,KK)/(P(I1)*P(KK))
     2-2*CVR(II,K1)/(P(II)*P(K1))-2*CVR(II,KK)/(P(II)*P(KK))
      RSG(I,K)=AA(I,K)*SQRT(RV)
  295 RSG(K,I)=AA(K,I)*SQRT(RV)
  296 CONTINUE
  297 SGAT=SQRT(VRT)
      DO 298 J=1,NL
      AA(J,J)=AR(J)/ARE
      RVD=1.5*(VRA(J)/(AR(J)*AR(J))+VRT/(ARE*ARE))
  298 RSG(J,J)=AA(J,J)*SQRT(RVD)
      WRITE(IPR,960)AREA,ARS,ARE,SGAT
  960 FORMAT('0',5X,'EXPER. AREA=',F12.4//6X,'FIT AREA=',
     1F10.4//6X,'BKGRD CORRECTED AREA=',F10.4,2X,'+-',F7.4)
      WRITE(IPR,961)
  961 FORMAT('0',5X,'INDIVIDUAL LINE AND OR PAIR AREAS'//10X,'LINE NUMBE
     1R')
      DO 962 J=1,NL
  962 WRITE(IPR,963)J,AR(J),SGA(J)
  963 FORMAT(' ',13X,I3,3X,E15.6,4H +- ,E15.6)
      DO 302 K=1,NL
  302 IP(K)=K
      WRITE(IPR,964)(IP(K),K=1,NL)
  964 FORMAT('0',5X,'AREA FRACTION MATRIX'//7X,'1)RATIO OF AREA OF ONE P
     1EAK TO TOTAL AREA ON DIAGONAL'//7X,'2)RATIO OF AREAS OF ANY PAIR O
     2F PEAKS OFF DIAGONAL'///2X,'PEAK(S)',10I7)
      DO 303 K=1,NL
  303 WRITE(IPR,965)K,(AA(K,L),L=1,NL)
  965 FORMAT('0',1X,I3,8X,8F7.3)
      WRITE(IPR,966)(IP(K),K=1,NL)
  966 FORMAT('0',5X,'AREA FRACTION ERRORS'//2X,'PEAK(S)',
     110I7)
      DO 305 K=1,NL
  305 WRITE(IPR,965)K,(RSG(K,L),L=1,NL)
      RETURN
      END
```

3. Theory Subprograms for Gaussian-Distributed Lorentzian Functions.

```
      SUBROUTINE THEORY(XT,PT,AT,BT,FT,DFT)
C     NN GAUSIAN-LORENTZIAN CONVOLUTED FITTING FCNS. PLUS
C    (NB=1) ONE LORENTZIAN CONSTR. IN POSITION (PX1) ONLY
C    OR (NB=2) ONE CONVOLUTED GAUSSIAN-LORENTZIAN
C    CONSTR. IN POS. (PX1). FIXED LORENTZIAN WIDTH
C    IN CONVOLUTION FCN. IS W/2=PX2. PARAMETERS FOR
C    UNCONSTR. G-L LINES: POS=PT(3*J-2), AREA=PT(3*J-1),
C    GAUSSIAN WITH=PT(3*J).  BACKGROUND EQUATION:
C    PT(M-2)+PT(M-1)*X+PT(M)*X**2.
      IMPLICIT REAL*8(A-H,Q-Z)
      REAL*4 VCAL,RZP,FT,BI(8)
      REAL*8 IM,PX,PY,PZ,PT(25),DFT(25)
      COMMON/CONTR/M,NS,NP,NB,NL,NK,IUP,ILP,IS
      COMMON/PAR/BS,BI,PX1,PX2,PX3,PX4,VCAL,RZP
      BS=1.0
      IF(NK.EQ.1) GO TO 10
      NL=NS
      NS3=3*NS
      PX=DBLE(PX1/VCAL+RZP)
      PZ=DBLE(PX2/VCAL)
      B=PT(M-2)
      NN=NS
      IF(NB.NE.0) NN=NS-1
   10 AT=1.0
      DO 20 J=1,NN
      JJ=3*J
      X=(XT-PT(JJ-2))/PT(JJ)
      XA=DABS(X)
      Y=PZ/PT(JJ)
      CALL COMER(XA,Y,RE,IM)
      FX=PT(JJ-1)*RE/(1.77245*PT(JJ))
      IF(X.LT.0.) IM=-IM
      BI(J)=1.-FX/B
      BS=BS-FX/B
      DFT(JJ-2)=-2.*AT*PT(JJ-1)*(X*RE-Y*IM)/(1.77245*PT(JJ)**2)
      DFT(JJ-1)=-AT*FX/PT(JJ-1)
   20 DFT(JJ)=-2.*AT*PT(JJ-1)*((X*X-Y*Y-0.5)*RE-2.*X*Y*IM
     1+Y/1.77245)/(1.77245*PT(JJ)**2)
      IF(NB-1) 90,50,80
   50 Z=XT-PX
      G=PT(NS3-1)
      T=PT(NS3-2)
      D=Z*Z+G*G
      FX=T*G/(3.14159*D)
      BI(NS)=1.-FX/B
      BS=BS-FX/B
      DFT(NS3-2)=-AT*FX/T
      DFT(NS3-1)=-AT*FX*(1./G-2.*G/D)
      GO TO 90
   80 X=(XT-PX)/PT(NS3-1)
      XA=DABS(X)
      Y=PZ/PT(NS3-1)
      CALL COMER(XA,Y,RE,IM)
```

```
      FX=PT(NS3-2)*RE/(1.77245*PT(NS3-1))
      IF(X.LT.0.)  IM=-IM
      BI(NS)=1.0-FX/B
      BS=BS-FX/B
      DFT(NS3-2)=-AT*FX/PT(NS3-2)
      DFT(NS3-1)=-2.*AT*PT(NS3-2)*((X*X-Y*Y-.5)*RE
     1-2.*X*Y*IM+Y/1.77245)/(1.77245*PT(NS3-1)**2)
   90 AT=PT(M-2)
      FT=AT*BS+PT(M-1)*XT+PT(M)*XT**2
      BT=FT/AT
      DFT(M-2)=1.0
      DFT(M-1)=XT
      DFT(M)=XT**2
      NK=1
      RETURN
      END



      SUBROUTINE CCMER(X,Y,RE,IM)
C       PROGRAM TO COMPUTE THE COMPLEX ERROR FUNCTION
      IMPLICIT REAL*8(A-H,O-Z)
      REAL*8 IM,LAMBDA
      LOGICAL B
      IF(Y.LT.4.29.AND.X.LT.5.33) GO TO 10
      H=0.
      NCAP=0
      NU=8
      GO TO 20
   10 S=(1.-Y/4.29)*DSQRT(1.-X*(X/28.41))
      H=1.6*S
      H2=2.*H
      NCAP=6+23*S
      NU=9+21*S
   20 LAMBDA=0.
      IF(H.GT.0.) LAMBDA=H2**NCAP
      B=.FALSE.
      IF(H.EQ.0..OR.LAMBDA.EQ.0.) B=.TRUE.
      S1=0.
      S2=0.
      R1=0.
      R2=0.
      N=NU
   30 NPL=N+1
      T1=Y+H+DFLOAT(NPL)*R1
      T2=X-DFLOAT(NPL)*R2
      C=.5/(T1**2+T2**2)
      R1=C*T1
      R2=T2*C
      IF(H.GT.0..AND.N.LE.NCAP) GO TO 40
      GO TO 50
   40 T1=LAMBDA+S1
      S1=R1*T1-R2*S2
      S2=R2*T1+R1*S2
      LAMBDA=LAMBDA/H2
   50 N=N-1
      IF(N.LT.0) GO TO 60
```

```
      GO TO 30
   60 RS=S1
      IF(B) RS=R1
      RE=1.12837916709551*RS
      IF(Y.EQ.0.0) RE=DEXP(-X*X)
      SR=S2
      IF(B) SR=R2
      IM=1.12837916709551*SR
      RETURN
      END



      SUBROUTINE TAREA
C       CALCULATION OF INDIVIDUAL AREAS, RATIOS AND ERRORS
C       FOR NN GAUSSIAN-LORENTZIANS PLUS ONE CONSTR LOR.
      REAL*4 AA(8,8),RSG(8,8),CVR(25,25),VR(25),VA(8)
      REAL*8 P(25)
      DIMENSION IP(8)
      COMMON/AREAS/P,CVR,VR,AREA,ARS
      COMMON/CONTR/M,NS,NP,NB,NL,NK,IUP,ILP,IS
      IPR=6
      ARE=0.
      VRT=0.
      NN=NS
      IF(NB.NE.0) NN=NS-1
      NS3=3*NS
      DO 10 I=1,NN
      II=3*I-1
      ARE=ARE+P(II)
      VRT=VRT+VR(II)
      VA(I)=VR(II)/P(II)
      IZ=I+1
      IF(IZ.GT.NN) GO TO 15
      DO 10 J=IZ,NN
      JJ=3*J-1
      AA(I,J)=P(II)/P(JJ)
      AA(J,I)=1./AA(I,J)
      RV=VR(II)/(P(II)*P(II))+VR(JJ)/(P(JJ)*P(JJ))
     1-2.*CVR(II,JJ)/(P(II)*P(JJ))
      RV=ABS(RV)
      RSG(I,J)=AA(I,J)*SQRT(RV)
      RSG(J,I)=AA(J,I)*SQRT(RV)
      VRT=VRT+2.*CVR(II,JJ)
   10 VA(I)=VA(I)+CVR(II,JJ)/P(II)
   15 CONTINUE
      IF(NB.EQ.0) GO TO 50
      ANS=P(NS3-2)
      VNS=VR(NS3-2)
      VA(NS)=VNS/ANS
      ARE=ARE+ANS
      VRT=VRT+VNS
```

```
      DO 40 I=1,NN
      II=3*I-1
      AA(I,NS)=P(II)/ANS
      AA(NS,I)=1./AA(I,NS)
      RV=VR(II)/(P(II)*P(II))+VNS/(ANS*ANS)
     1-2.*CVR(II,NS3-2)/(P(II)*ANS)
      VA(NS)=VA(NS)+CVR(II,NS3-2)/ANS
      VRT=VRT+2.*CVR(II,NS3-2)
      RV=ABS(RV)
      RSG(I,NS)=AA(I,NS)*SQRT(RV)
   40 RSG(NS,I)=AA(NS,I)*SQRT(RV)
   50 SGAT=SQRT(VRT)/P(M-2)
      DO 60 I=1,NN
      II=3*I-1
      AA(I,I)=P(II)/ARE
      RV=VR(II)/(P(II)*P(II))+VRT/(ARE*ARE)-2.*VA(I)/ARE
      RV=ABS(RV)
   60 RSG(I,I)=AA(I,I)*SQRT(RV)
      IF(NB.EQ.0) GO TO 80
      AA(NS,NS)=ANS/ARE
      RV=VNS/(ANS*ANS)+VRT/(ARE*ARE)-2.*VA(NS)/ARE
      RV=ABS(RV)
      RSG(NS,NS)=AA(NS,NS)*SQRT(RV)
   80 ARE=ARE/P(M-2)
      WRITE(IPR,960)AREA,ARS,ARE,SGAT
  960 FORMAT('0',5X,'EXPER. AREA=',F12.4//6X,'FIT AREA=',
     1F10.4//6X,'BKGRD CORRECTED AREA=',F12.4,2X,'+-',F7.4)
      DO 302 K=1,NL
  302 IP(K)=K
      WRITE(IPR,964)(IP(K),K=1,NL)
  964 FORMAT('0',5X,'AREA FRACTION MATRIX'//7X,'1)RATIO OF AREA OF ONE P
     1EAK TO TOTAL AREA ON DIAGONAL'//7X,'2)RATIO OF AREAS OF ANY PAIR O
     2F PEAKS OFF DIAGONAL'///2X,'PEAK(S)',10I7)
      DO 303 K=1,NL
  303 WRITE(IPR,965)K,(AA(K,L),L=1,NL)
  965 FORMAT('0',1X,I3,8X,8F7.3)
      WRITE(IPR,966)(IP(K),K=1,NL)
  966 FORMAT('0',5X,'AREA FRACTION ERRORS'//2X,'PEAK(S)',
     110I7)
      DO 305 K=1,NL
  305 WRITE(IPR,965)K,(RSG(K,L),L=1,NL)
      RETURN
      END
```

REFERENCES

1. R. L. Mössbauer, Z. Physik, 151, 124 (1958).
2. G. K. Wertheim, A. Hausman, and W. Sanders, The Electronic Structure of Point Defects, North-Holland, Amsterdam (1972), Chapter 1.
3. A. Boltax, Trans. AIME, 218, 812 (1960).
4. J. M. Denney, Acta Met., 4, 586 (1956).
5. A. Boltax, Nucl. Appl., 1, 337 (1965).
6. U. Gonser, R. W. Grant, A. H. Muir, Jr., and H. Wiedersich, Acta Met., 14, 259 (1966).
7. L. H. Bennett and L. J. Swartzendruber, Acta Met., 18, 485 (1970).
8. B. Window, J. Phys. C.: Metal Phys. Suppl. No. 3, 5323 (1970).
9. B. Window, J. Phys. F.: Metal Phys., 1, 533 (1971).
10. B. Window, Phil. Mag., 26, 681 (1972).
11. U. Gonser, Materials Sci. and Eng., 3, 1 (1968).
12. R. C. Reno and L. J. Swartzendruber, Phys. Rev. Lett., 29, 712 (1972).
13. C. E. Violet and R. J. Borg, Phys. Rev., 3, 608 (1967).
14. M. A. Ridout, J. Phys. C., 2, 1258 (1969).
15. B. Window, J. Phys. Chem. Solids, 32, 1059 (1971).
16. B. Window, Phys. Rev. B, 6, 2013 (1972).
17. H. Marcus, L. H. Schwartz, and M. E. Fine, Trans. Am. Soc. Metals, 59, 468 (1966).
18. M. Ron, H. Schechter, A. A. Hirsch, and I. Niedzwiedz, Phys. Lett., 20, 481 (1966).
19. J. M. Genin and P. A. Flinn, Phys. Lett., 22, 392 (1966).

20. B. W. Christ, P. M. Giles and F. C. Ruegg in Mössbauer Effect Methodology (I. J. Gruverman, editor), Vol. 3, Plenum Press, New York (1967).

21. P. M. Gielen and R. Kaplow, Acta Met., 15, 49 (1967).

22. M. Ron, A. Kidron, H. Schechter, and S. Niedzwiedz, J. Appl. Phys., 38, 590 (1967).

23. M. Bernas, S. A. Campbell, and R. Fruchard, J. Phys. Chem. Solids, 28, 17 (1968).

24. M. Ron, H. Shechter and A. Niedzwiedz, J. Appl. Phys., 39, 265 (1968).

25. A. Nagarajan and P. A. Flinn, Appl. Phys. Lett., 11, 120 (1967).

26. H. L. Marcus, M. E. Fine and L. H. Schwartz, J. Appl. Phys., 38, 4750 (1967).

27. S. Nasu, T. Shinjo, Y. Nakamura, and Y. Murakami, J. Phys. Soc. Japan, 23, 664 (1967).

28. E. M. Howard, Application of Mössbauer Effect in Determination of Phase Diagrams, Thesis, University of California at Davis, 1967.

29. A. Heilmann and W. Zinn, Z. Metallk, 58, 113 (1967).

30. R. A. Krogstad, R. W. Moss and V. Vali, Phys. Letters, 4, 44 (1963).

31. R. L. Cohen, J. H. Wernick, K. W. West, R. C. Sherwood, and G. J. Chin, Phys. Rev., 188, 684 (1969).

32. G. K. Wertheim and J. H. Wernick, Acta Met., 15, 297 (1967).

33. R. A. Preston and R. Gerlach, Phys. Rev. B, 3, 1519 (1971).

34. R. A. Preston, D. J. Lam, M. V. Nevitt, D. O. van Ostenburg and C. W. Kimball, Phys. Rev., 149, 440 (1966).

35. J. W. Cahn, Trans. AIME, 209, 1309 (1957).

36. U. Gonser and H. Wiedersich, J. Phys. Soc. Japan, 18, 47 (1963).

37. J. F. Ullrich, Te^{125} Mössbauer Effect Study of Radiation Effects and Magnetic Hyperfine Structure in Tellurium Compounds, Ph.D. Thesis, University of Michigan, 1967.

38. D. Schroeer, R. L. Lambe and C. D. Spencer in Mössbauer Effect Methodology (I. J. Gruverman, editor), Vol. 7, Plenum Press, New York (1971).

39. J. A. Stone and W. L. Pillinger, Phys. Rev. Letters, 13, 200 (1964).

40. C. G. Jacobs, N. Hershkowitz, and J. B. Jeffries, Phys. Letters, 29A, 498 (1969).

41. G. Czjzek, J. L. C. Ford, J. C. Love, F. E. Obenshain, and H. H. F. Wegener, Phys. Rev., 174, 331 (1968).

42. J. F. Ullrich and D. H. Vincent, J. Phys. Chem., 30, 1189 (1969).

43. W. G. Berger, Z. Physik, 225, 1969.

44. P. Hannaford and J. W. G. Wignall, Phys. Stat. Sol., 35, 809 (1969).

45. J. P. Christiansen, U. Hindennach, U. Morfeld, E. Recknagel, D. Riegel and G. Weyer, Nucl. Phys., A99, 345 (1967).

46. P. H. Dedericks, C. H. R. Lehmann, and H. Wegener, Phys. Stat. Sol., 8, 213 (1965).

47. G. Czjzek and W. G. Berger, Phys. Rev., B1, 957 (1970).

48. Y. Gros and J. C. Pebay-Peyroula, Phys. Letters, 13, 5 (1964).

49. Y. Gros, J. Paulene, D. Dautreppe and J. C. Pebay-Peyroula, Compt. Rend., 266, 1199 (1968).

50. G. R. Piercy, J. Phys. Chem. Solids, 23, 463 (1962).

51. R. S. Nelson, J. A. Hudson, and D. J. Mazey, J. Nucl. Matl., 44, 318 (1972).

52. J. G. and V. E. Stevens, Mössbauer Effect Data Index, Plenum, New York (1970).

53. S. Margullies and J. R. Erhman, Nucl. Instr. Methods, 12, 131 (1961).

54. H. Fraunfelder, D. E. Nagle, R. D. Taylor, D. R. F. Cochran and W. M. Visscher, Phys. Rev., 126, 1065 (1962).

55. N. N. Greenwood and T. C. Gibbs, Mössbauer Spectroscopy, Chapman and Hall, London (1971), pp. 10 and 11.

56. J. P. Schiffer, P. N. Parks and J. Heberle, Phys. Rev., 133, A1553 (1964).

57. C. Kittel, Introduction to Solid State Physics, John Wiley and Sons, 4th ed., New York (1971), p. 219.

58. W. A. Steyert and R. D. Taylor, Phys. Rev., 134, A716 (1964).

59. R. S. Preston, S. S. Hanna and J. Heberle, Phys. Rev., 128, 2207 (1962).

60. G. Lang, Nucl. Instr. Methods, 24, 425 (1963).

61. G. A. Bykov and Pham Zuy Hein, Soviet Phys. JETP, 16, 646 (1963).

62. R. M. Housley and R. W. Grant, Phys. Rev., 178, 514 (1969).

63. N. N. Greenwood and T. C. Gibb, op. cit., Chapt. II.

64. G. A. Wertheim, Mössbauer Effect: Principles and Applications, Academic Press, New York (1964).

65. D. A. Shirley, Rev. Mod. Phys., 36, 339 (1962).

66. S. M. Qaim, Proc. Phys. Soc., 90, 1065 (1967).

67. L. R. Walker, G. K. Wertheim, and V. Jaccarino, Phys. Rev. Letters, 6, 98 (1961).

68. S. S. Hanna, J. Heberle, C. Littlejohn, G. J. Perlow, R. S. Preston, and D. H. Vincent, Phys. Rev., 128, 2207 (1962).

69. R. E. Watson and A. J. Freeman, Phys. Rev., 123, 2027 (1961).

70. U. Gonser, C. J. Meechan, A. H. Muir and H. Wiedersich, J. Appl. Phys., 34, 2373 (1963).

71. R. E. Watson, A. C. Gossard and Y. Yafet, Phys. Rev., 140, A375 (1965).

72. R. M. Sternheimer, Phys. Rev., 132, 1637 (1963); Phys. Rev., 130, 1423 (1963).

73. N. F. Mott and H. Jones, Theory of the Properties of Metals and Alloys, Oxford U. Press, Oxford, England (1935).

74. J. Friedel, Nuovo Cimento Suppl., 7, 287 (1958). A. Blandin and J. Friedel, J. Phys. (Paris), 20, 160 (1959).

75. R. A. Preston, D. J. Lam, M. V. Nevitt, D. O. van Ostenburg and C. W. Kimball, Phys. Rev., 149, 440 (1966).

76. B. Window, J. Phys. E., Scientific Instr., 4, 401 (1971).

77. M. Hansen and K. Anderko, Constitution of Binary Alloys, McGraw Hill, New York (1958).

78. J. B. Newkirk, Trans. AIME, 209, 1214 (1957).

79. F. Bitter and A. R. Kaufmann, Phys. Rev., 56, 1034 (1939).

80. F. Bitter, A. R. Kaufmann, C. Starr, and S. T. Pan, Phys. Rev., 60, 134 (1941).

81. D. Hanson and G. W. Ford, J. Inst. Metals, 32, 335 (1924).

82. G. Tammann and W. Oelsen, L. Anorg. Chem., 186, 267 (1930).

83. C. S. Smith, Phys. Rev., 57, 337 (1940).

84. J. Burke, The Kinetics of Phase Transformations, Pergamon Press, New York (1965), Chapter 2.

85. K. E. Easterling and H. M. Meikk-Oja, Acta Met., 15, 1133 (1967).

86. D. S. R. Norris, Rad. Effects, 15, 1 (1972).

87. A. C. Damask in Studies in Radiation Effects on Solids, Vol II (G. J. Dienes, editor), Gordon and Breach, New York (1967), Ch. 1.

88. D. S. Billington and J. H. Crawford, Radiation Damage in Solids, Princeton University Press, Princeton, N.J. (1961).

89. G. J. Dienes and G. H. Vineyard, Radiation Effects in Solids, Interscience, New York (1957).

90. B. T. Kelly, Irradiation Damage to Solids, Pergamon Press, New York (1966).

91. S. M. Torrens and M. T. Robinson in Interatomic Potentials and Simulation of Lattice Defects (P. Gehlen, J. R. Beeler and R. S. Jaffee, editors), Plenum Press, New York (1972).

92. J. R. Beeler, Jr., Phys. Rev., 150, 470 (1966).

93. W. N. McElroy, Nucl. Sci. and Eng., 36, 109 (1969).

94. D. J. Hughes and R. B. Schwartz, BNL-325, Second Edition (1965).

95. F. Seitz and J. S. Koehler, Solid State Phys., 2, 305 (1956).

96. J. A. Brinkman, J. Appl. Phys., 25, 961 (1954).

97. J. A. Davies and G. A. Sims, Canad. J. Chem., 39, 601 (1961).

98. J. A. Brinkman, Am. J. Phys., 24, 246 (1956).

99. J. B. Gibson, A. N. Goland, M. Milgram and G. H. Vineyard, Phys. Rev., 120, 1229 (1960).

100. L. T. Chaderton, Radiation Damage in Crystals, John Wiley and Sons, Inc., New York (1965).

101. D. S. Billington and S. Siegel, Met. Prog., 58, 847 (1950).

102. G. T. Murray and W. E. Taylor, Acta Met., 2, 52 (1954).

103. D. Hull and S. I. Mogford, Phil. Mag., 6, 535 (1961).

104. C. P. Bean and J. D. Livingston, J. Appl. Phys., 30, 1205 (1959).

105. J. W. Cahn, Trans. AIME, 209, 1309 (1957).

106. P. G. Shewmon, Transformation in Metals, McGraw-Hill Co., New York (1969), Chapter 7.

107. G. R. Piercy, J. Nucl. Matl., 5, 158 (1962).

108. J. M. Denney, Phys. Rev., 92, 531 (1953).

109. E. Kankeleit, Rev. Sci. Instr., 35, 194 (1964).

110. T. E. Cranshaw, Nucl. Instr. and Meth., 30, 101 (1964).

111. R. L. Cohen, P. G. McMullin, and G. K. Wertheim, Rev. Sci. Instr., 34, 671 (1963).

112. E. Kankeleit in Mössbauer Effect Methodology (I. J. Gruverman, editor), Vol. 1, Plenum Press, New York (1965), p. 47.

113. R. L. Cohen, Rev. of Sci. Instr., 37, 260 (1966).

114. NBS Misc. Publ. No. 260-13 (1967).

115. J.J. Spijkerman in An Introduction to Mössbauer Spectroscopy (L. May, editor), Plenum Press, New York (1971), Chapter 2.

116. R. Riesenman, J. Steger, and E. Kostiner, Nucl. Instr. Methods, 72, 109 (1969).

117. R. M. Housley, N. E. Erickson and J. G. Dash, Nucl. Instr. Methods, 27, 29 (1964).

118. Y. Z. Yu, "Report on a Method of Measuring the Resistivity of Thin Metallic Foils, Dept. of Nucl. Eng. Internal Report, University of Michigan (1971).

119. H. O. Hartley, Technometrics, 3, 261 (1963).

120. B. J. Chrisman and T. A. Tumollilo, Computer Phys. Comm., 2, 322 (1971).

121. P. B. Merrithew, Ph.D. Thesis, University of Michigan (1967).

122. E. R. Cohen, K. M. Crowe and J. W. M. DuMond, Fundamental Constants of Physics, Ch. 7, Interscience, New York (1957).

123. H. H. Ku, "Notes on the Use of Propagation of Error Formulas," NBS Special Publication, No. 300, p. 331 (1966).

124. D. H. Wilkinson, Nucl. Inst. and Meth., 30, 259 (1971).

125. W. Gautschi, SIAM J. of Numerical Analysis, 7, 187 (1963).

126. J. C. Travis in An Introduction to Mössbauer Spectroscopy (L. May, editor), Plenum Press, New York (1971), Chapter 4.

127. W. Marshall, Phys. Rev., 118, 1519 (1960).

128. W. L. Zyp, "Review of Activation Methods for the Determination of Fast Neutron Spectra," RCN-37, Petten (1965).

129. W. Koehler, "The Determination of the Fast Neutron Fluence by Nickel and Iron Activation Monitors," IAEAIRL18, Vienna (1970).

130. K. Nishina, "Measurement of Fast Neutron Spectra in Ford Nuclear Reactor Core Using Threshold Detectors," Dept. of Nucl. Eng. Internal Report, University of Michigan (1967).

131. R. D. Evans, The Atomic Nucleus, McGraw Hill Book Co., New York (1955)

132. V. A. Lagunov, V. I. Polozenko, and V. A. Stepanov, ZhETF Red 12, 220 (1970).

133. J. O. Linde, Ann. Phys., 15, 219 (1932).

134. K. E. Easterling, Tekn. lic. (thesis), Institute of Technology, Helsinki (1966).

135. A. J. Ardell, Acta Metallurgica, 20, 61 (1972).

136. K. E. Easterling and G. C. Weatherly, Acta Metallurgica, 17, 845 (1969).

137. A. Boltax, Trans. Met. Soc. AIME 224, 286 (1960).

138. J.W. Christian, The Theory of Transformations in Metals and Alloys, Pergamon Press, New York (1965) Ch. 16.

139. A. Goldsmith, T. E. Waterman and H.J. Hirschhorn, Handbook of Thermophysical Properties of Solid Materials, vol. 1, MacMillen, New York (1961).

140. J. G. Mullen, Phys. Rev., 121, 1649 (1959).

141. F. Seitz, Advances in Physics, 1 (1953) p. 43.

142. E.W. Hart, Acta Met. 6, 553 (1958).

143. S.C. Abrahams, L. Guttman, and J.S. Kasper, Phys Rev. 127, 2052 (1962).

144. J. W. Cleland, D. s. Billington, and J. H. Crawford, Jr., Phys Rev. 91, 238 (1953)